

Mitochondrial plasticity implicates their new purpose
in therapy-induced senescence

Inaugural-Dissertation

zur

Erlangung des Doktorgrades

der Mathematisch-Naturwissenschaftlichen Fakultät

der Universität zu Köln

vorgelegt von

Jun Yong Kim

aus Incheon, Republic of Korea

Köln, 2022



Zeugnis / Certificate

über die Doktorprüfung an der
on the doctoral examination at the
Mathematisch-Naturwissenschaftlichen Fakultät
Faculty of Mathematics and Natural Sciences
der Universität zu Köln
of the University of Cologne
gemäß der Promotionsordnung vom 12. März 2020
according to the doctoral regulations of 12 March 2020

Herrn
Mr

Jun Yong Kim

geboren am 10.03.1988 in Incheon (Republik Korea)
born 10.03.1988 in Incheon (Republic of Korea)

hat am 16.08.2022
passed on 16.08.2022

die Disputation mit der Note
the oral thesis defense with the grade

sehr gut (1,0)
very good

und die Dissertation mit der Note
and the dissertation with the grade

sehr gut (1,0)
very good

bestanden.

Promotionsfach: **Biologie**
Research field

Prüfungskommission: Prof. Dr. Thomas Langer (Prüfer/in / Examiner)
Defense Committee Prof. Dr. Andreas Beyer (Prüfer/in / Examiner)
Prof. Dr. Marcus Krüger (Vorsitzende/r / Chairperson)

Titel der Dissertation: **Mitochondrial plasticity implicates their new purpose
in therapy-induced senescence**
PhD thesis title

Gesamtnote: **magna cum laude**
Final grade

Die Promotion ist damit abgeschlossen.
The doctoral examinations are completed.

Dieses Zeugnis berechtigt nicht zur Führung des Doktorgrades.
This certificate does not authorised the candidate to bear the doctoral degree.

Köln, 23.08.2022
Cologne 23.08.2022



Universitätsprofessor
Dr. Ir. Paul H.M. van Loosdrecht
Dekan

Berichterstatter:

Prof. Dr. Thomas Langer

Prof. Dr. Andreas Beyer

Claiming a doctorate of *philosophy*

While science essentially addresses *how*, philosophy does *why*. Thus, the degree shall come with contemplation about *why* after figuring out *how*, which distinguishes one from a technical expert. In this dissertation, I propose meanings inferred from mechanisms to meet the criteria. Now it is in the reader's hands whether it does or not.

Table of contents

1. Abstract
2. Introduction
 - 2.1 Cellular senescence (CS)
 - 2.1.1 Discovery
 - 2.1.2 Cause and type
 - 2.1.3 Regulation
 - 2.1.4 Senescence-associated secretory phenotype (SASP)
 - 2.1.5 Pathophysiological role in mammals
 - 2.2 Mitochondria
 - 2.2.1 Quality control by dynamics
 - 2.2.2 Bioenergetics
 - 2.2.3 One carbon–folate metabolism
 - 2.2.4 Branched-chain amino acid metabolism
 - 2.3 Mitochondria in cellular senescence
 - 2.3.1 Mitochondria as an effector: anterograde response
 - 2.3.2 Mitochondria as a cause: retrograde response
 - 2.3.3 Overview table of the findings in the literature
 - 2.4 Mitochondrial orphan gene OCIAD2
 - 2.4.1 Discovery and regulation
 - 2.4.2 Putative role in patho/physiology
3. Aim of thesis
4. Material and method
 - 4.1 Cell biology
 - 4.2 Biochemistry and molecular biology
 - 4.3 Mouse experiments
 - 4.4 Proteomics and metabolomics
 - 4.5 Data analysis and statistics
5. Result
 - 5.1 Forward genetics: characterizing mitochondria in therapy-induced senescence (TIS)
 - 5.1.1 Establishment of TIS in IMR90 fibroblast
 - 5.1.2 Profound increase of mitochondrial amount in a TIS fibroblast
 - 5.1.3 Increased hypoenergetic mitochondria resolve their paradoxical states in TIS
 - 5.1.4 Time-resolved analysis of mitochondrial proteome during development of TIS
 - 5.1.5 Positive association of mitochondrial translation with 1C-folate metabolism in TIS fibroblasts
 - 5.1.6 Increased nitrogen supply from BCAAs to NEAAs in TIS fibroblasts
 - 5.2 Reverse genetics: OCIAD2 and CS
 - 5.2.1 Identification of OCIAD2 as a pan-marker of CS
 - 5.2.2 OCIAD2 is localized at inner membrane of mitochondria
 - 5.2.3 OCIAD2 is neither sufficient nor required for TIS induction

- 5.2.4 OCIAD2 supports expression of ECM-related SASP genes by TGF- β
- 5.2.5 OCIAD2 neither regulates mitochondrial respiration nor superoxide level
- 5.2.6 OCIAD2 neither regulates glucose metabolism nor fatty acid β -oxidation
- 5.2.7 OCIAD2 supports formation of mitochondrial clump at perinuclear region
- 5.2.8 Analysis of OCIAD2 interactome
- 5.2.9 YME1L1 regulation of OCIAD2
- 5.2.10 Generation of whole-body Ociad2 knockout mice

6. Discussion

- 6.1 Resolving the contradiction of mitochondrial features in CS
- 6.2 Potential role of rewired mitochondria in CS
- 6.3 And still: enigmatic function of OCIAD2

7. Appendix

8. Summary

9. Acknowledgement

10. Eidesstaatliche Erklärung

11. Curriculum vitae

12. Reference

1. Abstract

Cellular senescence and mitochondrial dysfunction are regarded as pillars of aging and age-related diseases such as cancer. As a result, there have been great efforts to understand the role of the two phenomena in such pathological settings. However, the exact relationship between the two is not fully understood due in part to conflicting results. A thorough understanding of their relationship warrants revealing greater therapeutic targets in age-related diseases. Here, I report mitochondrial states with their accurate quantity in a senescent cell. Mitochondria were found to be bioenergetically hypoactive in senescent cells demonstrated by lower membrane potential, lower superoxide level, and lower respiration compared to proliferating cells. However, a profound increase of mitochondrial volume in a senescent cell led to enhanced outputs of the bioenergetic parameters on a cellular base. This largely resolves the paradoxical states of mitochondria in senescent cells and agrees with their age-related dysfunctions. In subsequent analyses combined with time-resolved quantitative proteomics and metabolomics, it was found that metabolic rewiring is the main signature amongst all mitochondrial pathways in senescent cells. In detail, branched-chain amino acid catabolism was increased while one carbon-folate metabolism was rapidly blocked upon the induction of cellular senescence. Such rewired mitochondrial metabolisms orchestrated a synthesis of non-essential amino acids, nucleotides, and translation of mitochondrial RNAs in senescent cells. Besides, a mitochondrial orphan gene OCIAD2 was identified as a pan-senescence marker. The inner mitochondrial membrane protein OCIAD2 regulated the formation of perinuclear mitochondrial clumps in senescent cells. Moreover, bulk RNA-seq analyses discovered its potential crosstalk with TGF- β signaling in senescent cells. However, OCIAD2 neither regulated respiration and superoxide generation, nor oxidation of glucose, glutamine, and fatty acids in mitochondria of senescent cells. Thus, the function of OCIAD2 remains to be determined other than those. These data collectively demonstrate the mitochondrial plasticity in senescent cells and warrant future investigation into their regulatory roles in senescent cells.

2. Introduction

2.1 Cellular senescence (CS)

2.1.1 Discovery

Although it is now accepted as a fact that non-transformed somatic cells are not capable of indefinite proliferation *in vitro*, it was regarded as the very opposite in the early 20th century. Alexis Carrel, a heart surgeon who won the Nobel prize, and his successor Albert Ebeling claimed that they succeeded in culturing minced heart tissues from chick embryos for over 20 years *in vitro*. This was even longer than the lifespan of the chicken. Through inductive reasoning, they concluded that cells taken out of the organism are essentially immortal and there is a certain *in vivo* regulation to limit the lifespan of cells in the body (1, 2). Despite the resistance from the other contemporary scientists, it somehow became a tenet of the era that cells are immortal on the dish. It was not until Leonard Hayflick discovered cellular senescence (CS) assisted by Paul Moorhead that the cellular immortality *in vitro* was deemed an artifact. In 1961, Leonard Hayflick reported that 25 different somatic fibroblast strains derived from different organs of human fetuses were explanted and cultured on the dish. Contrary to the expectation, all fibroblast strains stopped doubling after a certain period in culture while remaining viable and metabolically active by producing acid (lactate) (3). This was regardless of the culture conditions as cells with late passages stopped proliferating earlier than those with early passages under the same culture conditions—and this was also true to the frozen-thawed fibroblasts, which pointed to the existence of an intracellular clock that a cell somehow remembers (4). In those studies, he applied the word senescence which was exclusively used then to indicate organismal aging to describe the phenomenon of the permanent growth arrest state of the cells. It was based on his conjecture that it might reflect the aging process in the organism and thereby it would be a cellular counterpart to the organismal aging. Another conjecture of his was that the CS is an anti-tumor mechanism to prevent immortalization and hence neoplastic transformation, which took several decades thereafter to be proved to be true.

2.1.2 Cause and type

The original CS discovered by Hayflick was named replicative senescence (RS). In the 1990s, multiple lines of evidence showed that telomere attrition is the cause of the RS (5-7), indicating the telomere length is the intracellular clock for a cell division conjectured by Hayflick. In parallel, it was found that oncogenic signaling could induce the CS (8), regardless of telomere length (9) in agreement with the hypothesis that the CS is a barrier to tumorigenesis (10). This type of senescence has been

named oncogene-induced senescence (OIS). Apart from the RS and the OIS which occur exclusively in non-transformed cells, a variety of cellular stresses when given at sublethal doses have been found to be able to evoke the CS in malignant cells as well as diploid cells, termed stress-induced senescence (SIS) (11). The SIS-evoking stimuli encompass genetic, epigenetic, oxidative, and metabolic stresses. Of note, the current regimen of anti-cancer therapy by ionizing radiation (IR) and chemotherapeutic agents is largely overlapped with the SIS-evoking stimuli due to the vulnerability of cancer cells to such stresses. Later, it was more specifically coined as therapy-induced senescence (TIS) in the context of anti-cancer therapy (12). The TIS essentially takes place not only in the therapeutic target cells, that is cancer cells, but also in the non-targeted stromal cells because virtually all cells in the body will be exposed to the chemotherapeutic agents administered by intravenous injection. Similar to the generality of the TIS, the CS could occur in a diverse type of cells such as adipocytes, hepatocytes, melanocytes, keratinocytes, and endothelial cells as well as fibroblasts. However, the CS is categorized by its triggering stimulus, not by the type of cell in which the CS occurs. Besides, it was suggested recently that post-mitotic cells such as neurons can be senescent (13), although one needs to be careful to distinguish the senescence from senescent-like phenotypes.

2.1.3 Regulation

The CS is defined as a permanent arrest of the cell cycle. The irreversibility of the growth arrest stemmed from the fact that no physiological stimuli discovered yet can make senescent cells re-enter the active cell cycle (14), although genetic manipulations can reverse it (15-17). As inferred from the definition, the essential regulation of CS largely lies in two major cyclin-dependent kinase regulators, the p21 and p16^{INK4A} which ultimately converge upon dephosphorylation of the Rb protein to disable the G1-S progression (18). On one hand, upon the CS-promoting genotoxic stimuli, DNA damage sensor ATM or ATR kinases halt the cell cycle by stabilizing tumor suppressor p53 and subsequently activate the transcription of CDKN1A which encodes p21 protein. On the other hand, some other CS-triggering stimuli such as epigenetic stress seem to act on the derepression of p16^{INK4A} linked with the senescence-associated heterochromatin foci (SAHF) caused by a chromatin reorganization (19, 20). Once the cell cycle is arrested at G1 either through p21 or p16^{INK4A}, or even both, several other signaling pathways are engaged to stabilize the arrested state. For example, cellular reactive oxygen species (ROS) mainly generated from mitochondria potentiates the arrested state (21, 22). Another example is a reduction of the nuclear lamina gene LMNB1 by transcriptional repression in concert with autophagic degradation, which triggers alteration of chromatin structures and thereby large-scale gene expression changes (23-25). Such a dramatic remodeling of genome and epigenome is thought to potentiate the senescent states, called 'deep' senescence (18).

It is noteworthy that cancer cells can still become senescent under genotoxic stimuli. Cancer is generated from somatic mutations of tumor suppressors such as p53 which is the very gene that drives the CS. That is, although multiple types of cancer have a loss-of-function mutation of p53, they are still responding to genotoxic stimuli to activate the DDR and reach the senescent state. A *in vivo* study demonstrated that post-translational modifications (PTMs) of p53 by acetylation dictate the tumorigenic outcomes by regulating the cell fate between the cell-cycle arrest, apoptosis, and senescence (26). These data implicate that there is a mechanistic distinction in p53 by the PTMs to modulate the senescence response. It also indicates the tumorigenic loss-of-function of p53 is not related to its ability to relay the DDR signaling to induce the CS.

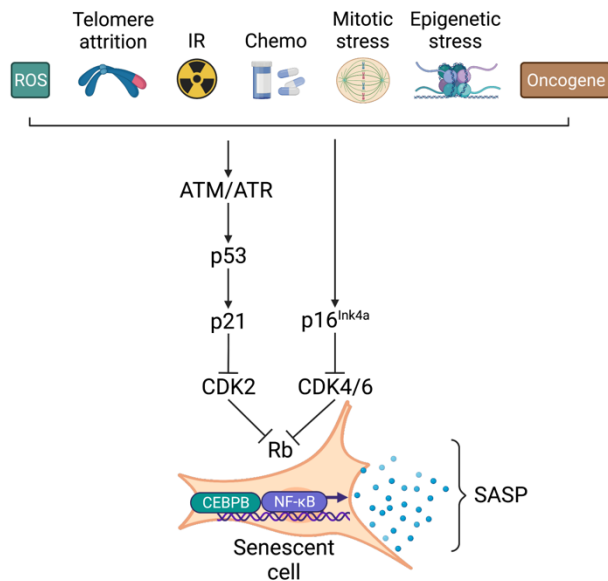
2.1.4 Senescence-associated Secretory Phenotype (SASP)

Senescent cells secrete a panoply of bioactive molecules termed as senescence-associated secretory phenotype (SASP) (27). Arguably, the SASP is the most critical factor to understand the biology of the CS for two reasons. First, it can explain its pleiotropic effects on the cell, tissue, and organismal level. Second, it is the unique character of senescent cells distinct from quiescent or terminally differentiated post-mitotic cells. The main comprising factors of the SASP have been identified as immunomodulatory cytokines and chemokines, extracellular matrix (ECM) modifiers, and growth factors (27, 28). By virtue of the SASP, senescent cells communicate with their neighboring cells in a paracrine manner as well as potentiate their own senescent phenotypes through autocrine mechanisms (29). As such, they exert the pleiotropic effects. One of the most crucial effects is that the cytokines and chemokines of the SASP promote inflammation in the microenvironment of senescent cells. These include interleukins (IL1, IL6, CXCL8), MCPs (monocyte chemoattractant proteins), MIPs (macrophage inflammatory proteins), and GM-CSF (granulocyte/macrophage colony-stimulating factor) (14). Other effects of the senescent cells on their microenvironment include stimulation of the neighboring cell proliferation via GROs (growth-regulated oncogenes) (30) and amphiregulin (31), angiogenesis by VEGF (32), and importantly bystander senescence via TGF- β signaling (33). The SASP can also induce epithelial-to-mesenchymal transition (EMT) in its recipient cells (34). Such pleiotropic effects of senescent cells are even more complex by the heterogeneity of the SASP dictated by the type of a cell, a trigger, and the duration of being senescent (28).

Nevertheless, several core pathways regulate the SASP largely regardless of the cell type or trigger. One is the DNA-damage response (DDR) pathway mediated by ATM and CHK2, upstream regulators of p53 (35). However, the role of p53 in the SASP is not linear. p53 is essential for the development of the SASP but once it is established, p53 puts a brake on it to prevent its uncontrolled

expression (27, 35). Thus, it appears that p53 regulates the robustness and strength of the SASP through an inhibitory feedback mechanism. In addition, an engagement of the DDR pathway turned out to be necessary for the SASP since there is no or little development of the SASP if the CS is established by ectopic overexpression of p21 or p16^{INK4A} (36). Another positive regulator is nuclear factor κ B (NF- κ B). Once the NF- κ B signaling is activated by IL1A, it stimulates the transcription of several pro-inflammatory SASP factors including IL6 and CXCL8 (37, 38). Another transcription factor CEBPB (CCAAT/enhancer-binding protein β) also similarly regulates the SASP to NF- κ B (37, 39, 40). However, the regulation of the SASP does not only lie in the transcriptional layer. For instance, p38 MAPK signaling could enhance the transcriptional activity of NF- κ B and thereby increases the SASP expression (41). In addition, it has been shown that mTOR signaling can regulate the SASP, at least in part, by promoting a translation of IL1A and MK2 mRNAs which are the positive regulators of the SASP (42, 43).

Another important aspect of the SASP is that it develops only after the incipient cell cycle arrest is established. The temporal dynamics is important to distinguish the SASP from any other stress responses that elicit SASP-like cytokines (44). It also hints that the SASP can be temporally segregated from the growth arrest of senescent cells. Indeed, many studies demonstrated that the SASP can be uncoupled from the growth arrest state of senescent cells. For example, p53 inactivation in senescent cells resumes the cell cycle but the SASP remains active (15, 27, 35). Another example is the oxygen tension playing between the growth arrest and the SASP. The physiologic oxygen tension present in mammalian tissues varies between 2–10% but it never reaches the atmospheric level (20%) (45). Several studies demonstrated that oxygen tension selectively affects the SASP upon the establishment of the CS by multiple means (46, 47). Particularly, the AMPK-mediated mTOR suppression was found to be one of the mechanistic links between oxygen tension and the SASP (47). Finally, the TGF- β signaling together with NOTCH signaling was shown to regulate the temporal dynamics of the SASP during its development (48, 49).



2.1.4 Regulation of cellular senescence and SASP

Diverse senescence-evoking stimuli converge on the p53 or p16^{Ink4a} pathway and ultimately arrest the cell-cycle. NF-κB and CEBPB are transcription factors responsible for the SASP expression.

2.1.5 Pathophysiological role of senescent cells

While the CS is a cell-autonomous mechanism, the SASP is a non-cell-autonomous mechanism that exerts a myriad of effects on organismal pathophysiology. That is, the temporality and heterogeneity of the SASP yield the versatile outcomes of the CS. This is the key notion to comprehending the seemingly paradoxical roles of senescent cells in organismal health. For example, the CS is a barrier to tumorigenesis but the chronic SASP has pro-tumorigenic effects (50). Moreover, the SASP has been implicated in seemingly incongruent biological processes, ranging from aging and cancer to wound healing, tissue repair, and embryonic development. This is in which the SASP kinetics plays a key role to produce such versatile outcomes of senescent cells. Below are the concrete examples that senescent cells contribute to the pathophysiology of the organism through the SASP.

One of the biological processes related to acute CS is wound healing and tissue repair. Upon the skin wound, fibroblasts are activated to myofibroblasts and secrete fibers to close the wound. It was found that the activated myofibroblasts subsequently undergo senescence to restrict excessive fibrosis at the site of injury (51). In addition, the senescent cells at the site of cutaneous wound secrete platelet-derived growth factor AA (PDGF-AA) to accelerate the wound closure (52). A similar case was observed in liver injury (53). When there is a fibrotic insult in the liver, hepatic stellate cells (HSCs) become activated to repair the damage and then subsequently senescent, followed by elimination by natural killer (NK) cells to complete the tissue repair. However, when the HSCs are genetically made

not to senesce upon the induction of liver fibrosis, the liver becomes excessively fibrotic. These findings demonstrate the beneficial role of senescence in maintaining tissue homeostasis and provide the evolutionary justification of the CS.

Another example of acute senescence is that it appears and disappears during the development of mammalian embryos to regulate angiogenesis in the uterine and remodel the tissues such as mesonephros, endolymphatic sac, neural roof plate, and apical ectodermal ridge (54-56). These results expand the biological meaning of the CS from the stress response to the programmed morphological process.

Contrary to the spatiotemporally regulated CS, aging-related CS augmented throughout life is thought to be a stochastic and uncontrolled process (18). The reason for the accumulation of senescent cells along the organismal aging is not clear yet. Two possible scenarios were conceived: an increased generation and a decreased elimination of senescent cells, or both. On one hand, the generation of senescent cells seems to be correlated with the cumulative exposure to the CS-evoking stresses throughout the life of the organism (57). On the other hand, the removal of senescent cells appears to be decreased in late periods of life presumably due to the malfunction of the immune system (18), based on the findings of immune clearance of senescent cells in cancer and fibrosis (53, 58, 59). In any case, the aging-related CS entails the switch from transient to persistent SASP which causes age-related tissue dysfunctions. In particular, the lingering pro-inflammatory SASP factors would create tissue with chronic inflammation, characterized by infiltration of immune cells. Chronic inflammation is one of the common causes of age-related diseases and thus the persistent SASP is very likely to be attributed to age-related diseases including cancer (18, 60). In support of this idea, it was shown that when senescent cells were cleared from a progeroid mouse model as well as naturally aged mice, the median lifespan and healthspan were significantly increased together with reduced inflammatory phenotypes such as arthritis and cataracts (61, 62). Having started from these phenomenal landmark studies, an ample amount of evidence indicated that clearance of senescent cells ameliorates numerous age-related disease phenotypes including pulmonary fibrosis, osteoarthritis, hepatic steatosis, cardiovascular disease, frailty, and neurodegeneration (63).

Particularly in cancer, mounting evidence suggests that senescent cells promote malignancies. For example, co-injection of senescent fibroblasts with epithelial tumor cells significantly increased the tumor size through the SASP (64, 65). Senescent cells also induce EMT of their neighboring tumor cells by the SASP (34, 66). Other examples are derived from studies of the TIS. When cancers are treated with chemotherapeutic agents (e.g., doxorubicin) in mouse models of lymphoma and prostate cancer, the SASP secreted in the tumor microenvironment confers the therapy resistance to the very agent (67, 68), but interestingly not to another one (69).

The fact that the acute CS is beneficial while the chronic one is detrimental to the organismal health puts its role as a good example of antagonistic pleiotropy explained by an evolutionary theory of aging (14). That is, the organism is evolved to ensure the survival of early periods of life—more precisely, reproductive periods—at the expense of the debility of its late periods (70). Thus, the outstanding question lies in dissecting the beneficial and detrimental aspects of the CS via a thorough understanding of the regulatory mechanism and thereby finding a way to selectively modulate its bad outcomes, which has garnered a lot of attention and been developed as a concept of senotherapy (71).

2.2 Mitochondria

2.2.1 Mitochondrial dynamics and quality control

The textbook description of mitochondria used to be tubular and static. With the advent of time-lapse imaging techniques, however, it turned out that mitochondria are highly dynamic with a continuous fusion and fission. Such a dynamic morphology of mitochondria is often regarded in the thought frame “form follows function” quoted from the penetrating principle of industrial design and architecture in the 20th century (72). In this vein, extensive efforts were made to ascribe their morphology to the corresponding cellular outcomes. For example, mitochondria are fragmented as a result of excessive nutrients, cell death, and impaired oxidative phosphorylation (OXPHOS), whereas hyperfusion of mitochondria is due, in part, to nutrient starvation and increased OXPHOS (73). Not only metabolism but also the regulation of apoptosis, Ca²⁺, and reactive oxygen species (ROS) levels are directly related to mitochondrial morphology. Although fixed images of tubulated and fragmented mitochondria are linked to distinct cellular phenotypes, the balance and dynamics—timely fusion and fission—are critical parameters of cellular fitness (74). One of the compelling hypotheses is that the dynamics ensures quality control by mixing and dividing the information in each mitochondrion and thereby complementing and diluting any present anomaly (75). In addition, the fragmented mitochondria are prone to be degraded by autophagy (76), which also promotes quality control (77). In light of this, the molecular regulators of morphological dynamics of mitochondria have been studied in detail. Below are several examples of the key regulators.

Mitofusins are dynamin-like GTPases that mediate the fusion of the outer membrane of mitochondria (OMM). There are two mitofusins in mammals, MFN1 and MFN2. These form homo- and heterodimers at the OMM and enable the fusion by GTP hydrolysis activity. The deletion of either one of them blocks the mitochondrial fusion in cultured cells to yield fragmented mitochondria. Of note, the same deletion leads to embryonic lethality in a mouse, demonstrating the essentiality of mitochondrial fusion in embryonic development (78). In some adult tissues, the function of each mitofusin seems to be redundant but in other tissues such as neurons and the heart, each of them has a distinct role which suggests a tissue specificity (73, 79, 80). The critical mechanism of mitofusins regulation is PTM. In particular, ubiquitylation by E3 ubiquitin ligase MARCHF5 plays a crucial role in proteasome-mediated degradation of mitofusins (81).

Optic atrophy 1 (OPA1) is another dynamin-like GTPase that orchestrates the fusion of the inner membrane of mitochondria (IMM). OPA1 has multiple forms resulting from alternative splicing and proteolytic cleavage. The alternative splicing yields long forms (L-OPA1) and proteolysis of those long forms by proteases OMA1 and YME1L1 gives rise to short forms (S-OPA1) (82). When L-OPA1

anchored at the IMM is cleaved by OMA1 and/or YME1L1, the soluble product S-OPA1 is released to the intermembrane space (IMS) of mitochondria (83). An excessive accumulation of S-OPA1 in the IMS results in mitochondrial fragmentation while L-OPA1 is sufficient for mitochondrial fusion. Therefore, the proteolysis of L-OPA1 by the two proteases is a critical regulator of fusion and fission balance. It is also imperative that OPA1 deletion in mice is embryonic lethal while haploinsufficiency phenocopies the optic neuropathy in humans such as slow-onset retinal degeneration, and a gradual loss of vision (73). This evidence links the mitochondrial fusion/fission balance to the pathology of tissues.

Dynamamin-related protein 1 (DRP1) is responsible for the fission of the OMM. Unlike MFNs or OPA1, DRP1 resides in cytosol. When there is a cue for mitochondrial fission, DRP1 is translocated to a fission site in the OMM regulated by DRP1 receptors and recruitment factors such as FIS1, MFF, MiD49, and MiD51 (84). There it oligomerizes into ring-like structures coordinated by the actin cytoskeleton and endoplasmic reticulum (ER) (85), followed by GTP hydrolysis which results in the DRP1 conformation change, and membrane constriction and scission (86). As a result, DRP1 loss-of-function yields hypertubulated mitochondria in multiple organisms like yeast, worms, and mammals (73). Like other fusion regulators, the regulation of the DRP1 mainly lies on the PTM including phosphorylation, ubiquitylation, and SUMOylation (87). Moreover, the whole-body deletion of the DRP1 causes embryonic lethality in mice (88), demonstrating the essentiality of mitochondrial dynamics in the viability of the organism.

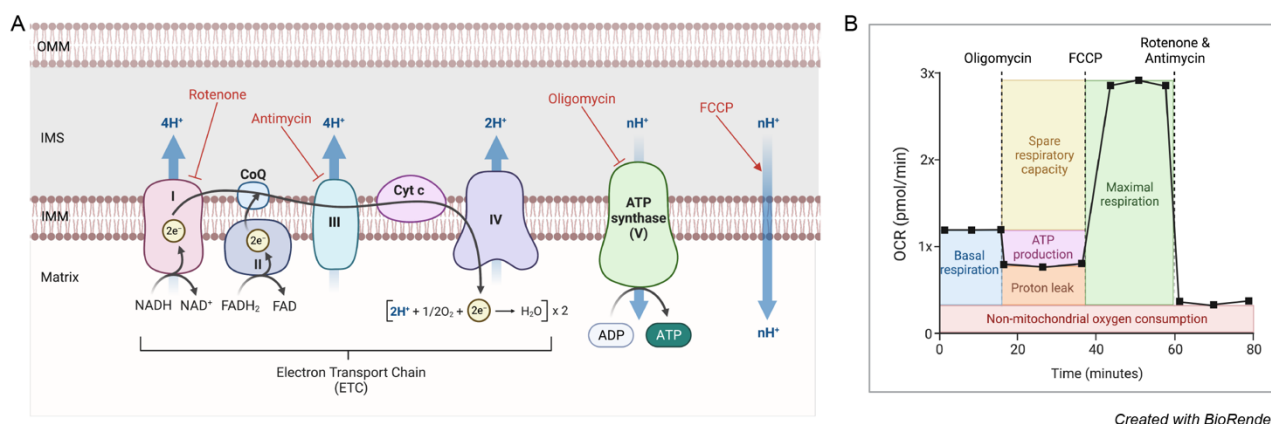
2.2.2 Bioenergetics: from discovery to assessment

Mitochondria are a powerhouse of a cell—probably the most consumed cliché when describing the role of mitochondria. Cells breathe through mitochondria and generate an energy currency of a cell, ATP. Contrary to such a cliché, it has long stood out as a matter of debate on how mitochondria synthesize ATP (89). The main problem was that the number of ATP molecules generated per glucose or oxygen molecule is not stoichiometric; it is a variable number and never an integer (90). This was a profound issue not only because there is no such thing as 2.5 ATP but also if it is not stoichiometric, it is not chemistry. However, biology does not violate any law of physics or chemistry. This led researchers for a long time to search for a high-energy chemical intermediate that acts as an energy transferer from glucose oxidation down to ATP synthesis (89). Instead, in the same year of the discovery of the CS, Peter Mitchell ingeniously proposed the concept of chemiosmosis to resolve the apparent violation (91). The chemiosmosis theory explains the non-stoichiometric nature by a gradient of protons across the membrane. Electron transport chain (ETC) complexes embedded in the IMM transport electrons provided by NADH and FADH₂ which are generated by oxidizing nutrients. The

electrons flow through the ETC to oxygen molecules to generate water molecules. The serial transport of high-energy electrons along the ETC complexes is coupled with their proton pumping activity across the IMM to generate the proton gradient, which is the foundation of mitochondrial membrane potential (MMP). The accumulated protons at the IMS then flow back into the matrix through ATP synthase and rotate the stalk of the enzyme. The rotation results in its conformational change and catalyzes the ATP synthesis (92). The essence of the way it works is that it makes a gradient by continuous pumping. The gradient is not stoichiometric. It is an analog as a varying amplitude. Thus, mitochondria are the converter of the digital number of nutrient molecules to the decimal number of ATP molecules through the analogous mechanism. This is a fundamental process virtually taking place in any living organism equipped with mitochondria.

The ETC in mammalian cells is comprised of 4 different complexes (CI, CII, CIII, CIV). Together with the ATP synthase as a final step processor of the electron transport (which is CV), they are called the OXPHOS complex. Each OXPHOS complex has subunits, except CII, that are encoded from nuclear DNA and mitochondrial DNA (mtDNA). This dual origin necessitates the coordinated expression of the subunits from the two genomes and the regulation of their proper assembly to ensure functional ATP synthesis (93). When assessing the functionality of the OXPHOS, the ATP level seems to be a direct readout. However, ATP is not only used as an energy currency but also as a building block of DNA, introducing confounding results from multi-step regulations after its synthesis. Rather, oxygen consumption rate (OCR) would be closer to the genuine parameter of the OXPHOS function. With the advent of technology to monitor the OCR in a real-time manner, the mitochondrial bioenergetics in cells can be profiled by sequentially adding pharmacological modulators of the OXPHOS (94, 95). The modulators generally include rotenone (CI inhibitor), antimycin A (CIII inhibitor), oligomycin (CV inhibitor), and FCCP (protonophore). The obtained profile upon the addition of the OXPHOS modulators commonly includes basal respiration, maximal respiration, and spare respiratory capacity, ATP-linked respiration and proton leak, OXPHOS coupling efficiency, and non-mitochondrial OCR. These are important parameters to assess the (dys)functionality of the mitochondria. For example, the protonophore FCCP dissipates the proton gradient by carrying the protons into the matrix. This results in a maximal flow of electrons through the ETC complexes since the chemiosmotic inhibition is removed. The maximal respiration indicates substrate availability, given that the ETC is intact. Thus, the spare respiratory capacity would be a parameter of the metabolic flexibility of a cell. Also, the ATP-linked respiration measured by oligomycin is a direct readout of the OXPHOS function. The remaining OCR then comes from the proton leakage into the matrix without involving the CV to synthesize the ATP. From these two parameters, the OXPHOS coupling efficiency can be calculated. It reflects the integrity of the ETC complexes. Finally, the non-mitochondrial OCR

is thought to be a result of the ROS outside of the mitochondria or the activity of oxygenase and oxidase in the cytosol (94, 95).



2.2.2 Mitochondrial bioenergetics

(A) Schematic depiction of OXPHOS complex and corresponding modulators.
 (B) Profiling mitochondrial bioenergetics by monitoring oxygen level in a real-time.

2.2.3 Branched-chain amino acid (BCAA) metabolism

Throughout a life of a cell, it faces diverse situations with cues to grow and divide. In order to proliferate, it needs to metabolize available nutrients to generate required macromolecules such as nucleotides and lipids for a newly divided cell (96). In particular, the metabolism of a eukaryotic cell is generally characterized by compartmentalization between fermenting cytosol and respiring mitochondria (97) which provides a cell not only ATP but also key substrates for cellular anabolism through oxidation of given nutrients. Arguably, this enabled a eukaryotic cell to dramatically expand its metabolic repertoire to support sophisticated and diverse cellular processes. This notion is supported by a pleiotropic role of mitochondrial metabolism in a proliferating cell as extensively documented in the literature for the past few decades in addition to their classical view as a cellular powerhouse to generate ATP (98).

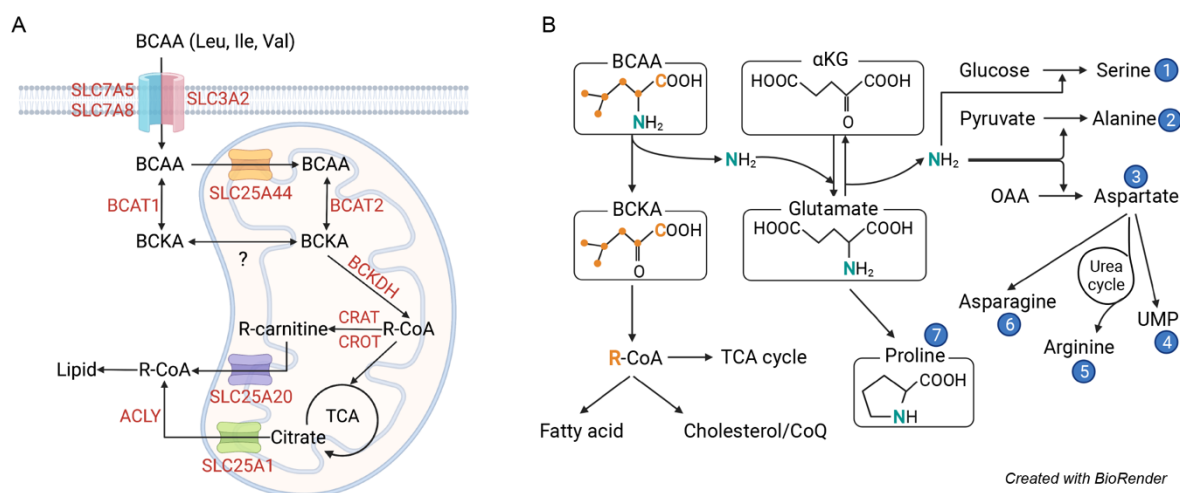
Amongst other nutrients like glutamine and fatty acids, branched-chain amino acids (BCAAs) are metabolized nearly exclusively in the mitochondria. BCAAs (leucine, isoleucine, and valine) are essential amino acids (EAAs) in metazoans and hence they have to be supplied by dietary intake. BCAAs are imported into a cell via heterodimers of solute carriers SLC7A5/SLC3A2. They are copious components of animal proteins which comprise about 18% of total amino acids in most mammalian proteins (99). BCAAs are critical for protein functions as their branched R group (hence their name) is small and hydrophobic to ensure the proper structures of proteins (100, 101). Besides the role of protein constituents, BCAA—particularly leucine—can act as a signaling molecule. Leucine is an agonist of mTORC1 (mammalian target of rapamycin complex 1) (102) and hence

promotes cap-dependent mRNA translation (103). Leucine also activates insulin secretion in pancreatic islet cells (104). These findings put leucine as an evolutionary indicator of access to protein-derived amino acids in mammals as it is the most abundant EAA and connects the two major anabolic processes (99). On contrary with leucine, not much is known about valine and isoleucine for their roles as signaling molecules.

The catabolism (oxidation) of each BCAA in a mammalian cell shares a similarity with each other. In the first reaction, all three BCAAs are transaminated by branched chain aminotransferases (BCATs) to yield branched chain α -ketoacids (BCKAs). There are two genes encoding BCATs; BCAT1 is localized in the cytosol and BCAT2 in the mitochondrial matrix. BCAT1 is expressed specifically in the human pancreas and brain whereas BCAT2 is rather ubiquitous except in the mouse liver (105-107). It was recently found that SLC25A44 imports a fraction of cytosolic BCAAs into mitochondria (108). By BCATs, the amino group of BCAAs is transferred to α -ketoglutarate (α KG) to make glutamate and BCKAs. The second step—and the rate-limiting step—is the oxidation of all BCKAs by a branched chain ketoacid dehydrogenase (BCKDH) complex. While BCATs act in bi-direction, the BCKDH complex does in uni-direction toward oxidation. This irreversibility makes BCAAs essential in animals. BCKDH complex is comprised of three subunits, a decarboxylase tetramer encoded by BCKDHA and BCKDHB, a transacylase encoded by DBT, and a dehydrogenase encoded by DLD. As a result, the oxidation of BCKAs yields CO_2 by the decarboxylation, NADH by the dehydrogenation, and corresponding branched-chain acyl-CoAs by the transacylation. Of these, the critical regulation lies in BCKDHA phosphorylation coordinated by BCKDH kinase (BCKDK) and phosphatase PPM1K (109, 110). The generated branched-chain acyl-CoAs are then either fully oxidized to acetyl-CoA/propionyl-CoA/succinyl-CoA to enter the TCA cycle or transformed to acyl-carnitines. These metabolites, one or the others, can be used for lipogenesis in the cytosol and TCA cycle anaplerosis. For lipogenesis, the acyl-CoA molecules need to be exported via SLC25A20 from mitochondria in a form of acyl-carnitines (111) or via SLC25A1 as citrate (112) because CoA is a bulky and prosthetic moiety that makes its adducts unable to cross the mitochondrial membrane (99).

The fate of BCAA carbons between the complete oxidation and the lipogenesis is largely tissue-specific and context-dependent. For example, muscle is the major tissue of their full oxidation to generate ATP (113) whereas adipose tissue breaks down the BCAAs as a metabolic sink to generate lipids and thereby maintain the blood BCAA level (108, 114). Besides the carbons, the nitrogen of BCAAs transferred to glutamate at the first catalytic step has multiple fates as well. The nitrogen then can be transferred from the glutamate to alanine, serine, proline, or aspartate. Especially the one transferred to the aspartate can ultimately be transferred to arginine through the urea cycle, uridine through dihydroorotate dehydrogenase (DHODH), or asparagine through asparagine synthase (ASNS).

Hence the nitrogen of BCAAs supports the synthesis of non-essential amino acids (NEAAs) and pyrimidines. Therefore, the catabolism of BCAA in the mitochondria collectively supplies the TCA cycle intermediates, the lipogenic acyl-CoAs, and the amino group for the synthesis of NEAAs and nucleotides in a tissue-specific manner, which affects the whole-body metabolism as well as the cellular metabolism (99).



2.2.3 Catabolism of branched-chain amino acids (BCAAs)

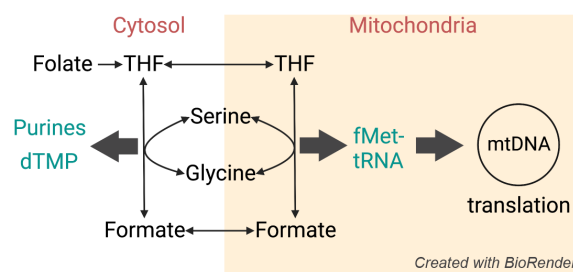
(A) Schematic depiction of BCAA metabolism between cytosol and mitochondria. Several key enzymes are denoted.
 (B) Fates of BCAA carbons and nitrogen into downstream metabolites. The nitrogen fates are denoted with numbers.

2.2.4 One carbon-folate metabolism

One carbon (1C)-folate metabolism is another example of the critical pathway to support the biosynthesis of nucleotides and redox equivalents. Like the BCAAs, the folate is essential to be supplied by dietary intake in animals but not in bacteria or plants. The metabolic pathway is compartmentalized between the mitochondria and the cytosol with isozymes in each locale. Each isozyme works in parallel and a bidirectional manner, depending on the supply-to-demand ratio, and the cofactor redox balance (115). As a first step to utilizing the folate for a mammalian cell, it needs to be activated as a reduced form of tetrahydrofolate (THF) by dihydrofolate reductase (DHFR) in the cytosol. 1C unit then is supplied from serine to the THF catalyzed by serine hydroxymethyltransferases (SHMTs), which subsequently yields glycine and 5,10-methylene-THF. The 5,10-methylene-THF is critical to generating deoxythymidine nucleotides (dTxPs) from deoxyuridine monophosphate (dUMP) catalyzed by thymidylate synthase (TYMS) in cytosol. The subsequent reaction converts the 5,10-methylene-THF to 10-formyl-THF which serves to synthesize purines in the cytosol, formylated methionine in the mitochondria, and NADPH in both.

All these products of the 1C-folate metabolism are highlighted in fundamental aspects of cell biology. For example, needless to say, the purines and the dTxPs are building blocks of DNA and RNA. Therefore, the metabolic demand for the 1C-folate pathway is particularly high in proliferating cells (116). In light of this, the folate activator DHFR was the first target among the anti-cancer chemotherapeutic targets (117). It is also important that the dTxPs in the mitochondria are critical for mtDNA homeostasis (118, 119). However, it is under debate whether dTxPs are synthesized in mitochondria by TYMS (115, 119). Another product of the 1C-folate pathway is mitochondrial formylmethionine (fMet). Like bacteria, the initiation of translation in the mitochondria requires the fMet and this enables the synthesis of the mtDNA-encoded OXPHOS subunits (120, 121). This is critical for cell survival such as in low glucose conditions by enabling a shift to an enhanced OXPHOS activity (122). In addition to the nucleotides and the fMet, the compartmentalized generation of NADPH in the cytosol and the mitochondria regulates oxidoreductive biochemical reactions in each compartment. For example, NADPH is necessary for cytosolic fatty acid synthesis, mitochondrial proline synthesis, and to reduce oxidized glutathione—GSSG to GSH—in both (123-125). The GSH/GSSG ratio is important to defend against oxidative damages such as lipid peroxidation (126). Lastly, the glycine produced from the catalysis of the serine can be used for the synthesis of heme, glutathione, purines, and creatine (127). Thus, the products of the 1C-folate metabolism would have different essentiality according to the cellular contexts such as fast proliferation or oxidative damage defense.

Of note, although the 1C-folate metabolism yields redundant metabolites between the cytosol and the mitochondria, a germline deletion of *Shmt2*, *Mthfd1*, or *Mthfd11* but not *Shmt1* in mice causes embryonic lethality (128-131). This argues that cytosolic serine catabolism is dispensable for the development of the mouse embryo. It was suggested that the majority of serine is catabolized in the mitochondria rather than cytosol to uncouple 1C metabolism from glycolysis because the two pathways compete for NAD (127). This indicates the presence of a cellular strategy for allocating redox cofactor budget in diverse processes.



2.2.4 Schematic diagram of one carbon-folate metabolism

*dTxPs: deoxythymidine nucleotides, *fMet: formylmethionine, *THF: tetrahydrofolate.

2.3 Mitochondria and CS

The mitochondrial dysfunction and the CS are regarded as hallmarks of aging (132). Hence it is tempting to conjecture that there is a crosstalk between these two hallmarks. However, there is surprisingly not much evidence of how much of the mitochondrial dysfunction observed in aged tissues are derived from the senescent cells or *vice versa*. That is, it is not clear yet whether aging-related mitochondrial dysfunction is a cause or consequence of the CS found in the aged tissues. Thus, the scope of the introduction below is restricted to direct evidence of a relationship between mitochondrial features and senescent cells *per se*, regardless of the aging context.

Often, the mitochondrial role in the CS is categorized by the functional aspects of mitochondria. However, this somehow confuses the readers whether it is the cause or consequence of the CS. To circumvent this, it is written in two parts each with supporting evidence. On one hand, the downstream effector roles of mitochondria in the CS evoked by non-mitochondrial (nuclear) stimuli, which is an anterograde response from the nucleus to mitochondria. On the other hand, the upstream initiator roles of mitochondria in the CS induced by direct mitochondrial perturbations, a retrograde response from mitochondria to the nucleus (133). It is also important to distinguish whether the CS is a major outcome under the given stimuli, especially *in vitro* cell culture. Since the CS essentially shares the regulatory pathway with apoptosis, the CS-evoking stimuli can yield compounding results (134). Thus, the introduction is written with an emphasis on the effect size of the CS to be the major outcome of a given stimulus.

Lastly, the field is confounded with conflicting results regarding the mitochondrial status in senescent cells. It seems to be largely due to the complexity of the CS—the type of cells and stimuli, duration, and intensity, let alone the SASP. Also, the mitochondrial status in the same cell seems to be paradoxical (e.g., higher respiration with lower membrane potential). In the last part, a summary is provided in the table to overview all those factors at once.

2.3.1 Mitochondria as an effector of CS: anterograde response

One of the early links between the mitochondrial effector role in the CS is derived from insights into oxygen tension. As now firmly established, the oxygen tension in tissues varies yet far from the ambient level (45). In 1977, it was found that culturing human diploid cells under 10% oxygen tension significantly extended the doubling potential of the cells (135). Two decades later was found that the replicative lifespan of the cells was even more extended—50% more compared to the ambient level—when the cells were cultured under 3% O₂ (136). In the same study, a simple treatment of a free radical scavenger was proven to extend the replicative lifespan of those cells cultured under the ambient oxygen tension. Subsequently, it was found that ROS accelerates the telomere attrition (137). Given

that the major source of cellular ROS is mitochondria, mitochondrial ROS (mtROS) was likely attributed to the observed replicative lifespan. However, it was not proven until the advent of technology to selectively scavenge the mtROS. The experimental evidence showed that MitoQ, the mtROS scavenger, extended the doubling potential by preventing accelerated telomere erosion (138). Moreover, a mild OXPHOS uncoupler reduced the mtROS and prolonged the replicative lifespan (139). This was also found to be true *in vivo*. *Ercc1*^{-Δ} mice with reduced expression of ERCC1-XPF endonuclease have impaired DNA repair capacity. This causes spontaneous DNA damage and the CS, leading to diverse phenotypes of premature aging (140). In this mouse model, a long-term administration of a mitochondria-targeted ROS scavenger delayed many premature aging symptoms with a concomitant reduction of senescent cells (141). These experiments established the role of mtROS in the CS. However, the mitochondrial scavengers never prevent the CS but simply delayed its manifestation. This demonstrates that mitochondrial ROS is an effector to accelerate the CS when combined with genotoxic stimuli.

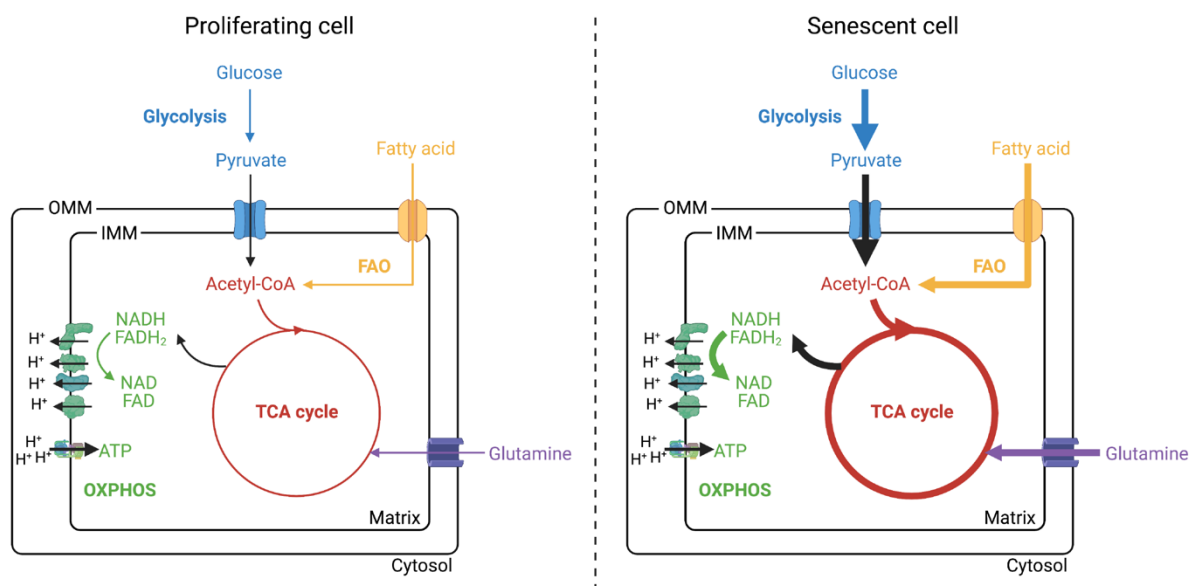
When it comes to the mitochondrial morphology and dynamics in senescent cells, there is not much disagreement. Numerous studies reported that the abundance of mitochondria is significantly increased with hypertubulated and often, clumped morphology in nearly all types of observed senescent cells, regardless of the triggers (21, 22, 139, 142-151). To name a few, in the replicative senescent human umbilical vein endothelial cells (HUVEC), the mitochondria are elongated with decreased expression of fission factors DRP1 and FIS1 (145). Interestingly, not only fission but also fusion events were decreased to a similar degree, indicating an overall reduction of the dynamics (146). A time-course study of mitochondria directly confirmed its reduced dynamics during the development of IR-induced senescent fibroblasts (152). However, the IR-induced senescence has a complication since the IR also inflicts damage on the mtDNA (153). This makes it unable to rule out the causative role of mitochondria in such settings. Similar observations were obtained from senescent epithelial cells and fibroblasts evoked by cigarette smoke extract (CSE) (142, 143, 147). The reason for the increased mitochondrial mass is largely considered due to the impaired mitophagy together with altered autophagy in senescent cells (154, 155). Mitophagy is generally regulated by the PTEN-induced kinase 1 (PINK1) and E3 ubiquitin ligase Parkin (PRKN) pathway (156). When mitophagy is activated, the PINK1 is stabilized and activates PRKN at the OMM. Then, PRKN ubiquitylates proteins at OMM, which facilitates the formation of autophagosomes. A study showed that cigarette smoking induces the CS significantly more in the PRKN whole-body knockout mouse lung (143). Another study showed that old mouse muscle stem cells displayed impaired mitophagy (155). Of note, it has been shown that mitochondrial turnover is reduced under the condition of impaired mitophagy, accompanied by a higher mtROS level and lower MMP. Thus, it is likely to be the accumulated 'old'

mitochondria in senescent cells that contribute to the senescent phenotypes (154). However, the dynamics *per se* does not appear to be a major contributor based on the effect size of the CS that it can yield (see 2.3.2 last paragraph). Also, it is not well understood how morphology can affect the function of mitochondria.

Lastly, mitochondrial metabolism has been shown to be a critical regulator of CS. The pyruvate dehydrogenase (PDH) complex converts pyruvate to acetyl-CoA in the mitochondrial matrix so that the glucose-driven carbons can be utilized through the TCA cycle. In the OIS fibroblasts by oncogenic BRAF, the PDH complex was found to be a rate-limiting factor (17). When the PDH complex was inhibited by multiple means, the cells reached senescence strikingly less under the oncogenic BRAF stimulus, which in turn licensed both melanoma development and maintenance. The activation of the PDH complex in the OIS resulted in a higher OCR accompanied by a higher cellular ROS level. Although quiescent cells also showed a higher flux of glucose carbon into the TCA cycle, it did not entail the elevated activity of the PDH complex. This suggests the OIS mechanism lies in the activity of the PDH complex *per se*, rather than the mitochondrial respiration. Of note, the PDH complex requires NAD as a cofactor. This raised the possibility of whether the NAD/NADH ratio could affect the OIS. Indeed, another subsequent study demonstrated that NAD/NADH ratio is a rheostat for the proinflammatory SASP expression in different types of CS (157). The OIS by oncogenic RAS, unlike the RS, elevated the expression of NAMPT, the rate-limiting enzyme of the NAD salvage pathway, through an HMGA1-mediated epigenetic mechanism. This resulted in an enhanced NAD/NADH ratio, accompanied by increased glycolysis and OCR. When NAD/NADH ratio is lowered by several means in the OIS, the proinflammatory SASP expression was markedly diminished. It turned out that lowering the NAD/NADH ratio hinders the enhancement of glycolysis and OCR, resulting in a higher ADP/ATP ratio in the OIS. Subsequently, AMPK-p53 signaling is activated which is known to suppress the SASP (27). Thus, the study suggests NAD/NADH ratio governs the strength of proinflammatory SASP, raising an alert to the NAD supplementation for anti-aging regimen (157). Given that mitochondrial CI is one of the major sources of NAD regeneration, this study implicates that elevated mitochondrial respiration in the RAS OIS is to support the SASP expression via the NAD regeneration. However, unlike BRAF OIS, it did not block the senescence *per se*, suggesting a differential regulation between the OIS evoked by RAS and RAF. Recently, not only glucose but also glutamine metabolism was found to be enhanced to ensure the survival of senescent cells (158). Glutamine is primarily catabolized in the mitochondria by glutaminase (GLS1 or GLS2). In the SIS fibroblasts by doxorubicin or p53 activation, the glutaminolysis was found to be increased. This was mainly relevant to cellular pH homeostasis rather than its well-known role of anaplerosis in the TCA cycle. Inhibition of glutaminolysis selectively killed senescent cells by disrupting the cellular pH both

in vitro and *in vivo* and ameliorated age-related phenotypes in old mice. Thus, glutaminolysis is a new senolytic target to kill senescent cells. As a last, fatty acid β -oxidation (FAO) was also found to be activated in the OIS fibroblasts (159). The FAO takes place in the mitochondria. The fatty acids are conjugated with carnitines in the cytosol and imported into the mitochondria through carnitine O-palmitoyltransferase 1 (CPT1), which is a rate-limiting enzyme of the FAO. After being imported, they are oxidized to acetyl-CoA by a series of β -oxidation. The OIS fibroblasts increased the OCR in a FAO-dependent manner. The reduction of the OCR by the FAO inhibition yielded blunted SASP expressions such as IL6 and IL8 but intriguingly not senescence itself, providing another example of selective regulation of the SASP. In another study, the proteomic analysis of senescent murine metastatic melanoma cells induced by etoposide identified FAO and TCA cycle genes as the most significantly enriched pathways (160). This was accompanied by an increased import of lipids including sphingomyelin, ceramide, and fatty acids, which resulted in more neutral lipid droplets and cellular aldehydes, suggesting a massive alteration of lipid metabolism in the TIS cells.

All in all, the senescent cells are accompanied by increased mitochondria with the higher mtROS level and the lower MMP, the higher OCR from the higher TCA cycle activity by the enhanced activity of the PDH complex, the FAO, and the glutaminolysis to support the senescence, the survival of senescent cells, and the SASP expression.



2.3.1 Mitochondrial metabolism in senescent cells

The oxidation of glucose, fatty acids, and glutamine is enhanced in diverse types of senescent cells. The width of arrows denotes an intensity of flux.

2.3.2 Mitochondria as a cause of CS: retrograde response

Besides the CS-accelerating role of the mtROS, several studies showed that mtROS as such could be a sufficient driver of the CS, regardless of the telomere shortening. The most compelling evidence came from the *in vivo* study of a mitochondrial antioxidant gene. Superoxide dismutase 2 (SOD2) is a mitochondrial matrix enzyme that detoxifies the mitochondrial superoxide to hydrogen peroxide. In whole-body *Sod2*^{-/-} mice, the appearance of senescent cells was accelerated in the epidermis which was positive for DNA damage and p16^{lnk4a} expression (161). This was recapitulated in mice with conditional *Sod2* knockout in the epidermal stem/progenitor cells (162). Another study showed it is sufficient to elicit the CS that putting cells under mtROS-elevating conditions such as CI inhibition by rotenone or CIII inhibition by stable knockdown of Rieske sulfur protein (RISP) (150). However, it was disputed later that mtROS is not a causal mediator of premature senescence at least in rotenone-treated conditions because the mitochondrial-selective ROS scavenger did not block the CS nor was there evidence of elevated mtROS when normalized by the increased mitochondrial mass, which hinted the importance of a normalization unit (163). A subsequent study made it more controversial by proving that mtROS alone can induce CS (164). In the study, mtROS was elevated directly by mitochondrial-targeted redox cycler MitoParaquat. 8 days of treatment of MitoParaquat was sufficient to induce the CS and the SASP. Perhaps, this apparent discrepancy is attributable to the amplitude of mtROS signaling which is often neglected in the experimental settings.

Other than the mtROS, general mitochondrial dysfunction was shown to be sufficient to drive the CS. A landmark study showed that stable knockdown of mitochondrial deacylase SIRT3 or SIRT5, or mitochondrial chaperone HSPA9 all induced the CS in 10 days (163). Of note, this was not due to the enzymatic activity of SIRT3, implicating an unknown function of SIRT3 in this observation. Likewise, the inhibition of CI or CIII rendered cells senescent after 10 days. Furthermore, the authors expanded it to cells depleted with mtDNA (*rho0* cells). It has been known that *rho0* cells require pyruvate and uridine for them to proliferate in culture. Upon pyruvate withdrawal, *rho0* cells were senesced in 7 days. Thus, the stress-induced mitochondrial dysfunction, in general, appears to elicit the CS and is hence termed mitochondrial dysfunction-associated senescence (MiDAS). What was striking about MiDAS is that the cells secreted little or no IL6, the classic SASP factor. Moreover, the MiDAS cells had a very different SASP gene expression profile. For example, senescent cells induced by SIRT3 knockdown did not express the core SASP genes including IL1A, IL1B, IL6, IL8, MMP3, and VEGF. In the subsequent experiments, it turned out that the cytosolic NAD/NADH ratio is a critical mediator of the MiDAS, although it remained unclear how general mitochondrial dysfunctions could lead to a cytosolic-specific imbalance of NAD/NADH ratio. Lowered NAD/NADH ratio was accompanied by an increased ADP/ATP ratio which in turn activated AMPK-p53 signaling and

thereby drove the CS. Of note, certain aspects of the MiDAS were found in POLG^{D257A} mice. POLGD^{257A} is a loss-of-function mutation of the mtDNA polymerase and this mutator mouse model garnered enormous attention because of the premature aging phenotypes (165). Senescent cells were found significantly more in the adipose tissue of the mutator mice with lower NAD/NADH ratio and lack of Il1a, Il1b, and Il6 expression, which are the MiDAS characteristics. Thus, it would be interesting to check whether clearance of MiDAS cells could ameliorate the aging phenotypes in the mutator mice.

There are several studies regarding mitochondrial dynamics as a sufficient driver of CS. In a study, a direct silencing of FIS1 induced Chang cells to be senescent associated with a decreased MMP (166). Nevertheless, 30% of the whole population at most became senescent. This was the same in the stable knockdown of E3 ubiquitin-protein ligase MARCHF5. MARCHF5 ubiquitylates MFN1 and facilitates its degradation via the proteasome. Chang cells with a stable knockdown of MARCHF5 exhibited elongated mitochondria, albeit less than 30% of the total population became senescent (167). There is another study that ectopic overexpression of the DRP1 loss-of-function mutant faithfully induces the CS (149). However, it remains to be seen how much it represents its loss of function without involving intact DRP1. These data collectively suggest the mitochondrial elongation commonly observed in senescent cells is not a significant driver of the CS.

2.3.3 Overview of the current findings of mitochondrial features in CS

Cell type	Trigger	mt ROS	MMP	Mitochondrial respiration	mtDNA	Normalization unit	Reference
HDF	BRAF ^{V600E}	N/A	N/A	Up	N/A	Cell number	(17)
HDF	RAS ^{G12V}	N/A	N/A	Up	N/A	Unknown	(168)
MEF	Ras ^{G12V}	N/A	N/A	Up	N/A	Unknown	(168)
HDF	RAS ^{G12V}	Up	Down	N/A	Up	Cell number	(150)
HDF	RAS ^{G12V}	N/A	N/A	Up	N/A	Cell number	(159)
HDF	RS	N/A	Down	Up	N/A	Cell number	(169)
HDF	RS	N/A	N/A	Up	N/A	Cell number	(154)
HDF	RS	N/A	Up	Same per mtDNA	Up	Cell number	(170)
HDF	RS	Up	Down	N/A	Up	Cell number	(139)
HDF	DNA damage	Up	Down	Up	N/A	Cell number	(21)
Lymphoma cell	DNA damage	N/A	N/A	Up	N/A	Unknown	(168)
RPE	DNA damage	N/A	Up	Same per mtDNA	Up	Cell number	(170)
Chang (HeLa)	Iron chelator	N/A	N/A	Down	Down	Cell number	(171)
HDF	MiDAS	Same	N/A	N/A	N/A	Mitochondrial mass	(163)
Chang (HeLa)	Mito elongation	N/A	Down	N/A	N/A	Cell number	(166)
Chang (HeLa)	Mito elongation	N/A	Down	N/A	N/A	Cell number	(167)

*HDF: human diploid fibroblast, *MEF: mouse embryonic fibroblast, *RPE: retinal pigment epithelium, *RS: replicative senescence, *mtROS: mitochondrial ROS, *MMP: Mitochondrial membrane potential, *mtDNA: mitochondrial DNA, *MiDAS: mitochondrial dysfunction-associated senescence, *N/A: not applicable (not measured)

2.4 Mitochondrial orphan gene OCIAD2

In 2001, ovarian cancer immunoreactive antigen domain 1 (OCIAD1) was first identified in an attempt to find immunoreactive antigens from the patient ascites fluid of ovarian cancer (172). Later, it was found to be overexpressed in metastatic ovarian cancer patient samples compared to non-metastatic primary ones and hence officially named OCIAD1 (173). In the meantime, OCIAD2 was identified based on the sequence homology to the OCIAD1 (174), despite the lack of evidence that it is involved in ovarian cancer at the time. OCIAD2 is a poorly characterized gene. It is comprised of 154 amino acids and is evolutionarily present only after the metazoans such as amphibians, fish, and birds, indicating its late evolution and perhaps tailored function in animal biology (175). Several studies reported OCIAD2 to be localized in multiple organelles such as endosomes, mitochondria, and mitochondrial-associated membranes (175-179). One of the first reports found it to be overexpressed in the lung adenocarcinoma at a highly malignant, advanced stage (180). Subsequent studies reported that OCIAD2 is generally more expressed in advanced cancer and thereby identified it as a malignancy biomarker (181-183). However, as it is unclear whether it is a cause or consequence of carcinogenesis, the expression of OCIAD2 was correlated with the survival and prognosis of the cancer patients in a context-dependent manner (180, 181, 184-187). Other than cancer, it was reported that OCIAD2 is expressed in the mouse cerebellum in a cell-type-specific manner, which reiterates its potentially tailored function and tight regulation (188). Another study identified OCIAD2 as a γ -secretase activator for enhanced amyloid β production in neuroblastoma cells (177), suggesting its possible role in neurobiology.

When it comes to insights into its function, it is significantly hampered by a scant amount of solid evidence. It was originally suggested to be an agonist of signal transducer and activator of transcription 3 (STAT3) signaling together with OCIAD1 (175). However, this observation was not reproducible (189). Recently, two conflicting reports were published regarding its function. In one study, OCIAD2 was reported to be an assembly factor of ETC CIII dimerization (178). Silencing OCIAD2 resulted in the lack of CIII dimerization, a mild decrease in maximal respiration, and mitochondrial fragmentation. However, none of these parameters was rescued by the complementation of OCIAD2, raising a concern that the observed phenotypes were off-target effects. In line with this, another report convincingly showed that OCIAD1, but not OCIAD2 facilitates the CIII assembly (179). In this study, a genome-wide CRISPRi screening identified OCIAD1 as a determinant of CIII assembly. The screening results were validated thoroughly in cells with each OCIAD1 and OCIAD2 single loss-of-function as well as dual loss-of-function. Regardless of OCIAD2 status, the observed defect in CIII

assembly was reproduced in OCIAD1-silenced cells. Thus, a *bona fide* function of OCIAD2 remains to be elucidated.

Lastly, three reports are available about its upstream regulator. Recently, it was shown that the abundance of OCIAD2 is regulated by mitochondrial m-AAA protease YME1L1 and thereby proposed as its substrate (190). YME1L1 has a pleiotropic role in cell biology through the regulation of its diverse set of substrates. As of yet, there is nothing known about the role of YME1L1 through OCIAD2 regulation. In the other report, OCIAD2 was identified as a downstream gene to TGF- β signaling from the time-resolved proteomic analysis (191). OCIAD2 was robustly increased upon TGF- β treatment as early as 6 hours in immortalized keratinocytes. It was one of the highest upregulated proteins among the previously unidentified genes in the TGF- β signaling, bolstering the robustness of the finding. In parallel, a bioinformatic study also suggested a possible link between OCIAD2 and the TGF- β signaling (192).

3. Aim of the thesis

As introduced, there are emerging evidence of mitochondrial role in cellular senescence. Considering mitochondria and cellular senescence are two important factors of aging, a thorough understanding of their relationship warrants a closer step to the actionable intervention. However, the exact mitochondrial status described in previous studies is not well compatible with each other. Moreover, the mitochondrial status even within the same study is not congruent. For example, the dysfunctional mitochondria as suggested exhibit higher respiration with lower membrane potential. Moreover, the mitochondrial metabolism is shown to be crucial in cellular senescence, arguing a necessity of functional mitochondria.

In this study, I first aim to define the mitochondrial status in senescent cells with a particular emphasis on the accurate quantification of their increased mass, based on the hypothesis that the mitochondrial mass is the key factor to reconcile the paradoxical status of mitochondria. Secondly, I aim to characterize mitochondrial proteome in a time-resolved manner during the development of cellular senescence, based on the hypothesis that such a forward approach with the temporal dynamics will reveal key regulatory pathways of cellular senescence laid in mitochondria. Lastly, I aim to test the role of the mitochondrial gene(s) identified from the proteomic analysis in order to find novel mitochondrial regulators in cellular senescence and thereby provide a testable target for senotherapy.

4. Materials and Methods

All the original data including proteomics and metabolomics are duly stored in the internal server of Max Planck Institute for Biology of Ageing and accessible with authority.

4.1 Cell biology

Cell cultures and chemicals

The human lung fibroblast IMR90 with population doublings (PD) 25-30 was obtained from ATCC (CCL-186) and maintained in the Minimum Essential Medium (Thermo; 41090) supplemented with 9.5% FBS (Sigma; F7524). IMR90 was cultured in the incubator under 3% O₂, 5% CO₂ and 92% N₂ and cells with SA- β -Gal positivity less than 10% of the population were used in all experiments. Upon the induction of TIS, the media were replaced every other day so that the nutrient availability does not become a limiting factor to drive TIS. HEK293T cells for lentivirus production were maintained in DMEM (Thermo; 61965) supplemented with 9.5% FBS. All cells were cultured without antibiotics and routinely checked with mycoplasma contamination and had never been positive. The cell number was calculated with trypan blue using Countess automated cell counter (Thermo). The chemicals used in the cell culture experiments are as follows: DMSO (Sigma; D2650), decitabine (Abcam; ab120842), doxorubicin (Sigma; D1515), bleomycin (Cayman; 13877). Decitabine was solved in DMSO and the rest in H₂O as stock solutions.

Establishment of therapy-induced senescence and replicative senescence

IMR90 or MRC5 cells were seeded on a diverse size of culture vessels with the density of 3,500/cm² for DMSO (0.01% v/v) and decitabine (1 μ M) treatment, or 7,000/cm² for doxorubicin (300 nM), bleomycin (10 μ g/mL) treatment. The next day, cells were treated with the compounds accordingly, then the media were replaced every other day until the harvest of cells. DMSO and decitabine were present in the media all times while doxorubicin and bleomycin was washed out in the first replacement of the medium. Unless denoted otherwise, the timing of cell harvest was synchronized to be 24 (\pm 3) hours from the last medium replacement and DMSO-treated cells were timely re-plated so that they did not reach the confluence by the time of harvest to maintain a proliferating state. All senescence assays were performed 7 days after the initial treatment, unless otherwise specified. Also, throughout the assay, all cells were cultured under 3% O₂ incubator except

for replicative senescence. IMR90 cells were routinely passaged in ambient 5% CO₂ incubator until it reached replicative senescence.

Cell proliferation assay

Cells were incubated with 10 μ M EdU in DMSO for 24 hours since the population doubling time is around 24 hours under our culture conditions. Cells were collected by trypsinization and then processed according to the manufacturer's protocol of the kit (Thermo; C10634). The number of EdU positive cells was counted by flow cytometry (BD Biosciences; FACS Canto) under APC channel using conventional FSC/SSC gating criteria without a viability dye.

Measurement of mitochondrial membrane potential, superoxide, and polarized mitochondria

Cells were seeded on the 6-well plate with the density described above. At day 7, cells were collected by trypsinization and pelleted and then processed according to the manufacturer's protocol of mitoSOX (Thermo; M36008), TMRM (Thermo; M20036), and Mitotracker Deep Red FM (Thermo; M22426). Briefly, the collected cell pellets were resuspended in the 1 mL PBS with the mitoSOX (5 μ M), TMRM (20 nM), or Mitotracker Deep Red FM (50 nM) and incubated in the non-CO₂ incubator at 37°C for 20 min. Cells were pelleted and washed with PBS twice and DAPI (1 ng/mL) was added to select the live cells. Then cells were filtered through 50 μ m cell strainer and analysed by flow cytometry (BD Biosciences; FACScanto) in the PE channel with the conventional SSC/FSC gating strategy. Mean fluorescence intensity of the gated population was taken.

Stable cell line generation by lentivirus

HEK293T cells were seeded as 5x10⁶ per 10-cm dish in 8 mL medium. The next day, cells were transfected with the lentivirus plasmids according to the manufacturer's protocol (Takara; 631276). For OCIAD2 knockdown, 7 μ g shRNA plasmids (Sigma) targeting OCIAD2 (#1: TRCN0000130004, #2: TRCN0000131164, #3: TRCN0000128368, #4: TRCN0000318948) or non-targeting control (SHC202) were used. For OCIAD2 overexpression, pLenti-C-Myc-DDK-P2A-Puro (OriGene; PS100092 for control, RC222324L3 for OCIAD2) plasmids were used. The plasmids were diluted in 600 μ L H₂O, followed by mixing with the packaging plasmid tube. 10 min later, the generated liposomes were treated to HEK293T cells. The next day, 6 mL DMEM was carefully added to minimize the cell detachment. 48 hours after the transfection, the generation of lentiviral particle was confirmed by the kit (Takara; 631280) and the virus-containing medium was mixed with polybrene (5 μ g/mL, Sigma;107689) and added to the recipient IMR90 cells that were seeded one day

before as 10e6 per 10-cm dish. 1 day later the transduction, the medium was replaced with the polybrene-free MEM. Another day later, cells were trypsinized and replated on 15-cm dish with the medium containing puromycin (1.5 µg/mL, InvivoGen; ant-pr-1). 3 days later, the medium was replaced with the drug-free MEM and expanded for the subsequent experiments.

4.2 Biochemistry and molecular biology

Senescence-associated β galactosidase assay

Cells were washed twice with PBS and subject to SA-β-Gal assay using the kit (Abcam; ab65351) according to the manufacturer's protocol. The next day, the stained cells were washed twice with PBS and permeabilized by 0.2% TX-100/PBS for 5 min. After washing twice, DAPI (1 ng/mL) was added to count the number of cells. The images were taken under the DAPI channel and transparent channel using EVOS microscope (Thermo). At least 100 cells per condition were analyzed and the number of DAPI and SA-β-Gal positive cells was counted by eyes.

Quantification of mitochondrial volume

Cells were seeded on the coverslips and induced to be senescent. The DMSO-treated control cells were seeded as well the day before the assay. At day 7, cells were washed twice with PBS and fixed with 4% PFA (Santa Cruz; sc-281692) for 15 min at RT. After washing out PFA with PBS twice, cells were permeabilized with 0.2% TX-100 for 5 min at RT. Cells were washed twice again and incubated with the antibody against ATP5B (Invitrogen; A21351) diluted as 1:1000 in 1% BSA/PBS for overnight at 4°C. The next day, the primary antibody was washed out and the goat anti-mouse IgG (H+L) antibody conjugated with Alexa fluor 568 (Invitrogen; A11031) was treated as 1:1000 in PBS with Alexa Fluor 647 Phalloidin (Invitrogen; A22287) to stain the F-actin for the identification of a single cell. After 1 hour, DAPI (1 ng/mL) was added after washing out the secondary antibodies for 5 min and mounted on the slides with the mounting medium (Thermo; P10144). At least one day after the mounting, the images were taken by confocal microscope (Leica; SP8-DLS). Z-stack confocal images were taken with 0.2 µm interval from the bottom to the top of mitochondria. After a single cell was defined in each image based on the F-actin staining using the software Fiji (193), the stacks of 2-dimensional mitochondrial images were converted into the 3-dimensional model by Mitograph (194). Total length, average width and volume (by voxels) of mitochondria per cell were calculated by Mitograph.

Real time quantitative PCR (RT-qPCR)

RNA was harvested from the cells by the kit (Macherey-Nagel; 740955) and subject to cDNA synthesis with oligo(dT) reverse transcriptase (Promega; A2791). Target mRNA levels were quantified by $\Delta\Delta C_t$ values using TaqMan fast advanced master-mix (Thermo; 4444557) with the TaqMan probes as follows: B2M (Hs99999907_m1), IL1A (Hs00174092_m1), IL1B (Hs01555410_m1), IL6 (Hs00174131_m1), CXCL8 (Hs00174103_m1), CDKN1A (Hs00355782_m1), CDKN2A (Hs00923894_m1), LMNB1 (Hs01059210_m1), BCAT1 (Hs00398962_m1), BCAT2 (Hs01553550_m1), ISG15 (Hs00192713_m1), IFI44 (Hs00197427_m1), MX1 (Hs00895608_m1), MAVS (Hs00920075_m1), TMEM173 (Hs00736955_g1), MB21D1 (Hs00403553_m1), PGC1A (Hs00173304_m1), PGC1B (Hs00991677_m1). Fold change was calculated by B2M as the reference.

Quantification of mtDNA copy number difference

Cellular DNA was extracted from the cells using the kit (Qiagen; 69504) and mtDNA copy number was measured by TaqMan assay as described previously. Genomic DNA was measured by ACTB (Hs03023880_g1) and mtDNA was measured by two different probes (MT-ND1; Hs02596873_s1 and MT-7s; Hs02596861_s1). The mtDNA copy difference between conditions were calculated by $\Delta\Delta C_t$ values (MT-ND1/ACTB or MT-7s/ACTB).

Measurement of oxygen consumption rate (OCR)

Mitochondrial respiration was measured by XFe96 Seahorse analyser with mito stress test kit (Agilent; 103015) according to the manufacturer's protocol. Briefly, 2×10^4 (proliferating) and 3×10^4 (senescent) cells were seeded per well on XFe96 plate. The next day, cells were washed and incubated for 1 hour at 37°C in the non-CO₂ chamber with the assay medium (Agilent; 103575) supplemented with L-glutamine (2 mM) and D-glucose (5.5 mM). OCR was measured with subsequent injections of the following compounds (Oligomycin 1 μ M, FCCP or CCCP 0.5 μ M, Rotenone+Antimycin A 0.5 μ M each). After the assay, cells were washed once with PBS and lysed in 25 μ L of SDS buffer (50 mM Tris-HCl pH 7.4, 1% SDS), followed by the protein quantification. The data were normalized according to the cell number calculated from the protein quantity with the scaling factors of protein to cell number ratio. Diverse parameters of mitochondrial functions were calculated by the Seahorse XF report generator (Agilent).

Mitochondrial translation assay

Cells were seeded and treated with DMSO, Decitabine or Doxorubicin on the 6-well plates as described previously. At day 7, cells were incubated for 30 min in the glutamine/methionine/cysteine-free DMEM (Thermo; 21013) supplemented with 100 µg/mL Emetine to block the cytosolic translation. Then, 50 µCi ³⁵S-methionine/cysteine mix (Hartmann Analytic; SCIS-103) was added to the wells and incubated for 1 hour. The cells were washed twice with DPBS and lysed in RIPA buffer and cleared out by 21,000 g for 10 min at 4°C. The equal quantity of proteins was run on 12% Tris-Tricine SDS-PAGE and transferred to nitrocellulose membrane. The membrane was dried in the air and the radioactive signals were captured to the storage phosphor screen for 3 days. Upon laser-induced stimulation, the captured signals on the screen were detected by the Typhoon phosphorimager (Cytiva Lifesciences).

Western blotting

Cells were washed once with PBS and lysed by the RIPA buffer (25 mM Tris-KOH pH 7.4, 140 mM NaCl, 1% TX-100, 0.1% SDS, 0.5% sodium deoxycholate, 5 µM EDTA pH 7.4) and scraped. The lysates were centrifuged at 21,000 g for 20 min at 4°C and the proteins were quantified by BCA assay kit. The lysate with the equal quantity of proteins was mixed with the sample buffer (Thermo; NP0008) and subject to bis-tris SDS-PAGE with MOPS buffer and transferred to PVDF membrane by the wet transfer. The membranes were blocked for 1 hour at RT with 5% skim milk diluted in TBS with 0.1% Tween20, followed by the incubation with corresponding primary antibodies for overnight at 8°C. The next day, membranes were washed 3 times with TBS-T and incubated with HRP-conjugated secondary antibodies for 1 hour at RT. Membranes were washed 3 times again and developed using ECL chemistry (Advansta; K-12045-D50 or Thermo; 34096) under the digital detector (INTAS; ChemoStar Touch ECL). All antibodies were diluted in 3% BSA in TBS-T containing 0.02% sodium azide. The following antibodies were used: BCAT2 (ProteinTech; 16417-1-AP), BCAT1 (ProteinTech; 13640-1-AP), BCKDHE1A (CST; 90198), phospho-BCKDHE1A (Abcam; ab275961), MT-CO1 (Abcam; ab14705), MT-CO2 (Invitrogen; A6404), MT-ATP6 (ProteinTech; 55313-1-AP), SDHA (Abcam; ab14715), OXPHOS cocktail (Abcam; ab110413), TUBA (Sigma; T6074), ACTB (Sigma; A5441), p21 (CST; 2947), LMNB1 (Abcam; ab16048).

Isolation of mitochondria

Preparation of mitochondria-enriched membrane organelle was done as described with a few modifications (195). Briefly, cells with around 80% confluence on five 15-cm dishes were collected by scraping and washed with ice-cold PBS twice. All subsequent steps were performed at 4°C. The

cells were incubated for 10 min in the isotonic buffer (10 mM HEPES pH 7.4, 225 mM Mannitol, 75 mM Sucrose, 1 mM EGTA pH 7.4). Then, the cells were lysed with 1 mL syringe with 27 G needle by passing through the needles for 10 times. The lysates were spun down by 600 g for 5 min. The supernatants were centrifuged by 7,000 g for 10 min, followed by washing steps with the isotonic buffer for 3 times. The final pellets containing membrane organelles without cytosolic fraction were resuspended in the 200 μ L isotonic buffer.

Immunoprecipitation of OCIAD2 binding partners

IMR90 cells with or without expressing ectopic OCIAD2^{Myc-FLAG} were seeded as 2x10⁵ per 15-cm dish. Six dishes were prepared per genotype. The next day, 1 μ M decitabine or 0.1% DMSO was treated. At day 7, cells were subject to mitochondrial isolation as stated above. The experiments were repeated four times independently. The resulting 16 mitochondria-enriched fractions (2 genotypes x 2 treatments x 4 replicates) were altogether subject to immunoprecipitation using FLAG magnetic beads (Thermo, A36798) and the corresponding magnet stands (Thermo, 12321D) for washing steps. Briefly, 300 μ g of mitochondrial fraction was pelleted and lysed in 150 μ L lysis buffer (20 mM HEPES pH 7.4, 150 mM NaCl, 0.8% digitonin) by resuspending the pellets about 20 times and incubate under 8°C with rotation (10 rpm, 15 min). Then, the lysates were spun down (20,000 g, 10 min at 4°C) and 150 μ L supernatant was mixed with 20 μ L processed FLAG magnetic beads. The beads were processed in advance as follows: 350 μ L beads were washed 3 times with 1 mL H₂O and resuspended in 200 μ L lysis buffer. Then another 150 μ L lysis buffer was added to make 320 μ L in total. The mixture was rotated overnight (10 rpm, 8°C). The next day, the beads were washed 3 times with 1 mL wash buffer (identical to the lysis buffer instead 0.1% digitonin). The beads were then washed 3 times with 1 mL wash buffer without detergent to get rid of all the residual detergent before elution. Finally, the beads were eluted in 100 μ L elution buffer (50 mM Tris-HCl pH 7.4, 1 mM TCEP, 5 mM CAA, 5 ng/ μ L trypsin) for 20 min at room temperature with occasional vortex. Then the beads were left in 37°C water bath overnight. The next day, they were directly subject to peptide preparation for the proteomics analysis.

4.3 Mouse experiments

Generation of Ociad2 whole-body knockout mice

The generation was performed by Dr. Simon Tröder at the CECAD animal facility, according to the animal regulations. Mouse embryos were subjected to CRISPR-Cas9 gene editing technology. In detail,

the embryos were injected with small guide RNA, single strand deoxynucleotide (ssODN) as a donor template targeting exon 4, and cas9 expression plasmid. The exact sequence of each molecule is described in the attached DNA sequence file. After selecting successful edited embryos, the newly born animals were backcrossed twice to remove the unwanted genetic background variance. Validation of the correct genotype was performed sequence-based method after amplifying the targeted region. The exact primer sequence for genotyping is included in the attached DNA file as well.

OCIAD2 immunoblot from the Yme111 CNS-specific knockout mice tissues

For the result 5.2.9c, the mice tissues were collected from the previously published experiments (196).

4.3 Proteomics and metabolomics

Proteomics: peptide preparation

Cells were seeded on 15-cm dishes and the next day treated with either DMSO or Decitabine. At day 1, 3, 5, and 7, cells were collected by scraping and washed with PBS twice. In all conditions, cells were seeded adequately so that they reached around 80% confluence by the time of collection. The cell pellets were then resuspended in 15 μ L of lysis buffer (6 M guanidinium chloride, 2.5 mM tris(2-carboxyethyl)phosphine, 10 mM chloroacetamide, 100 mM tris-hydrochloride) and heated at 95°C for 10 min. The lysates were sonicated (30 sec/30 sec, 10 cycles, high performance) by Bioruptor (Diagenode; B01020001), followed by centrifugation at 21,000 g for 20 min at 20°C. 200 μ g of supernatants were digested by 1 μ L trypsin (Promega; V5280) for overnight at 37°C. The next day, formic acid (to be 1%) was added to the digested peptide lysates to stop the trypsin digestion and desalted by home-made STAGE tips (197). The eluted lysates in 60% acetonitrile/0.1% formic acid were dried by the vacuum centrifugation (Eppendorf; Concentrator Plus) at 45°C.

Proteomics: TMT labeling

4 μ g of desalted peptides were labeled with tandem mass tags TMT10plex (Thermo; 90110) using a 1:20 ratio of peptides to TMT reagent. TMT labeling was carried out according to manufacturer's instruction with the following changes: dried peptides were reconstituted in 9 μ L 0.1 M TEAB to which 7 μ L TMT reagent in acetonitrile was added to a final acetonitrile concentration of 43.75%, the reaction was quenched with 2 μ L 5% hydroxylamine. Labeled peptides were pooled, dried, resuspended in 0.1% formic acid, split into two samples, and desalted using home-made STAGE tips (197).

Proteomics: high-pH fractionation

Pooled TMT labeled peptides were separated on a 150 mm, 300 μm OD, 2 μm C18, Acclaim PepMap (Thermo) column using an Ultimate 3000 (Thermo). The column was maintained at 30°C. Separation was performed using a segmented gradient from 1% to 50% buffer B, for 85 min and 50% to 95% for 20 min with a flow of 4 μL . Buffer A was 5% acetonitrile 0.01M ammonium bicarbonate, buffer B was 80% acetonitrile 0.01 M ammonium bicarbonate. Fractions were collected every 150 sec and combined into nine fractions by pooling every ninth fraction. Pooled fractions were dried in Concentrator plus (Eppendorf), resuspended in 5 μL 0.1% formic acid from which 2 μL analyzed by LC-MS/MS.

Proteomics: LC-MS/MS analysis

Dried fractions were re-suspended in 0.1% formic acid and separated on a 50 cm, 75 μm Acclaim PepMap column (Thermo; 164942) and analysed on a Orbitrap Lumos Tribrid mass spectrometer (Thermo) equipped with a FAIMS device (Thermo). The FAIMS device was operated in two compensation voltages, -50 V and -70 V. Synchronous precursor selection based MS3 was used for the acquisition of the TMT reporter ion signals. Peptide separation was performed on an EASY-nLC1200 using a 90 min linear gradient from 6% to 31% buffer; buffer A was 0.1% formic acid, buffer B was 0.1% formic acid, 80% acetonitrile. The analytical column was operated at 50°C. Raw files were split based on the FAIMS compensation voltage using FreeStyle (Thermo).

FLAG-IP proteomics: LC-MS/MS analysis

Peptides were separated on a 25 cm, 75 μm internal diameter PicoFrit analytical column (New Objective) packed with 1.9 μm ReproSil-Pur 120 C18-AQ media (Dr. Maisch,) using an EASY-nLC 1200 (Thermo). The column was maintained at 50°C. Buffer A and B were 0.1% formic acid in water and 0.1% formic acid in 80% acetonitrile. Peptides were separated on a segmented gradient from 6% to 31% buffer B for 57 min and from 31% to 44% buffer B for 5 min at 250 nl/min. Eluting peptides were analyzed on a Orbitrap Fusion Tribrid mass spectrometer (Thermo). Peptide precursor m/z measurements were carried out at 60000 resolution in the 350 to 1500 m/z range. The most intense precursors with charge state from 2 to 7 only were selected for HCD fragmentation using 27% normalized collision energy. The cycle time was set to 1 sec. The m/z values of the peptide fragments were measured at a resolution of 50000 using an AGC target of $2e5$ and 86 ms maximum injection time. Upon fragmentation, precursors were put on a dynamic exclusion list for 45 sec.

Metabolomics: metabolite preparation

Cells on 6-well plates were washed twice with the wash buffer (75 mM ammonium carbonate, pH 7.4) and the plates were flash frozen in the liquid nitrogen. 800 μ L extraction buffer (acetonitrile:methanol:H₂O=4:4:2, -20°C) was added to the wells, scraped and centrifuged by 21,000 g for 20 min at 4°C. The supernatants were dried by the vacuum centrifugation (Labogene) for 6 hours at 20°C while the pellets were used for protein quantification after lysed in the buffer (50 mM Tris-KOH pH 8.0, 150 mM NaCl, 1% SDS) by BCA assay (Thermo; 23225). Metabolomics samples to measure steady-state abundance were added with the following internal standards in the extraction buffer: 2.5 mM amino acids standard (Cambridge Isotopes; MSK-A2-1.2), 100 μ g/mL citrate d₄ (Sigma; 485438), 1 mg/mL ¹³C₁₀ ATP (Sigma; 710695). No internal standard was added for the isotopologue tracing experiments. Isotopologues used in the experiments are as following: ¹³C₅ L-glutamine (Sigma; 605166), ¹³C₆ D-glucose (Sigma; 389374), ¹³C₆ L-leucine (Sigma; 605239), ¹⁵N L-leucine (sigma; 340960), ¹³C₅ L-valine (Sigma; 758159), ¹⁵N L-valine (Sigma; 490172).

Anion-Exchange Chromatography Mass Spectrometry (AEX-MS) for the analysis of anionic metabolites

Extracted metabolites were re-suspended in 200 μ l of Optima UPLC/MS grade water (Thermo). After 15 min incubation on a thermomixer at 4°C and a 5 min centrifugation at 16.000 x g at 4°C, 100 μ l of the cleared supernatant were transferred to polypropylene autosampler vials (Chromatography Accessories Trott).

The samples were analysed using a Dionex ionchromatography system (Integrion, Thermo) as described previously. In brief, 5 μ L of polar metabolite extract were injected in full loop mode using an overfill factor of 1, onto a Dionex IonPac AS11-HC column (2 mm \times 250 mm, 4 μ m particle size, Thermo) equipped with a Dionex IonPac AG11-HC guard column (2 mm \times 50 mm, 4 μ m, Thermo). The column temperature was held at 30°C, while the auto sampler was set to 6°C. A potassium hydroxide gradient was generated using a potassium hydroxide cartridge (Eluent Generator, Thermo), which was supplied with deionized water. The metabolite separation was carried at a flow rate of 380 μ L/min, applying the following gradient conditions: 0-3 min, 10 mM KOH; 3-12 min, 10–50 mM KOH; 12-19 min, 50-100 mM KOH, 19-21 min, 100 mM KOH, 21-22 min, 100-10 mM KOH. The column was re-equilibrated at 10 mM for 8 min.

For the analysis of metabolic pool sizes the eluting compounds were detected in negative ion mode using full scan measurements in the mass range m/z 50 – 750 on a Q-Exactive HF high resolution MS (Thermo). The heated electrospray ionization (ESI) source settings of the mass spectrometer were:

Spray voltage 3.2 kV, capillary temperature was set to 300°C, sheath gas flow 60 AU, aux gas flow 20 AU at a temperature of 330°C and a sweep gas flow of 2 AU. The S-lens was set to a value of 60. The semi-targeted LC-MS data analysis was performed using the TraceFinder software (Version 4.1, Thermo). The identity of each compound was validated by authentic reference compounds, which were measured at the beginning and the end of the sequence.

For data analysis the area of the deprotonated (M-H⁺)- monoisotopic mass peak of each compound was extracted and integrated using a mass accuracy <5 ppm and a retention time (RT) tolerance of <0.05 min as compared to the independently measured reference compounds. Areas of the cellular pool sizes were normalized to the internal standards, which were added to the extraction buffer, followed by a normalization to the fresh weight of the analyzed sample.

Semi-targeted liquid chromatography-high-resolution mass spectrometry-based (LC-HRS-MS) analysis of amine-containing metabolites

The LC-HRMS analysis of amine-containing compounds was performed using an adapted benzoylchloride-based derivatization method.

In brief: The polar fraction of the metabolite extract was re-suspended in 200 µL of LC-MS-grade water (Optima-Grade, Thermo) and incubated at 4°C for 15 min on a thermomixer. The re-suspended extract was centrifuged for 5 min at 16.000 x g at 4°C and 50 µL of the cleared supernatant were mixed with 25 µl of 100 mM sodium carbonate (Sigma), followed by the addition of 25 µl 2% (v/v) benzoylchloride (Sigma) in acetonitrile (Optima-Grade, Thermo). Samples were vortexed and kept at 20°C until analysis.

For the LC-HRMS analysis, 1 µl of the derivatized sample was injected onto a 100 x 2.1 mm HSS T3 UPLC column (Waters). The flow rate was set to 400 µl/min using a binary buffer system consisting of buffer A (10 mM ammonium formate (Sigma), 0.15% (v/v) formic acid (Sigma) in LC-MS-grade water (Optima-Grade, Thermo). Buffer B consisted solely of acetonitrile (Optima-grade, Thermo). The column temperature was set to 40°C, while the LC gradient was: 0% B at 0 min, 0-15% B 0- 4.1 min; 15-17% B 4.1 – 4.5 min; 17-55% B 4.5-11 min; 55-70% B 11 – 11.5 min, 70-100% B 11.5 - 13 min; B 100% 13 - 14 min; 100-0% B 14 -14.1 min; 0% B 14.1-19 min; 0% B. The mass spectrometer (Q-Exactive Plus, Thermo) was operating in positive ionization mode recording the mass range m/z 100-1000. The heated ESI source settings of the mass spectrometer were: Spray voltage 3.5 kV, capillary temperature 300°C, sheath gas flow 60 AU, aux gas flow 20 AU at a temperature of 330°C and the sweep gas to 2 AU. The RF-lens was set to a value of 60.

Semi-targeted data analysis for the samples was performed using the TraceFinder software (Version 4.1, Thermo). The identity of each compound was validated by authentic reference compounds, which

were run before and after every sequence. Peak areas of $[M + nBz + H]^+$ ions were extracted using a mass accuracy (<5 ppm) and a retention time tolerance of <0.05 min. Areas of the cellular pool sizes were normalized to the internal standards ($[U]-^{15}N$; $[U]-^{13}C$ amino acid mix (MSK-A2-1.2), Cambridge Isotope Laboratories), which were added to the extraction buffer, followed by a normalization to the fresh weight of the analyzed sample.

Semi-targeted liquid chromatography-high-resolution mass spectrometry-based (LC-HRS-MS) analysis of Acyl-CoA metabolites

The LC-HRMS analysis of Acyl-CoAs was performed using an modified protocol based on the previous method. In brief: The polar fraction of the metabolite extract was re-suspended in 50 μ L of LC-MS-grade water (Optima-Grade, Thermo). For the LC-HRMS analysis, 1 μ l of the sample was injected onto a 30 x 2.1 mm BEH Amide UPLC column (Waters) with 1.7 μ m particle size. The flow rate was set to 500 μ l/min using a quaternary buffer system consisting of buffer A 5 mM ammonium acetate (Sigma) in LC-MS-grade water (Optima-Grade, Thermo). Buffer B consisted of 5 mM ammonium acetate (Sigma) in 95% acetonitrile (Optima-grade, Thermo). Buffer C consisted of 0.1% phosphoric acid (85%, VWR) in 60% acetonitrile (acidic wash) and buffer D of 50% acetonitrile (neutral wash). The column temperature was set to 30°C, while the LC gradient was: 85% B for 1 min, 85-70% B 1- 3min; 70-50% B 3 – 3.2 min; holding 50% B till 5 min; 100% C 5.1 – 8 min, 100% D 8.1 - 10 min; followed by re-equilibration 85% B 10.1 - 13 min. The mass spectrometer (Q-Exactive Plus, Thermo) was operating in positive ionization mode recording the mass range m/z 760-1800. The heated ESI source settings of the mass spectrometer were: Spray voltage 3.5 kV, capillary temperature 300°C, sheath gas flow 50 AU, aux gas flow 15 AU at a temperature of 350°C and the sweep gas to 3 AU. The RF-lens was set to a value of 55.

Semi-targeted data analysis for the samples was performed using the TraceFinder software (Version 4.1, Thermo). The identity of Acetyl-CoA and Malonyl-CoA was validated by authentic ^{13}C labelled reference compounds, which were run before. Other Acyl-CoAs were validated by using E.coli reference material matching exact mass and reporter ions from PRM experiments. Peak areas of $[M + H]^+$ ions and corresponding isotopomers were extracted using a mass accuracy (<5 ppm) and a retention time tolerance of <0.05 min.

4.4 Data analysis and statistics

All statistical analyses were performed by GraphPad Prism version 9.3.1. When two groups were compared, the welch t-test was used with a multiple comparison correction by the Bonferroni-Dunn method, if needed. When 3 or more groups were compared, ANOVA test was used. One-way

ANOVA was used for multiple groups under one condition and two-way ANOVA for them under two conditions. Then, each subject group was compared to the control group (e.g., DMSO, shNT) with a multiple comparison correction by the Dunnett method. *:p<0.05, **:p<0.01, ***:p<0.001.

For visualization of the results and figures, Biorender, GraphPad Prism, Flaski, or R was used as indicated elsewhere.

Proteomics: peptide identification and quantification

Proteomics data was analyzed using MaxQuant, version 1.5.2.8, (198). The isotope purity correction factors, provided by the manufacturer, were included in the analysis. Differential expression analysis was performed using limma version 3.34.9 (199) and R version 3.4.3 (200). Mitochondrial annotations were based on human MitoCarta 3.0 (176).

Proteomics: data analysis and visualization

Quantified proteomics data were investigated for the enrichment analysis including statistics by the String database (201) and the GSEA (202, 203). For the GSEA analysis, the background gmt files were made with the MitoPathways and localization information from the human MitoCarta 3.0. The total quantified 6482 proteins were used as a background. All graphs were drawn by either GraphPad Prism version 9.3.1 or R version 3.4.3.

Metabolomics: data analysis and visualization

79 quantified metabolites were normalized by the total ion counts (TIC) value. Differential abundance analysis from each comparison was calculated with fold changes in log₂ values by the welch t-test with correction using Bonferroni-Dunn method. For mass isotopologue experiments, the natural abundance of ¹³C was not corrected. All the statistical analysis and graphs were by GraphPad Prism version 9.3.1. For heatmap in appendix 4, Flaski was used (204).

5. Result

5.1 Forward genetics: characterizing mitochondria in therapy-induced senescence (TIS)

Among different types of senescence, I focused on *in vitro* TIS in this study for the following reasons:

- i) Unlike other types of senescence, its emergence is under controlled and defined conditions in the human body by chemotherapy. Thus, *in vitro* cell culture results would yield highly relevant implications to *in vivo* circumstances.
- ii) Chemotherapeutic agents have defined targets. This enables the interpretations of the outcomes with the least confounding factors. By its nature, it also provides highly reproducible results *in vitro*.
- iii) There are not many tools to study CS *in vivo* yet. The biggest obstacle is the lack of a non-invasive marker that universally detects senescent cells in the body.

5.1.1 Establishment of TIS by anti-cancer drugs in IMR90 fibroblasts

As a model of *in vitro* TIS, IMR90 human lung fibroblasts were treated with two chemotherapeutic agents, decitabine and doxorubicin as both have been well-known drugs to induce TIS. Decitabine is a deoxycytidine analogue to cause epigenetic stress, a loss of DNA methylome, due to the substitution of carbon with methylation-incapable nitrogen at 5' position when incorporated into proliferating cellular DNA (Figure 5.1.1 A). On the other hand, doxorubicin blocks topoisomerase II to cause DNA double-strand break and hence DDR. As expected, IMR90 treated with decitabine or doxorubicin became senescent 7 days later, evidenced by the mRNA level of increased CDKN1A and CDKN2A, decreased LMNB1, and increased SASP factors IL1A and IL6 (Figure 5.1.1 B-C). The cells were with little or no cell-cycle activity (Figure 5.1.1 D) and 60-70% of the cell population was SA- β -gal positive (Figure 5.1.1 E-F). Another general feature of CS is that the amount of cellular protein is increased. This was the case in TIS fibroblasts (Figure 5.1.1 G), and hence the cell : protein ratio in TIS fibroblasts shall be a critical scaling factor for comparison between non-senescent cells to senescent cells since protein amount is generally used as a reference for normalization.

In conclusion, a condition is established that both decitabine and doxorubicin induce the TIS in IMR90 human lung fibroblasts.

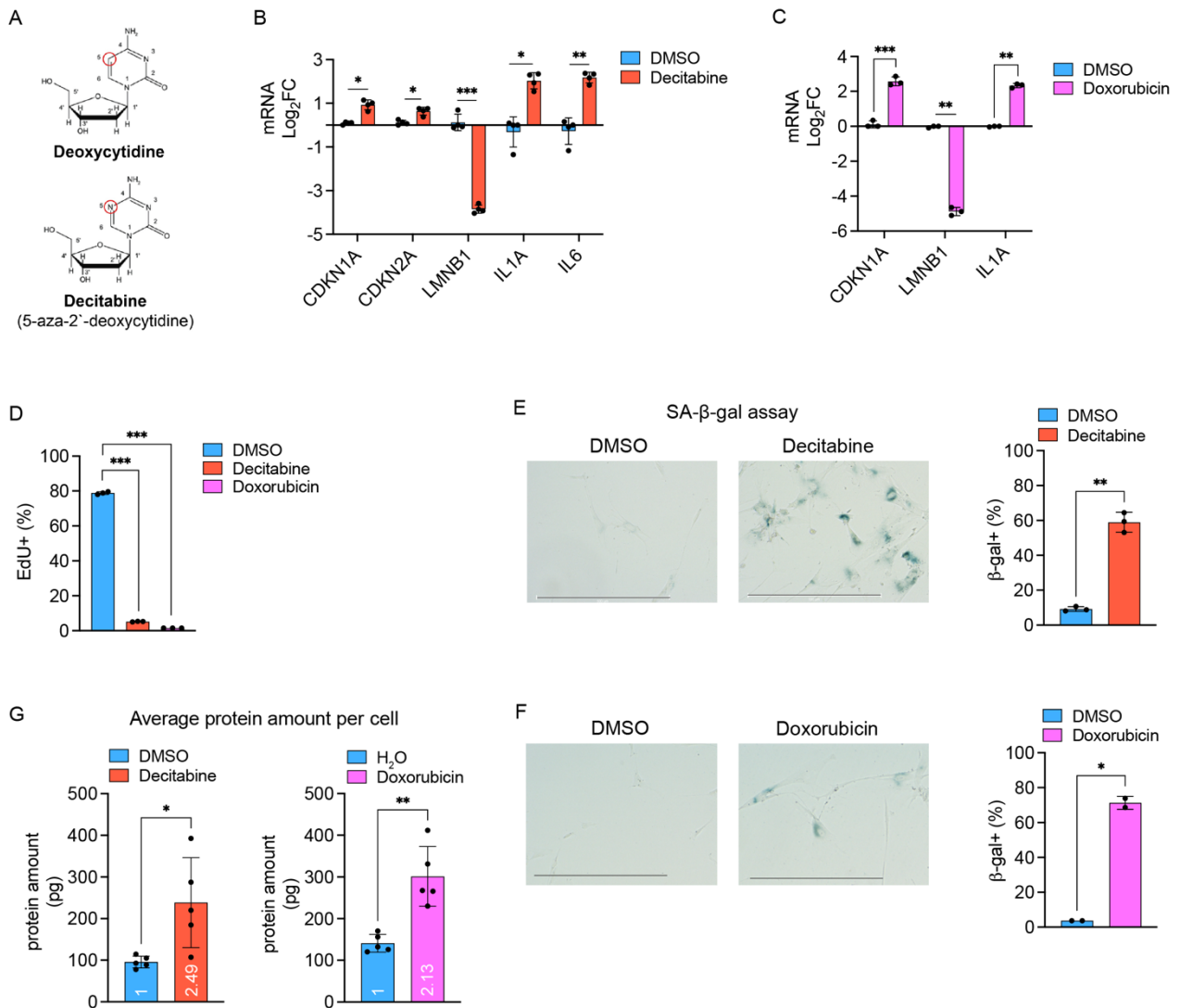


Figure 5.1.1 Establishment of TIS in IMR90

(A) Structure of deoxycytidine and decitabine. (B-G) IMR90 cells were treated with compounds as specified for 7 days.

(B, C) mRNA levels were measured by RT-qPCR. Welch t-test, Bonferroni-Dunn correction. n=4 (B), n=3 (C).

(D) EdU positive population. One-way ANOVA, Dunnett correction. n=3

(E, F) SA-β-gal assay. Counted were at least 50 cells per replicate in each condition. Scale bar 500 μm. Welch t-test. (E) n=3, (F) n=2.

(G) Protein amount per cell. Average fold change was denoted within the bar. Welch t-test. n=5

5.1.2 Profound increase of mitochondrial abundance in a TIS fibroblast

Although it has been repeatedly shown that an amount of mitochondria is increased in senescent cells, it is less known about the accurate mitochondrial volume considering 3-dimensional space. Hence firstly quantified was the increased mitochondrial volume per cell. Immunofluorescent images taken by confocal microscopy encompassing the whole focal planes from the very bottom to the top of mitochondria were rendered into 3-D images using the software MitoGraph. The OXPHOS subunit ATP5B was used to stain mitochondria harnessing its ubiquitous expression throughout

mitochondria while F-actin to identify a single cell (Figure 5.1.2 A). As a result, it was found that the total length of mitochondria is remarkably increased without a difference in average width, which led to over a 12-fold increase in mitochondrial volume per TIS fibroblast compared to proliferating cell (Figure 5.1.2 B). Such an increase would be another important scaling factor to understand the relative mitochondrial activity per mitochondrion in the TIS fibroblast compared to the proliferating one.

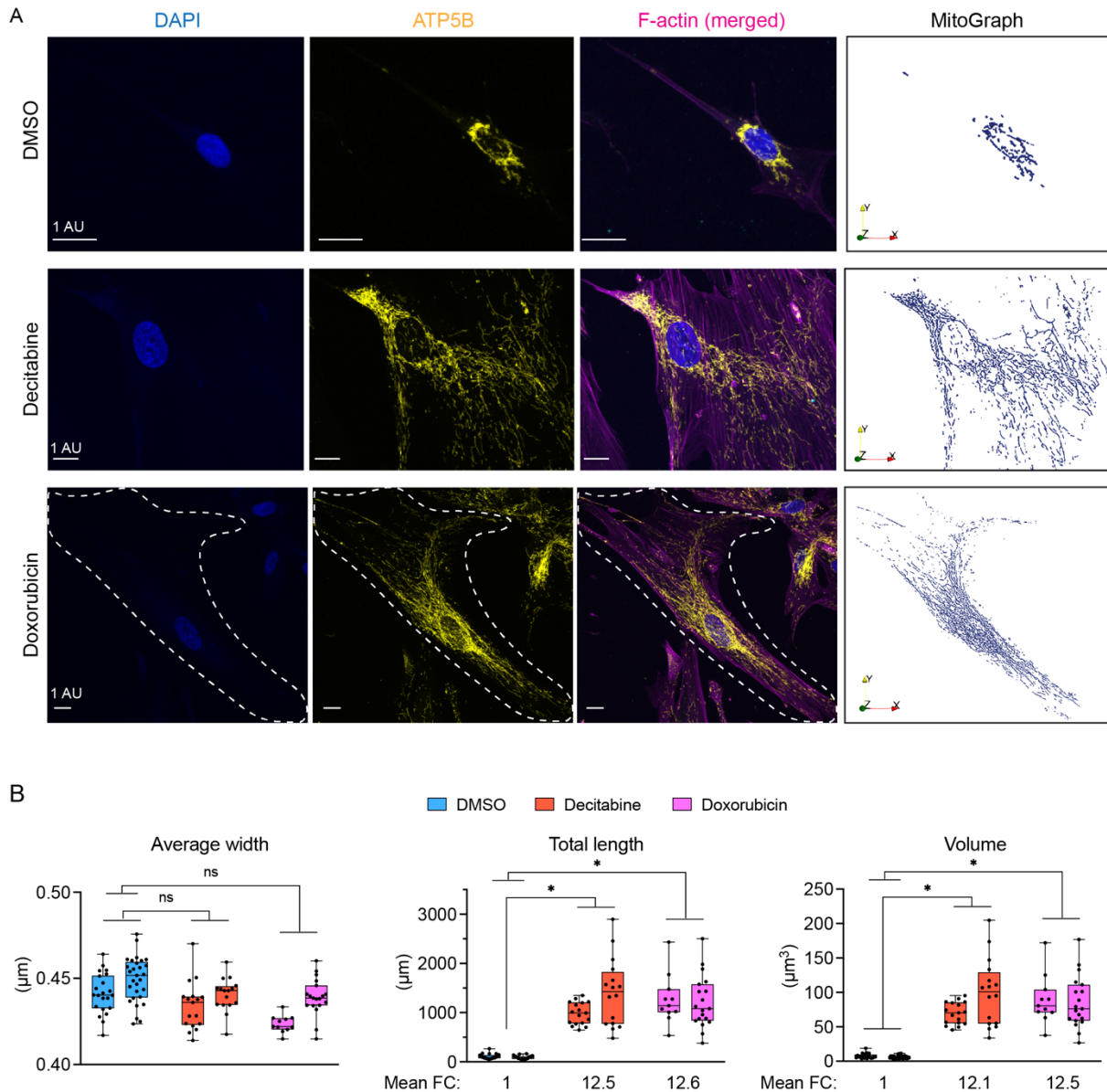


Figure 5.1.2 Quantification of mitochondrial volume per cell upon TIS establishment

(A) Representative images of max projection combined with z-stack confocal images and their 3-dimensional rendering images of mitochondria per cell by MitoGraph 2.0. AU: arbitrary unit.

(B) Quantified parameters of mitochondrial abundance. Whisker of the box stands for the mean and each dot represents a measured value from each single cell. Counted were between 11 and 29 cells per replicate in each condition. Mean fold changes are denoted. Nested One-way ANOVA, Dunnett's correction, n=2.

5.1.3 Profound increase of hypoactive mitochondria in TIS reconciles discrepancies in mitochondrial states

Based on the reasoning that different normalization unit used in the literature is attributed to the mitochondrial contradictions in CS, diverse mitochondrial features were analyzed by taking the increased mitochondrial volume per TIS fibroblast into account to resolve the contradictions. In the subsequent analysis, mitochondrial volume was used as a proxy for mitochondrial abundance and hence the unit volume stands for the mitochondrial entity—mitochondrion. As a result, many aspects of mitochondria were changed in TIS fibroblasts in accordance with the literature when considered per cell, however, it was no longer valid when considered per mitochondrion. For example, mtDNA copy number, one of the most frequently used readouts of mitochondrial abundance, was increased ~6-fold per TIS fibroblast but reduced to half per TIS mitochondrion (Figure 5.1.3 A). Similarly, mitochondrial superoxide levels measured by mitoSOX and membrane potential by TMRM showed the same pattern (Figure 5.1.3 B-E). These data show that the individual mitochondrion is indeed in a hypoactive state. Based on these data, I reasoned that repeatedly reported enhancement of mitochondrial respiration in CS would also fall into such a case. To test it, oxygen consumption rate (OCR) was measured with different classes of OXPHOS modulators in a real-time manner by Seahorse equipment. As reasoned, the basal mitochondrial respiration was overall higher per TIS fibroblast but strikingly lower per TIS mitochondrion (Figure 5.1.3 G, H). These data suggest that the enhancement of mitochondrial respiration in CS is due to the massively increased mitochondria which have far lower OCR. In light of this, other parameters of mitochondrial bioenergetics were analyzed from the real-time OCR measurement to check whether such parameters would support the observed bioenergetically dysfunctional state of mitochondria (Figure 5.1.3 G, H). Consistent with the idea, the proton leak was increased which is indicative of electron transport chain (ETC) dysfunction with higher electron slippage. In addition, decreased spare respiratory capacity caused by either a loss of ETC integrity or decreased substrate availability is another sign of dysfunction. Along with mitochondrial respiration, the increased non-mitochondrial oxygen consumption indicates the increased level of ROS produced from non-mitochondrial sources (e.g., cytosol and peroxisome), which explains the augmentation of cellular ROS levels reported multiple times in CS.

In summary, these data unequivocally demonstrate that the profound increase of bioenergetically dysfunctional mitochondria in a TIS fibroblast gives rise to the enhanced mitochondrial functions as a sum and resolves the contradictory reports regarding the mitochondrial functions in CS.

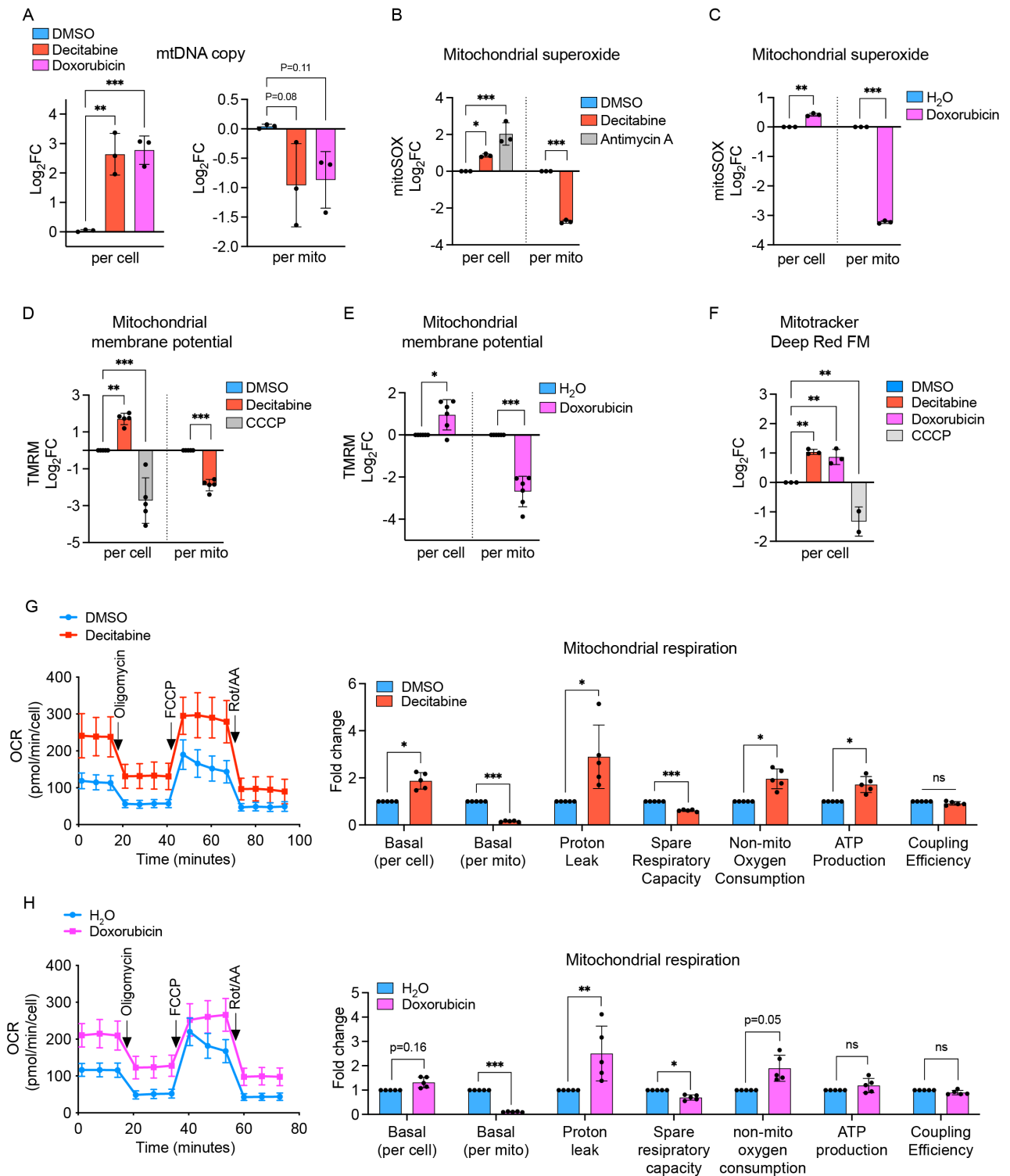


Figure 5.1.3 Profound increase of dysfunctional mitochondria in TIS resolves contradictions in mitochondrial states

(A-G) All the measured parameters were normalized by cell number, and then scaled by mean FC of mitochondrial volume.

(A) MT-ND1 and ACTB were measured as readouts of mtDNA and genomic DNA. One-way ANOVA, Dunnett's correction. n=3

(B-F) Mean fluorescence intensities of mitochondrial probes were measured by flow cytometry. Antimycin A and CCCP were used as positive controls. One-way ANOVA, Dunnett's correction for 3 groups and Welch t-test for 2 groups. (B,C,F) n=3, (D) n=5, (E) n=6

(G,H) Left: measurement of the real-time oxygen consumption rate (OCR) with different OXPHOS modulators. Right: fold changes of several parameters calculated from the left graphs were transformed by log2 and subject to statistical analysis. Welch t-test, Bonferroni-Dunn correction. n=5

5.1.4 Time-resolved analysis of mitochondrial proteome during the development of TIS

TIS is temporally dynamic ranging from an initial trigger to a full-fledged state, which normally takes around 5-7 days *in vitro*. In regard to the dynamic and in order to gain molecular insights to decipher the role of dysfunctional mitochondria in TIS, the proteome of TIS fibroblasts evoked by Decitabine were analyzed in a time-resolved manner encompassing from the initiation to the establishment by tandem mass tag labeling mass-spectrometry (TMT-MS) (Figure 5.1.4 A). Leveraging the power of TMT-MS to minimize missing values across samples, only proteins identified in all 32 samples were considered for the subsequent analysis to yield robust proteomic data. As a result, 6482 proteins were analyzed (Figure 5.1.4 B). Principal component analysis (PCA) showed that the biological replicates were well clustered together while decitabine segregated the proteome away from DMSO, indicating the emergence of systemic difference in the cellular proteome during the development of TIS (Figure 5.1.4 C). In detail, the fully quantified 6482 proteins covered overall 60% of major cellular organellar proteome based on the reference databases, especially 692 mitochondrial proteins enlisted in human MitoCarta 3.0 (Figure 5.1.4 D, refer to Appendix 1 for the organelle-specific proteome change). It could also be confirmed the successful induction of CS by several key protein markers such as reduction of LMNB1, HMGBs, and the decitabine target DNMT1 as well as an increase of CDKN1A and several SASP genes (Figure 5.1.4 E).

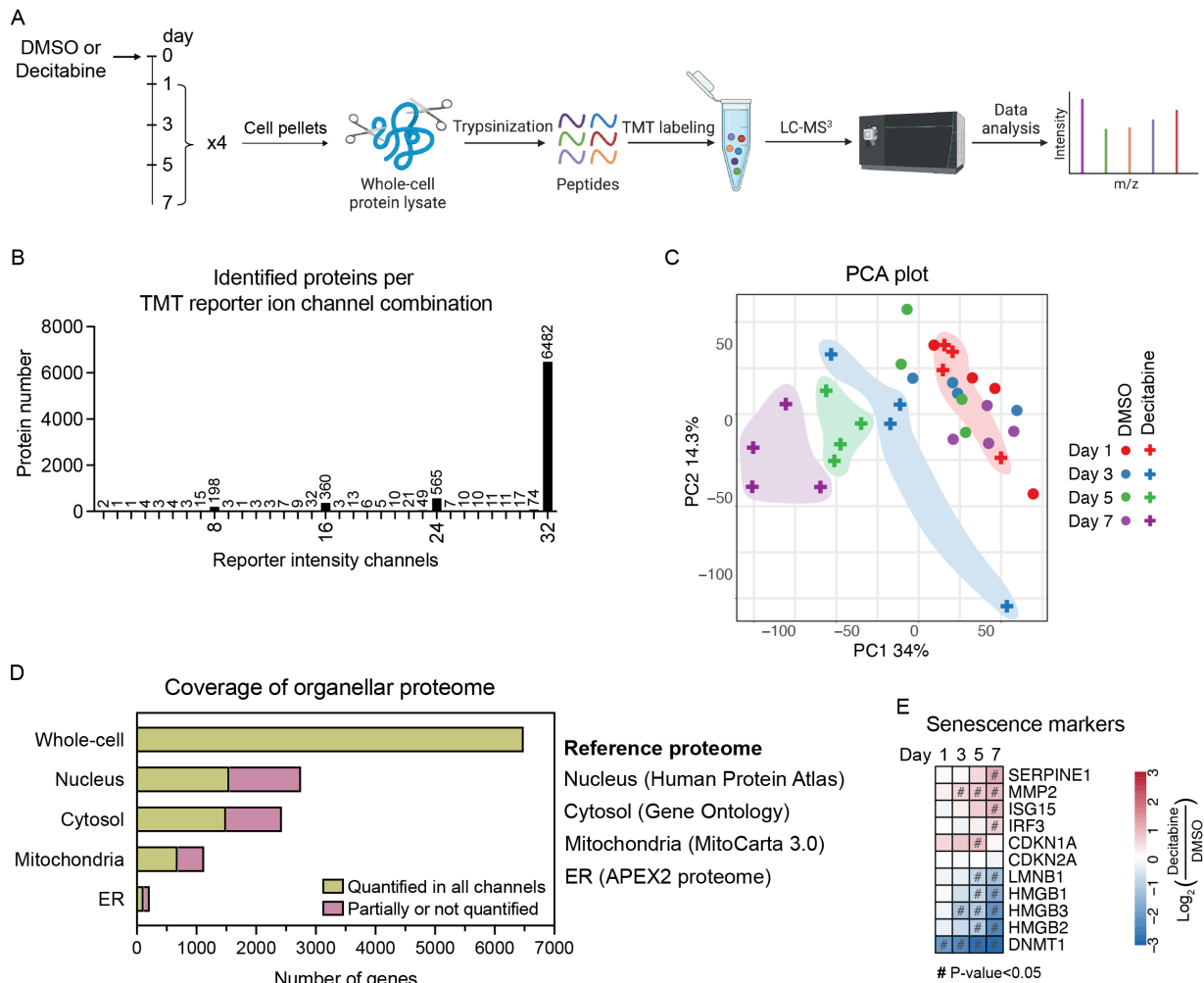
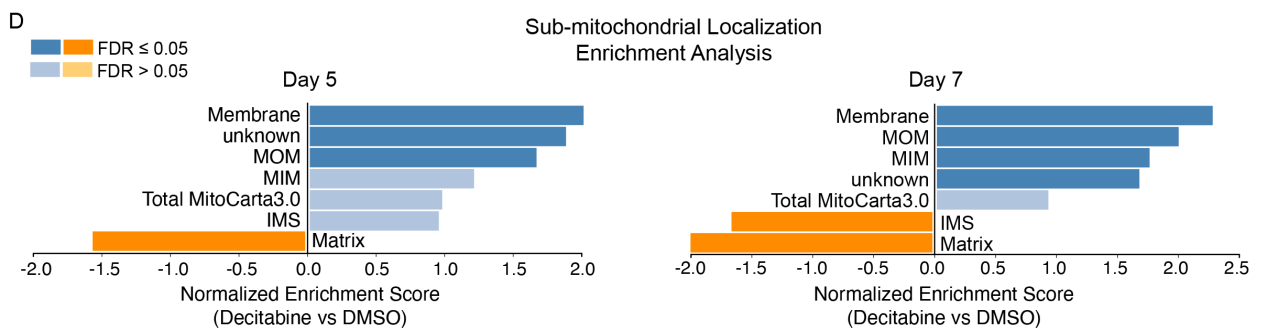
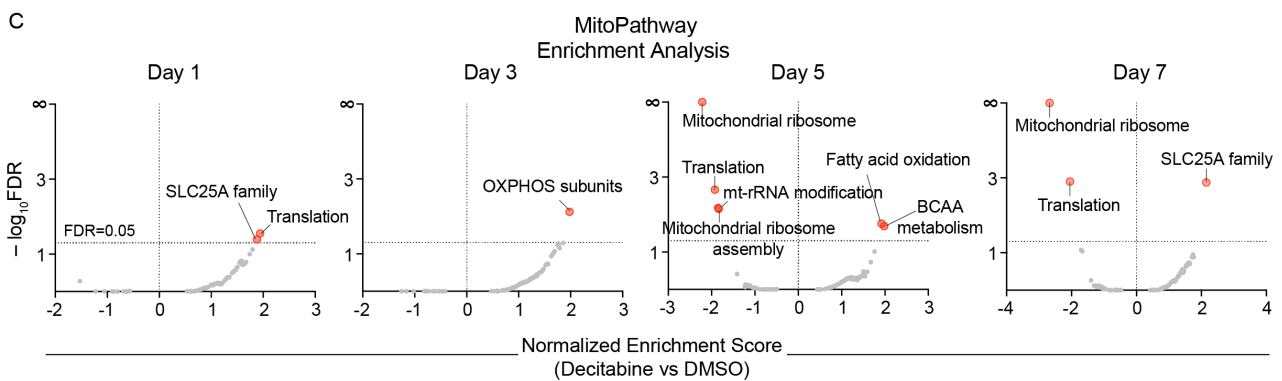
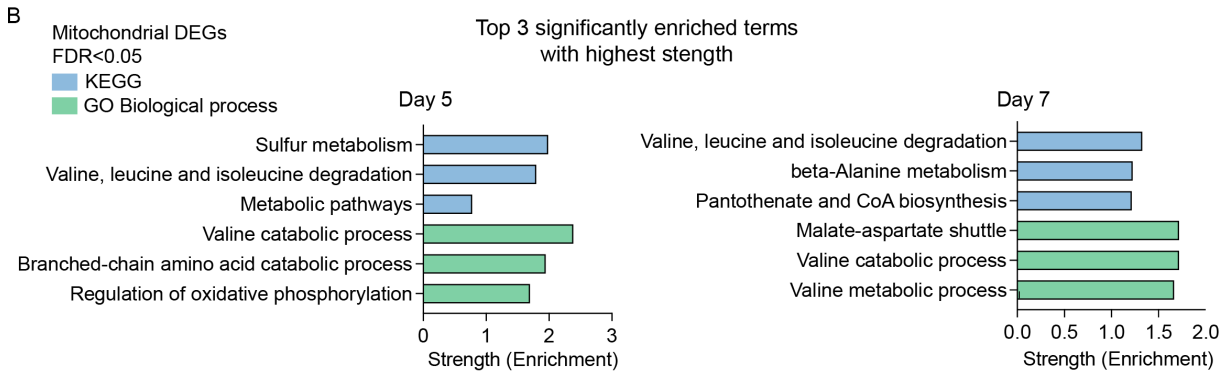
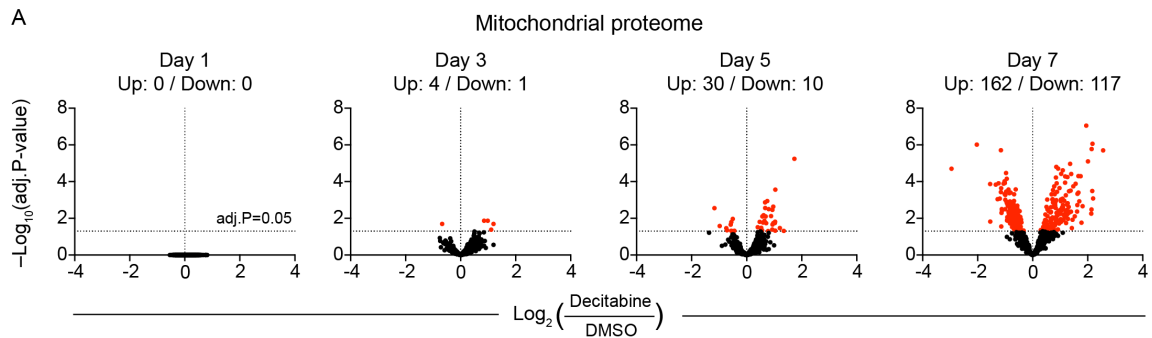


Figure 5.1.4 Time-resolved analyses of cellular proteome during development of TIS

- (A) Schematic depiction of workflow. Data-dependent acquisition of proteomics by TMT-10 plex labeling.
 (B) The number of proteins detected per TMT reporter ion channel. 4 replicates x 2 treatments x 4 time points = 32 samples.
 (C) Principal component analysis (PCA) plot of 32 samples. Decitabine-treated samples are grouped with highlights.
 (D) Coverage of organellar proteome based on the reference database as shown.
 (E) Proteomic validation of successful establishment of cellular senescence. # denotes adjusted P-value < 0.05

Next, analyzed were mitochondrial differentially expressed genes (DEGs) at each time point. The mitochondrial proteome started to differentiate as early as day 3 and developed a significant number of changes on day 7 (Figure 5.1.5 A). Over-representation analysis by two different databases GO and KEGG consistently revealed that several metabolic pathways mainly branched-chain amino acid (BCAA) metabolism were the most significantly changed amongst all the mitochondrial terms throughout the development of TIS (Figure 5.1.5 B). As an orthogonal approach, the proteomics data were also analyzed by the gene-set enrichment analysis (GSEA) without filtration of DEGs by the arbitrary cutoff (i.e., $p=0.05$) to increase the signal to noise ratio. GSEA was performed on two different features of mitochondria: signaling pathways and sub-mitochondrial localization, both being crucial to gaining deeper insights into mitochondrial biology. MitoPathways curated by MitoCarta 3.0 includes 134 pathways exclusive to mitochondria and thereby enables a tailored analysis without involving non-mitochondrial genes, unlike that of GO and KEGG. Interestingly, the analysis revealed that the pathways involved in the expression of mtDNA-encoded genes are significantly reduced on day 5 and 7 whereas pathways generally related to metabolism are increased (Figure 5.1.5 C). Furthermore, the GSEA of sub-mitochondrial localization uncovered proteins at both inner and outer membrane (MIM and MOM) were overall increased while decreased were those in the matrix and intermembrane space (IMS) (Figure 5.1.5 D). These two analyses are coherent in part in that the increased SLC25A family is comprised of proteins at MIM whereas mitochondrial ribosome and translation proteins are localized in the matrix. Of note, the overall enrichment of membrane proteins is unlikely due to the increased protein import not only because the enrichment at day 5 preceded the observed change of the import machinery on day 7, but also because the small TIM proteins (TIMM8B, TIMM9, TIMM10, TIMM13) responsible for the chaperone-mediated import of many hydrophobic membrane proteins were generally reduced at day 7 (Figure 5.1.5 D, Appendix 2; Import & Sorting).



(continued)

The analyses so far have delineated the mitochondrial proteome at each time point considered as an individual entity. However, these snapshots might not necessarily reflect the continuity of the enriched pathway throughout the given time points. As a complement, therefore, mitochondrial DEGs of at least one-time point were selected and grouped according to their temporal dynamic patterns,

which gave rise to 4 different groups (Figure 5.1.5 E; left boxes, refer to Appendix 3 for the detailed list of DEGs in each group). Groups 1 and 2 are proteins that significantly changed as early as day 3 and groups 3 and 4 are the ones that changed on day 7. Of note, only 1.5 % of the analyzed DEGs did not fall into any of the 4 groups, showing that few genes fluctuated during the development of TIS while the majority either increased or decreased without oscillation (Figure 5.1.5 E, F). Over-representation analysis of groups 1 and 2 suggested upregulation of BCAA degradation and downregulation of one-carbon folate (herein, 1C-folate) metabolism whereas that of groups 3 and 4 indicated upregulation of fatty acid metabolism and calcium import into the mitochondria as well as downregulation of mitochondrial translation. These results were comparable to the ones performed previously without temporal grouping (Figure 5.1.5 B, C), corroborating the fact that there were few genes that fluctuated. Interestingly, the analysis did not show any general decrease of OXPHOS subunits or assembly factors, contrary to the expectation based on the mitochondrial dysfunctions shown previously (Figure 5.1.3). This indicates that the dysfunctions may be explained by the functional integrity of ETC, rather than its protein levels. Another salient fact is that the enriched terms of early changes are mainly related to mitochondrial metabolic pathways rather than any other aspects of mitochondria (e.g., dynamics, protein import, OXPHOS), arguing the major role of mitochondria would be about metabolic rewiring to support the early stage of TIS. The detailed list of the entire mitochondrial proteins analyzed is in Appendix 2.

In conclusion, the time-resolved proteomic data suggest that mitochondria are reprogrammed in TIS to enhance the metabolism of BCAA and fatty acid while reducing the 1C-folate metabolism, followed by a systemic decrease of translational machinery of mtDNA-encoded genes.

E

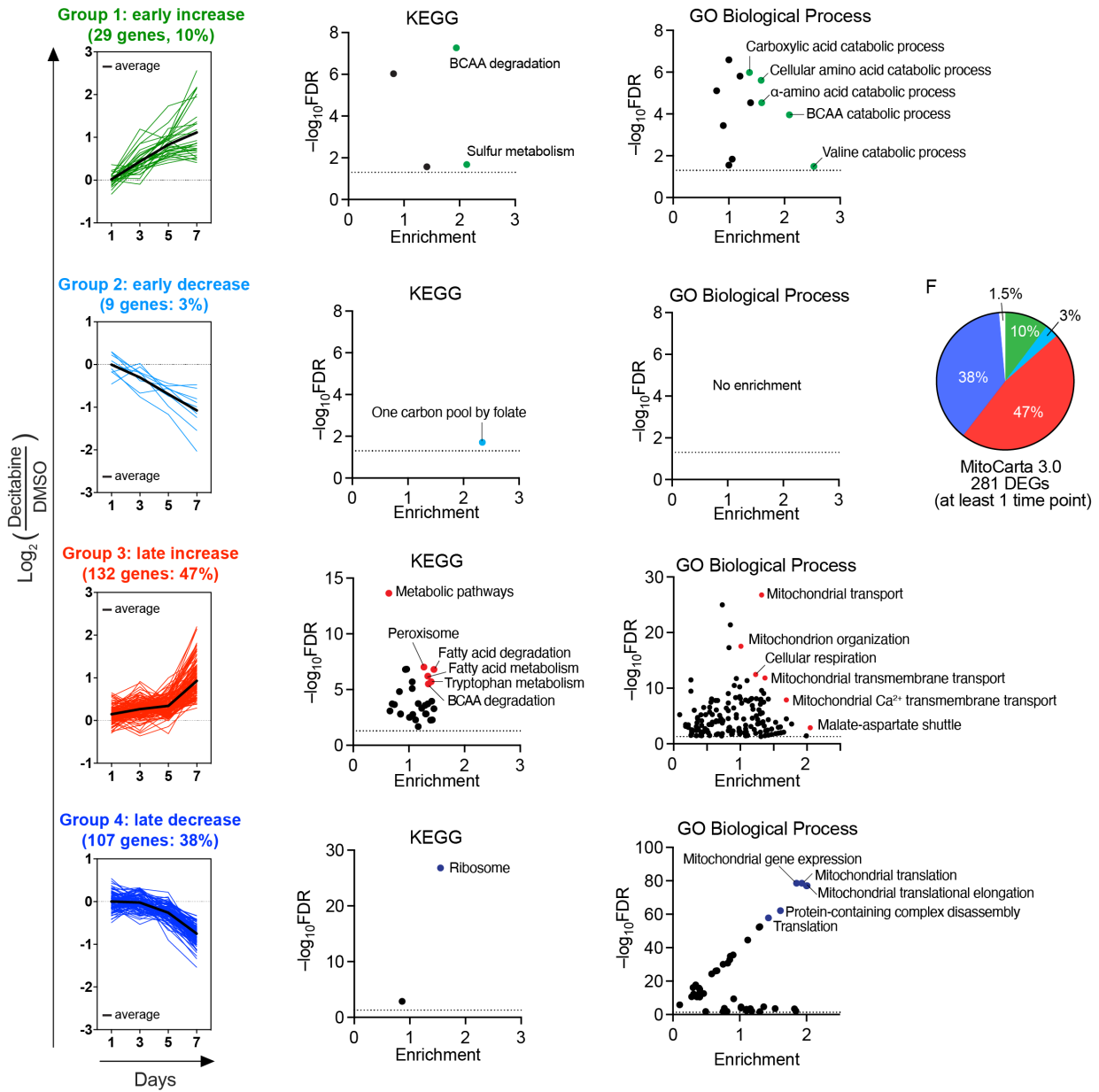


Figure 5.1.5 Detailed analysis of mitochondrial proteome during development of TIS

- (A) Volcano plots with the number of mitochondrial DEGs at each time point based on human Mitocarta 3.0.
- (B) Over-representation analysis of mitochondrial DEGs. Top 3 enriched terms are presented. FDR: false discovery rate
- (C,D) GSEA of MitoPathway and sub-mitochondrial localization. Total human Mitocarta 3.0 genes were used as background.
- (D) MOM: mitochondrial outer membrane, MIM: mitochondrial inner membrane, IMS: intermembrane space.
- (E,F) 4 groups of mitochondrial DEGs according to the temporal dynamics.
- (E) Over-representation analysis of each group. A few pathways are highlighted.
- (F) Percentage of DEGs comprising each group.

5.1.5 Positive association of mitochondrial translation with 1C-folate metabolism in TIS fibroblasts

To find out the regulatory role of mitochondria in TIS, I focused on the pathways enriched in groups 1 and 2, assuming that the early responders are likely to be causal factors in the subsequent changes observed in the group 3 and 4 (Figure 5.1.5 E) and thereby possibly serve as drivers of TIS. In this vein, group 2 was vet in depth, to begin with. Although the over-representation analysis was performed exclusively on mitochondrial DEGs, the enzymes involved in the cytosolic 1C-folate metabolic pathways were also found to be acutely decreased upon induction of TIS with similar temporal dynamics to that of mitochondria (Figure 5.1.6 A). The major role of the pathway is to provide intermediate molecules for synthesis of purine and deoxythymidine nucleotides as well as mitochondrial N-formylmethionine (herein, f-Met) which serves as an initial amino acid for the protein synthesis in mitochondria and hence crucial for the translational activity. To test whether the observed reduction of 1C-folate metabolism results in a decreased amount of its product, performed was semi-targeted metabolomics focusing on polar metabolites including nucleotides and amino acids (a full list is in Appendix 4). PCA showed the metabolome of TIS fibroblasts is distinct from that of proliferating cells (Figure 5.1.6 B). Importantly, the metabolomics revealed a significant depletion of purines (AMP, GMP) and deoxythymidines (dTTP, dTMP was even under the detection limit exclusively in both TIS fibroblasts) in line with the proteomic analysis of 1C-folate metabolism (Figure 5.1.6 C). Interestingly, only the monophosphates were decreased unlike the triphosphates. Probably it is because the monophosphates are the direct product of *de novo* synthesis which would reflect the activity of the pathway more closely. Another indicator of the activity of the pathway is the serine to glycine ratio which is altered by cytosolic SHMT1 and mitochondrial SHMT2 (Figure 5.1.6 A). Of note, the ratio is significantly increased in both TIS fibroblasts which mirrors the reduced level of SHMT2 (Figure 5.1.6 D). Lastly, it was investigated for the link between reduced f-Met level and mitochondrial translational activity. Consistent with the known role of f-Met, the mitochondrial translation was reduced in both TIS fibroblasts measured by autoradiograph after labeling *de novo* mtDNA-encoded peptides with ³⁵S methionine and cysteine. Although the statistical analysis did not yield significance due to one outlier sample of decitabine, it was obtained after excluding the outlier (Figure 5.1.6 E). However, the reduced translation did not instantly cause the reduction of steady-state level checked from the proteomics data (Appendix 2; OXPHOS; MT-CO2, MT-ATP8) arguably because many OXPHOS subunits are known to be long-lived proteins.

In summary, the early downregulation of 1C-folate metabolism coordinated between cytosol and mitochondria is associated with the reduced level of nucleotides and mitochondrial translation in TIS fibroblasts.

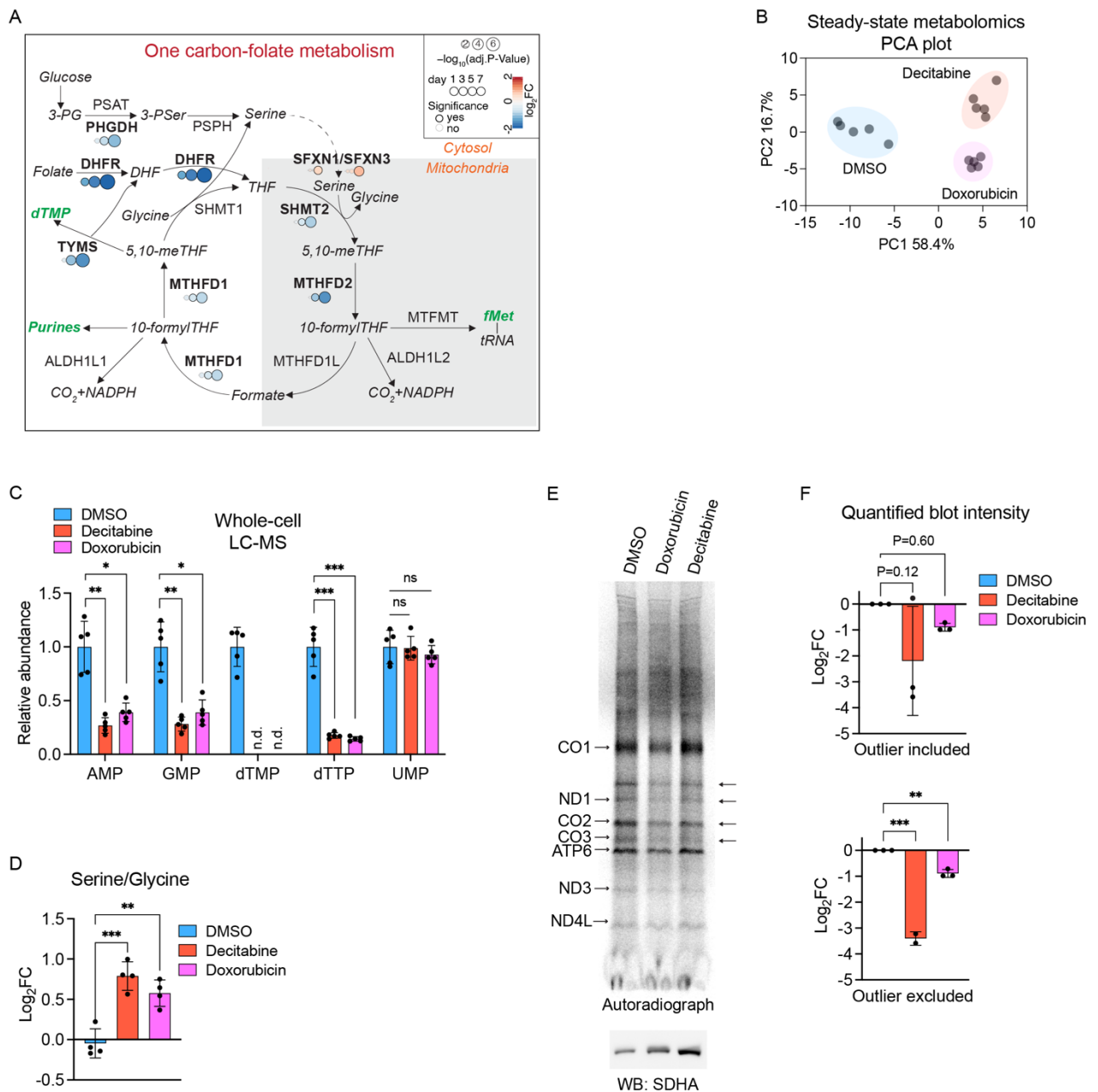


Figure 5.1.6 Reduced mitochondrial translation in TIS is associated with early downregulation of 1C-folate metabolism

(A) Metabolic pathway of 1C-folate metabolism. Enzyme levels at each step are denoted from the time-resolved proteomic data.

(B) PCA plot of steady-state metabolomics data of TIS cells. 79 metabolites were quantified and normalized by total ion counts. $n=5$

(C) Level of nucleotides from (B). Statistical analysis is done on 79 metabolites with Welch t-test, Bonferroni-Dunn correction. $n=5$

(D) Serine to Glycine ratio from (B). One outlier replicate was omitted. One-way ANOVA, Dunnett correction. $n=4$

(E) A representative autoradiograph image of mitochondrial translation. SDHA was used as a reference for equal loading. Arrows indicate pronounced decreases in both TIS mitochondria. $n=3$

(F) Quantified values of (E) with or without an outlier. The intensity of each entire lane was divided by that of corresponding SDHA band. One-way ANOVA, Dunnett correction. $n=3$

5.1.6 Increased nitrogen supply by BCAAs to NEAAs in TIS fibroblasts

The proteomic analysis revealed that BCAA catabolic process was the most significantly enriched term in group 1 comprised of early increased genes upon the induction of TIS (Figure 5.1.5 E). A closer look into the catabolic pathway of BCAA in mitochondria recapitulated that many enzymes involved in the degradation were all upregulated throughout the measured time points except for a slight reduction of BCKDHA (Figure 5.1.7 A). The degradation of BCAA takes place in mitochondria except for the first catalytic step which is compartmentalized by cytosolic BCAT1 and mitochondrial BCAT2. To validate the result from the proteomics with a spatial resolution, mitochondria and cytosolic fractions from the fibroblasts were extracted and the level of each enzyme was measured by western blot. Indeed, BCAT2 but not BCAT1 was increased comparable to the fold-change from the proteomic data in both TIS fibroblasts, although it did not yield a statistical significance due to the high variance (Figure 5.1.7 B-D). Thus, the fact that the increased amount of BCAT2 proteins in the TIS fibroblasts was found in the mitochondria excluded a possible scenario of the mislocalization of BCAT2 due to the low mitochondrial membrane potential (Figure 5.1.3 D). The first catalytic step performed by BCAT2 is trans-amination that the nitrogen of the amino group is transferred to α -ketoglutarate to yield glutamate. The nitrogen then could subsequently be utilized to synthesize non-essential amino acids (NEAAs) and uridines (Figure 5.1.7 E). As inferred from the proteomic data, the metabolic tracing experiment using nitrogen mass isotopologues of valine and leucine demonstrated the increased flux of BCAA amino group into glutamate (Figure 5.1.7 F). The subsequent downstream fate of the amino group traced from the same experiment uncovered that the nitrogen had been fed into serine, alanine, aspartate, and proline. Considering the effect size of the labelled fraction, aspartate and proline appeared to be the major receivers of BCAA nitrogen in TIS fibroblasts. Besides, I also obtained preliminary data of increased flux of the BCAA carbons into acyl-CoAs without reaching the TCA cycle and decreased neutral lipids in BCAT2 knockdown TIS fibroblasts (data not shown; ongoing work), which speaks against its possible role in anaplerotic reactions to replenish the pools of TCA cycle metabolites. This is also consistent with the observation of a general decrease of TCA cycle metabolites in TIS fibroblasts (Appendix 4), which warrants the future study about the potential role of those acyl-CoAs in lipogenesis in TIS fibroblasts.

All in all, the increased catabolism of BCAAs in the mitochondria driven by a systemic rewiring of the proteome supplies nitrogen for the synthesis of NEAAs in TIS fibroblasts.

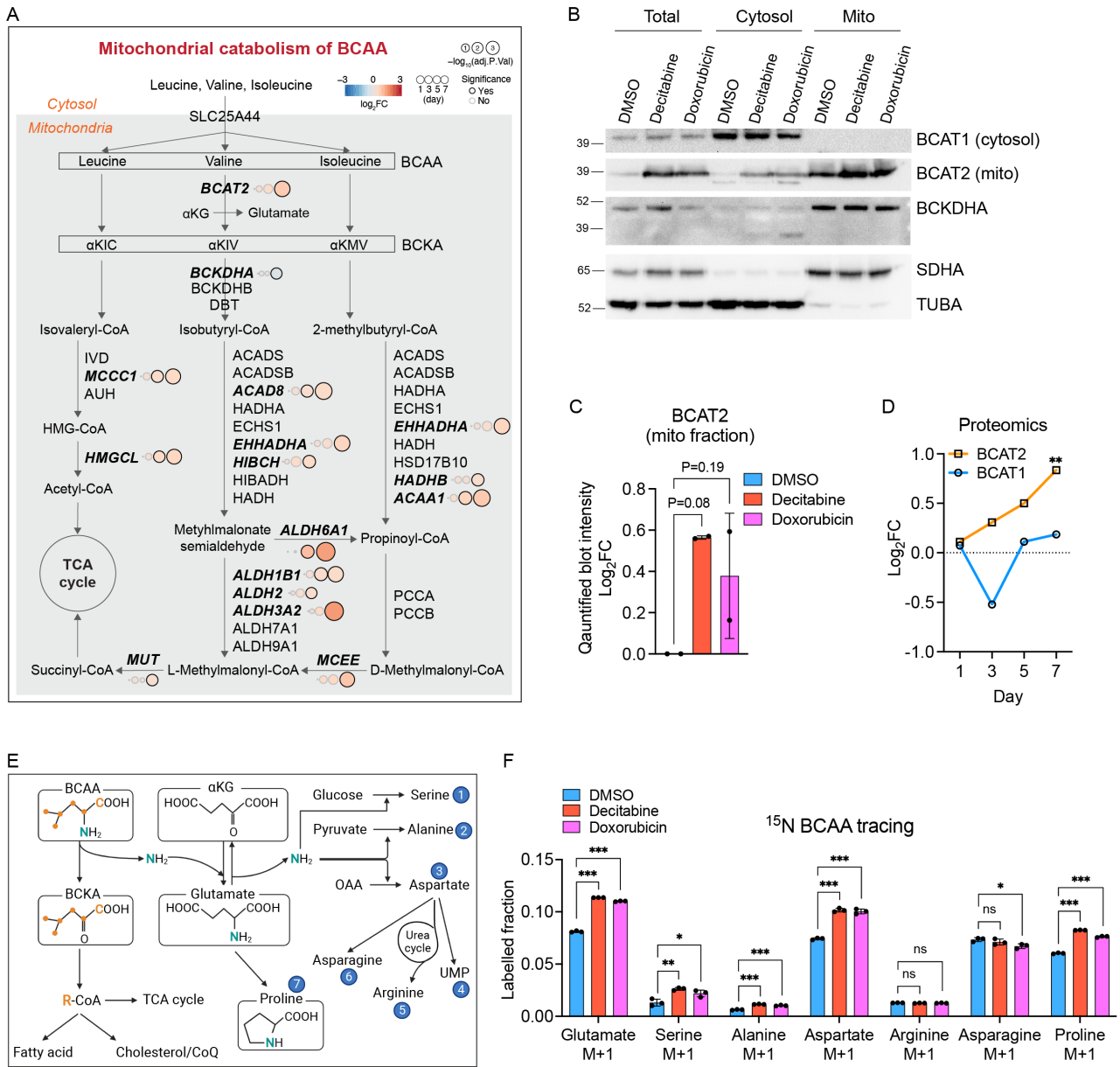


Figure 5.1.7 Enhanced mitochondrial catabolism of BCAA provides nitrogen for NEAA synthesis in TIS fibroblasts

(A) Metabolic pathway of BCAA degradation in mitochondria. The level of enzymes at each step is noted from the time-resolved proteomic data. BCKA: branched-chain α -keto acid. Bold italicized: mitochondrial DEGs.

(B) A representative western blot of BCAT2 from fractions enriched with cytosol and mitochondria. n=2

(C) Quantified blot intensity from mito fraction in (B). The intensity of BCAT2 blot was normalized by that of corresponding BCKDHA blot. One-way ANOVA, Dunnett correction. n=2

(D) The protein levels of BCAT1 and BCAT2 from the proteomics data. Statistical significance was derived from the proteomics data.

(E) Diagram of the metabolic fate of BCAA carbon and nitrogen to the downstream metabolites. Yellow: carbon, green: nitrogen. The numbers denote the possible fate of nitrogen. Note that the pathways depicted are not specific to mitochondria but include cytosol.

α kG: α -ketoglutarate, CoQ: coenzyme Q, OAA: oxaloacetic acid

(F) Valine and Leucine labelled with ¹⁵N were fed together as 1:1 for 24 hours. Each metabolite was subject to statistical analysis separately. One-way ANOVA, Dunnett correction. n=3

5.2 Reverse genetics: OCIAD2 in the cellular senescence

5.2.1 Identification of OCIAD2 as a pan-marker of CS

Based on the mitochondrial proteome characterized in the TIS fibroblasts, it was sought to identify a novel mitochondrial gene that would regulate the mitochondrial function and thereby the biology of the TIS in parallel to the genes related to BCAA metabolism and 1C-folate metabolism (Result 5.1). In this vein, there was one salient gene earliest changed with the highest fold change and statistical significance upon induction of the TIS: OCIAD2 (Appendix 1; mitochondria). It garnered my attention that OCIAD2 was a poorly characterized gene and no study was available in the context of cellular senescence. I first investigated whether the increase of OCIAD2 is related to the cell-cycle arrest, as it could also be the case of quiescence and not necessarily senescence. The cellular quiescence was evoked by two different means, contact inhibition and serum deprivation. As a result, the quiescence was distinguished from the senescence by the LMNB1 reduction, a senescence-specific marker, from the western blot analysis (Figure 5.2.1 A). It also showed the exclusive increase of OCIAD2 in the TIS as well as the similar temporal dynamics of OCIAD2 with that of proteomics result, indicating OCIAD2 is increased in the senescence rather than the quiescence. To know whether this is a cell-line specific outcome, MRC5 human lung fibroblasts were also induced to be TIS by bleomycin or doxorubicin treatment for 7 days. Consistent with IMR90 cells, OCIAD2 mRNA level was also significantly increased in TIS MRC5. Of note, OCIAD1—the homologous gene of OCIAD2—was increased little or no in MRC5 and IMR90, suggesting the independent regulation of these homologous genes in CS (Appendix 1; proteomics, Figure 5.2.1 B, C, F). The transcriptional regulation of OCIAD2 in TIS was also shown to be the case in IMR90 cells in a time-dependent manner (Figure 5.2.1 C). Thus, OCIAD2 is transcriptionally upregulated in the TIS fibroblasts evoked by multiple means. I then checked whether the increase of OCIAD2 is general in the CS or limited to the TIS. The preliminary data indeed showed that OCIAD2 was also increased in the replicative senescent (RS) fibroblasts induced by a serial passaging (Figure 5.2.1 D, E). Moreover, OCIAD2 was reported to be upregulated transcriptionally in senescent fibroblasts induced by the oncogenic Ras (Figure 5.2.1 F).

All in all, these observations altogether demonstrated the OCIAD2 is a pan-marker for senescent fibroblasts and a potential candidate as a mitochondrial regulator of CS.

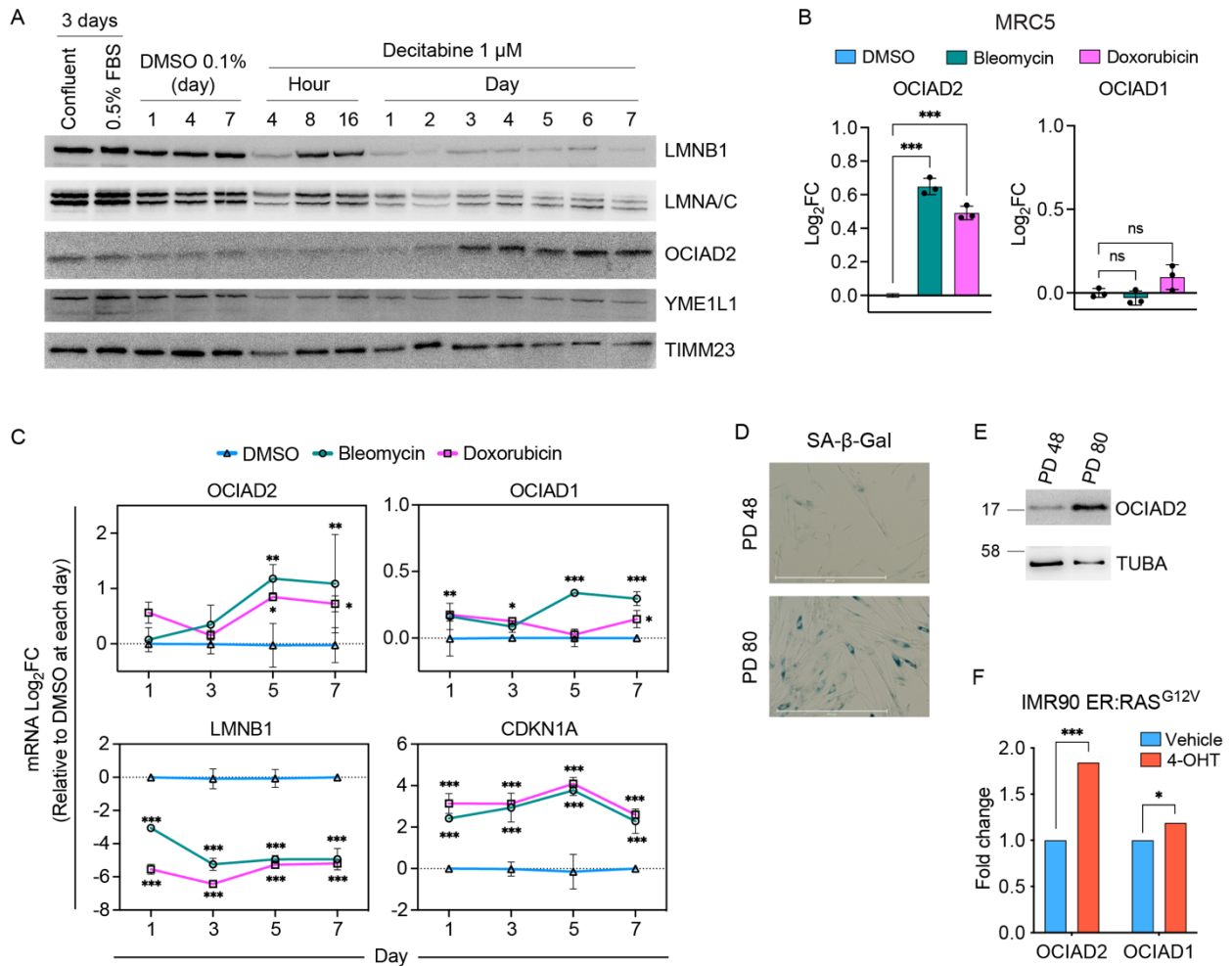


Figure 5.2.1 Identification of OCIAD2 as a pan-CS marker

(A) Western blot analysis of OCIAD2 level in a series of time points upon induction of TIS. Quiescence was included by two different means: serum starvation (0.5% FBS) or contact inhibition (confluent) for 3 days. LMNA/C and TIMM23 was used as a loading control. n=1

(B) RT-qPCR analysis of OCIAD1 and OCIAD2 in MRC5 human lung fibroblast. One-way ANOVA, Dunnett correction. n=3

(C) RT-qPCR analysis of OCIAD2 and others in a time-resolved manner. Two-way ANOVA, Dunnett correction. n=3

(D) Cells were passaged routinely to reach late passage. PD: population doublings. Scale bar: 500 μ m. n=1

(E) Western blot of cells from (D). TUBA was used as a loading control. n=1

(F) mRNA levels of OCIAD2 and OCIAD1 in oncogene-induced senescence IMR90, presented by processing the publicly available RNA-seq data (GSE41318). Fold change and statistical significance was derived from the original publication. n=3

5.2.2 OCIAD2 is localized at inner membrane of mitochondria

Though the location of OCIAD2 is shown to be mitochondria by the MitoCarta 3.0, it was confounded by incongruent reports to be in the mitochondria, endosome and mitochondria-associated membrane (MAM) as well as the fact that it lacks any signal peptide. To resolve the issue, its localization was examined from cellular fractions with different organelles including mitochondria of HEK293 cells. HEK293 cells were used due to its high yield of mitochondria and the significant expression level of OCIAD2. In fact, OCIAD2 was localized specifically in the mitochondria as

demonstrated by its exclusive detection in the pure mitochondrial fraction devoid of the ER, endosome, cytosol, and nucleus (Figure 5.2.2 A). Next, another discrepancy was addressed whether it is localized at the inner membrane or outer membrane of mitochondria. OCIAD2 was predicted to have two alpha-helical transmembrane domains (Figure 5.2.2 B) with a positive net charge in the flanking region of those two domains at mitochondrial matrix pH 8. Based on this prediction, the exact topology of OCIAD2 in the mitochondria was tested by proteinase K assay. As a result, the assay demonstrated that OCIAD2 is a mitochondrial inner membrane (MIM) protein (Figure 5.2.2 C, D). According to the positive inside rule which applies to mitochondrial membrane proteins, the conclusive topology was presented as both N and C-termini residing in the intermembrane space (IMS) whereas the flanking region in the matrix (Figure 5.2.2 E).

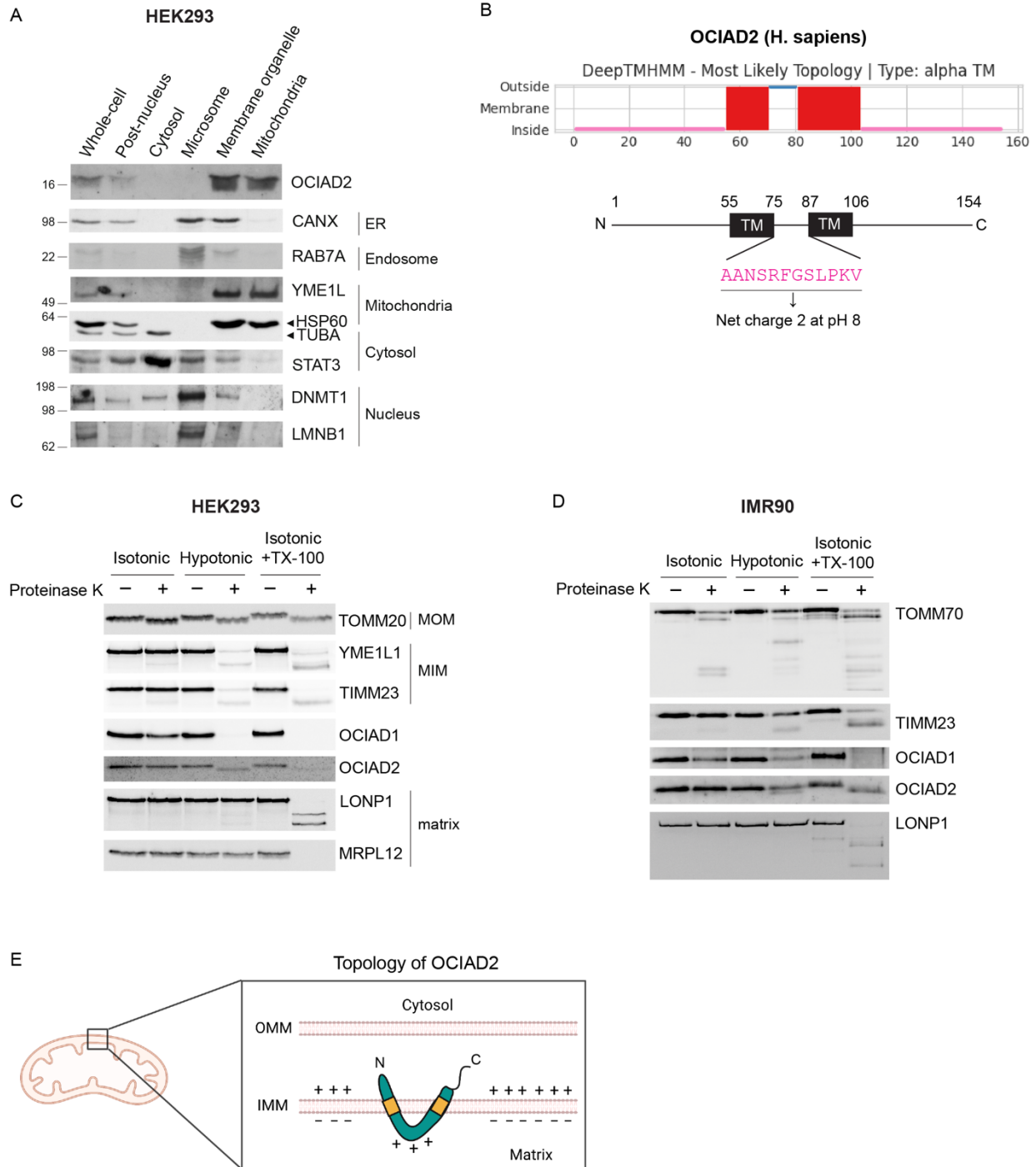


Figure 5.2.2 OCIAD2 is localized at inner membrane of mitochondria

(A) A representative western blot of several fractions from HEK293 cells. n=2

(B) Analysis of amino acid sequence of OCIAD2. Two α -helical transmembrane domains were predicted by deep learning algorithm.

(C, D) A representative western blot of OCIAD2 topology assay. MOM: mitochondrial outer membrane, MIM: mitochondrial inner membrane. (C) HEK293, n=3. (D) IMR90, n=2

(E) Topology of OCIAD2 based on the combined data.

5.2.3 OCIAD2 is neither sufficient nor required to establish TIS

The fact that OCIAD2 is generally increased in CS prompted me to investigate whether it is sufficient to induce the CS. To this end, OCIAD2 with epitope tags (Myc and FLAG) was overexpressed in IMR90 (Figure 5.2.3 A). The overexpressed OCIAD2^{MycFLAG} protein was successfully localized in the mitochondria (Figure 5.2.3 B). Around up to 40 days post generation, there was no sign of spontaneous senescence in the overexpressing cells as evidenced by normal proliferation rate (Figure 5.2.3 C) and a lack of SA- β -Gal signal (data not shown). Thus, the increased OCIAD2 is not a cause of CS. Next, it was analyzed whether OCIAD2 is necessary for the induction of the TIS. A stable knockdown of OCIAD2 was achieved via lentiviral transduction of 4 different shRNA oligos targeting OCIAD2 (Figure 5.2.3 D) and there was no defect in proliferation at any given time of the culture (Figure 5.2.3 E). The OCIAD2 knockdown cells were then induced to senesce by decitabine and doxorubicin to address its necessity in the TIS. As a result, there was no difference to reach the established state of the TIS, as shown by SA- β -Gal positivity (Figure 5.2.3 F, G).

These data demonstrate that OCIAD2 is neither sufficient nor required to establish the TIS.

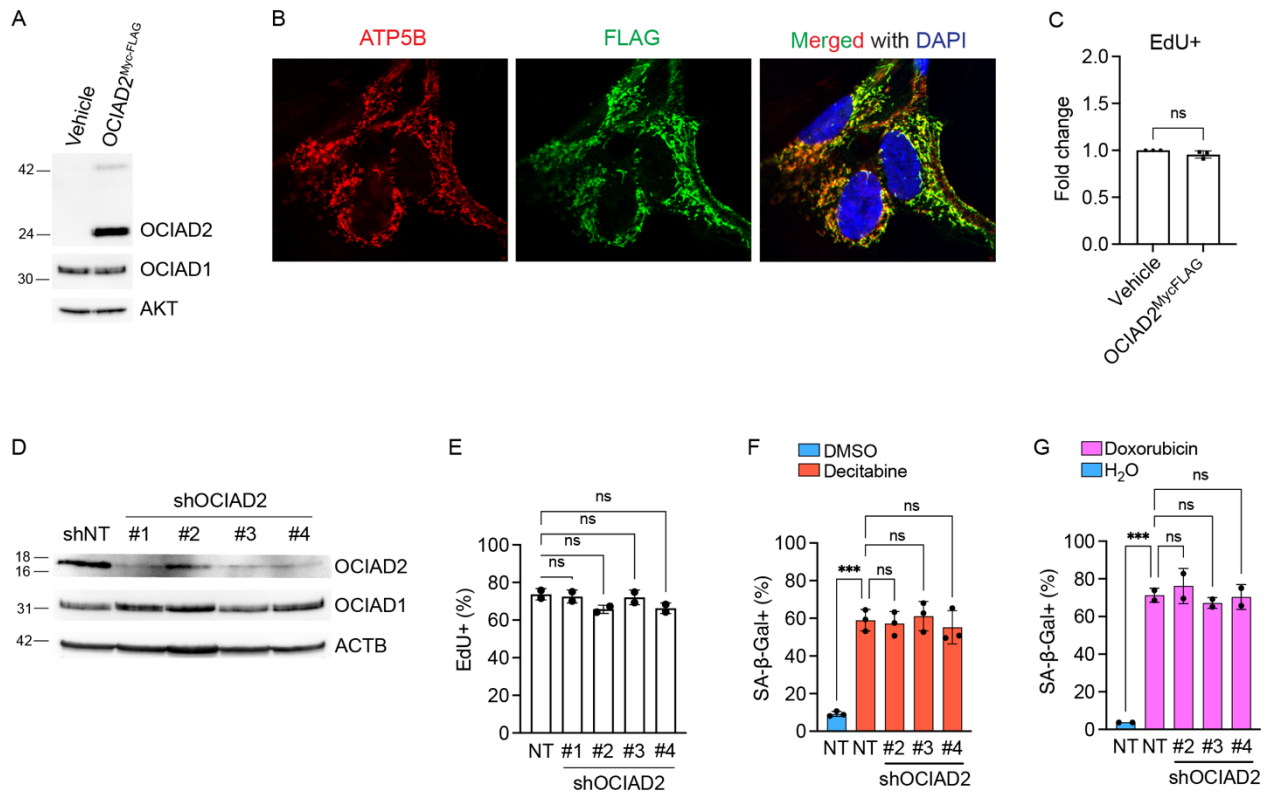


Figure 5.2.3 OCIAD2 is neither sufficient nor required to induce TIS in fibroblasts

(A) A representative western blot of OCIAD2 tagged with Myc-FLAG at c-terminus. Vehicle expresses Myc-FLAG without OCIAD2. AKT was used as a loading control. n=2

(B) Immunostaining of OCIAD2^{MycFLAG} cells. ATP5B is used as a mitochondrial marker. A representative image is shown. n=2

(C) EdU assay of cells from (A). Fold change was transformed to log2 value and subject to statistical analysis. Welch t-test. n=3

(D) Assessment of knockdown efficiency by western blots. 4 different OCIAD2-targeting oligos were used.

(E) EdU assay of cells from (D). One-way ANOVA, Dunnett correction. n=2

(F, G) SA-β-Gal assay. One-way ANOVA, Dunnett correction. n=3 (F), n=2 (G).

5.2.4 OCIAD2 supports expression of ECM-related genes regulated by TGF-β signaling in TIS fibroblasts

Since OCIAD2 was found to be not essential for the establishment of CS, I next reasoned that it would affect the quality of the established senescent cells. One way to assess the quality of CS is to examine its transcriptome as the major regulators of CS are transcription factors. To this end, both proliferating and senescent OCIAD2 stable knockdown cells were subjected to the bulk RNA-seq analysis (Figure 5.2.4 A). PCA plot of the RNA-seq data showed that the TIS (that is, treatment) caused the major difference rather than OCIAD2 (that is, genotype) in the transcriptome (Figure 5.2.4 B), which was expected by the dispensability of OCIAD2 in the TIS. After confirming the significant reduction of OCIAD2 mRNA level (Figure 5.2.4 C), the DEGs altered by OCIAD2 in the TIS were selected. That is, genes that were significantly changed in TIS were selected. Among those, chosen were genes that significantly blocked such changes in all 3 different shOCIAD2 cells. As a result, 110

genes were upregulated and 19 genes downregulated in the TIS fibroblasts in an OCIAD2-dependent manner (Figure 5.2.4 D). Among the 129 genes were only 2 other mitochondrial genes (MRPS6, PRSS35) than OCIAD2, indicating that the main transcriptomic change of TIS fibroblasts by OCIAD2 applies little or no to the expression of mitochondrial genes. These 129 genes were then examined by the over-representation analysis to find out the pathways affected by OCIAD2 as well as the upstream regulators which would explain such changes. Interestingly, the over-representation analysis yielded a network of genes related to the extracellular matrix (ECM) such as collagen and integrin genes (Figure 5.2.4 E; ITGB4, COL1A2, etc.). In detail, the major databases including GO, KEGG, and Reactome all yielded the same pathways enriched that are related to the ECM biology (Figure 5.2.4 F). The upstream regulator analysis of the 129 DEGs in turn predicted transforming growth factor beta (TGF- β) as the most significantly activated gene that positively regulates the 129 DEGs (Figure 5.2.4 G). Of note, TGF- β has been shown to be activated in CS to regulate the temporal dynamics of the SASP. Another interesting point is that it has been found by others that OCIAD2 *per se* is positively regulated by the TGF- β signaling. For example, the meta-analysis that thoroughly integrated 20,591 transcriptomics data for 46 different human cytokine responses in different cell types indicated OCIAD2 was upregulated in nearly all experiments when treated by TGF- β 1 with diverse doses and time points in different human cell types (Figure 5.2.4 H). These two results together suggest that TGF- β upregulates OCIAD2 and that upregulated OCIAD2 supports the expression of the TGF- β signaling target genes.

In conclusion, the RNA-seq analysis revealed that OCIAD2 supports the expression of ECM-related genes that are regulated by TGF- β signaling in the TIS fibroblasts.

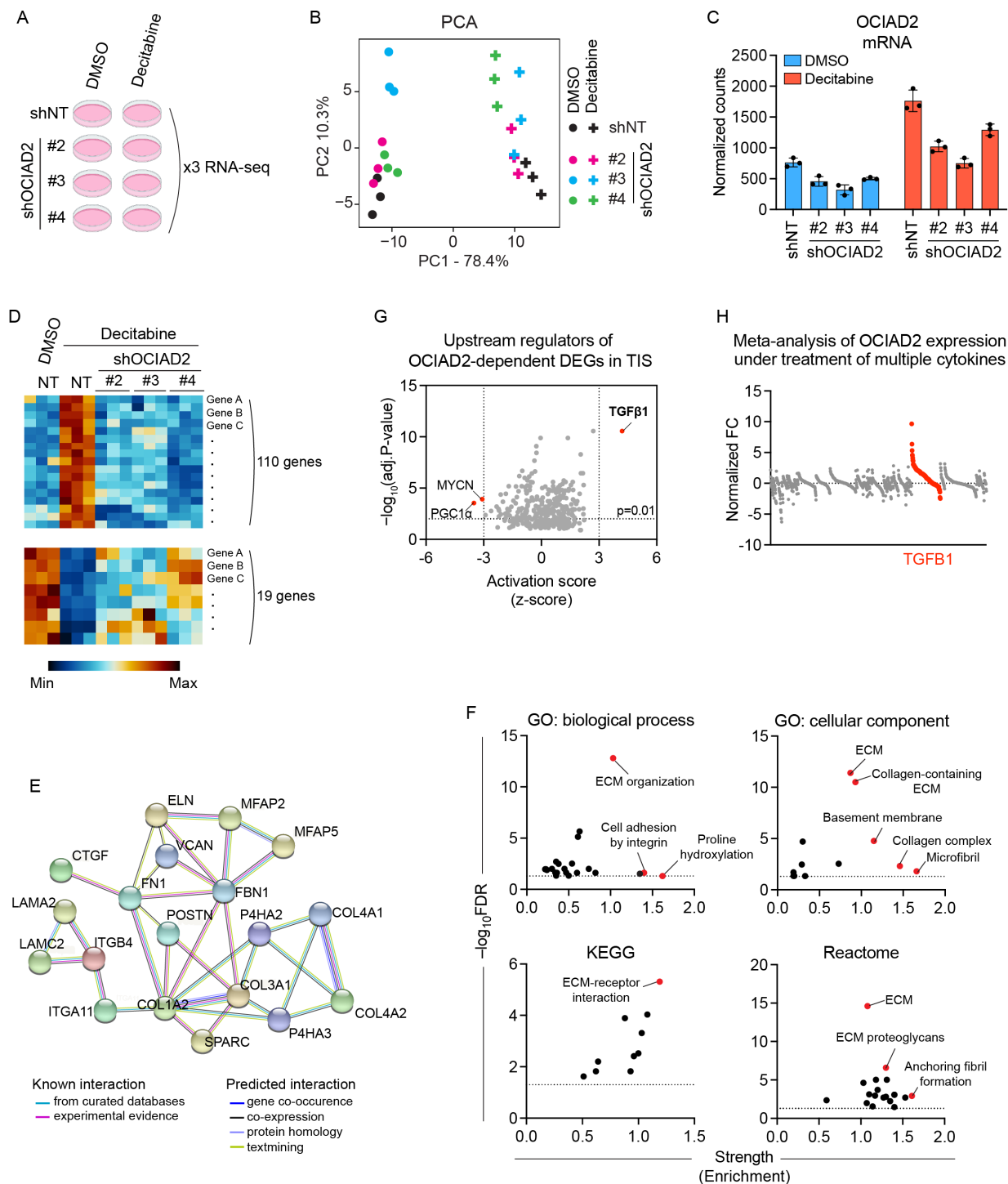


Figure 5.2.4 OCIAD2 supports expression of ECM-related genes regulated by TGF- β signaling in TIS fibroblasts

(A) Experimental setup for RNA-seq. (B) PCA plot of RNA-seq result. (C) Level of OCIAD2 mRNA from the RNA-seq result. n=3

(D) Schematic flow of analysis of OCIAD2-dependent DEGs in TIS.

(E) Interactive network of OCIAD2-dependent DEGs from selected from (D). The biggest network with highest confidence is shown.

(F) Over-representation analysis of OCIAD2-dependent DEGs selected from (D). GO, KEGG and Reactome databases were used.

(G) Upstream regulator analysis of DEGs selected from (D) by Ingenuity Pathway Analysis®. Ones with highest z-score are labelled.

(H) OCIAD2 expression levels from the published transcriptomics meta-analysis of 46 cytokines. Each dot represents a single result from the transcriptomics data comprised of different time points, different cell lines and different doses of cytokines treated. TGF β 1 is in red color among the total 46 cytokines.

5.2.5 OCIAD2 affects neither mitochondrial respiration nor superoxide level in TIS fibroblasts

I next asked how the mitochondrial gene OCIAD2 could regulate the TGF- β signaling in the TIS. I reasoned that OCIAD2 would regulate mitochondrial functions related to the TGF- β signaling. One of the well-known effects of TGF- β on mitochondria is that it increases the mitochondrial superoxide level and respiration. Hence these two parameters were vet in the TIS fibroblasts. Contrary to the expectation, there was no observable difference in mitochondrial superoxide level of the TIS fibroblasts regardless of the OCIAD2 knockdown (Figure 5.2.5 A). This was also true when cells were treated with MitoParaquat, a selective superoxide generator within mitochondria (Figure 5.2.5 B). Moreover, the OCIAD2 overexpressing fibroblasts in the TIS did not yield any different superoxide levels as well (Figure 5.2.5 C). These data demonstrate that OCIAD2 does not affect the mitochondrial superoxide level in the TIS fibroblasts. Next, mitochondrial respiration was measured. The Seahorse analysis revealed that there was no difference in any parameter of mitochondrial respiration of the TIS fibroblasts in spite of the stable knockdown of OCIAD2 (Figure 5.2.5 D). Like the superoxide level, the respiration did not change in the OCIAD2 overexpressing TIS fibroblasts (Figure 5.2.5 E).

Altogether, these data demonstrate that OCIAD2 affects neither the mitochondrial superoxide level nor respiration in the TIS fibroblasts.

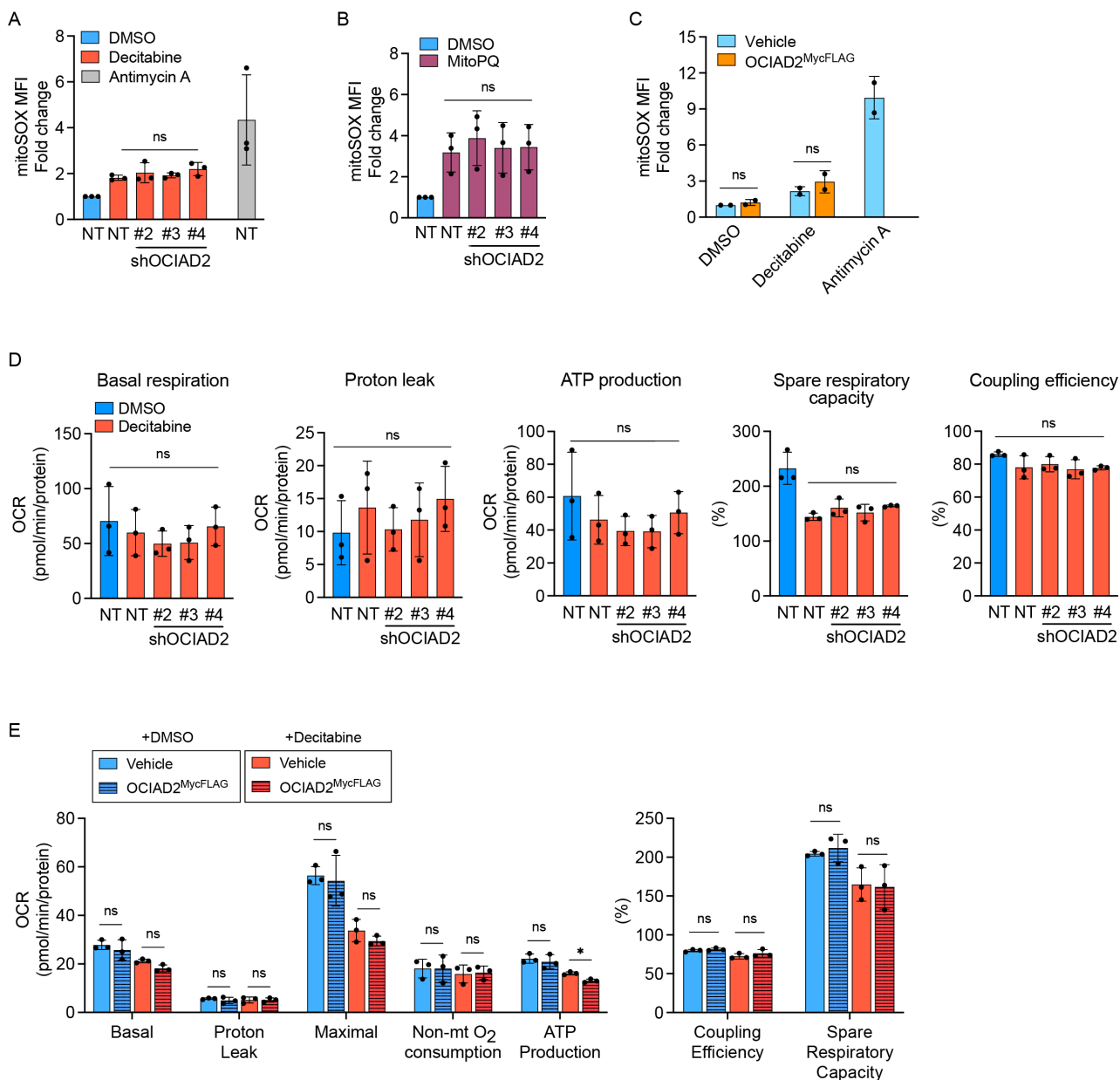


Figure 5.2.5 OCIAD2 affects neither mitochondrial respiration nor superoxide level in TIS fibroblasts

(A-C) Mitochondrial superoxide level measured with mitoSOX dye. Antimycin A (10 μ M, 30 min) was used as a positive control.

MitoParaquat: 40 μ M, 3 day. (A, B) One-way ANOVA, Dunnett correction, n=3. (C) Mann-Whitney test, Holm-Sidak correction. n=2

(D, E) Mitochondrial respiration analyzed by Seahorse. (D) One-way ANOVA, n=3. (E) Welch t-test, Bonferroni-Dunn correction. n=3.

5.2.6 OCIAD2 does not alter mitochondrial metabolism of nutrients in TIS fibroblasts

Other effects of TGF- β on mitochondria are to increase the glutaminolysis and glycolysis by upregulating the enzymes GLS1 and HK2 each responsible for metabolizing glutamine and glucose in association with mitochondria. Hence the metabolism of glucose and glutamine was analyzed. However, against the expectation, the Seahorse analysis did not yield any notable difference in glycolysis of the TIS fibroblasts due to the reduction of OCIAD2 (Figure 5.2.6 A). In addition, the

analysis of glucose flux into the glycolytic pathway by feeding mass isotopologue $^{13}\text{C}_6$ glucose to the TIS fibroblasts did not show any difference in both 2 different feeding time points (Figure 5.2.6 B). Thus, it was ruled out that OCIAD2 regulates glycolysis in the TIS fibroblasts. Next, the glutaminolysis was measured by feeding cells with $^{13}\text{C}_5$ glutamine. 5 hours of feeding glutamine labelled nearly 80% of αKG and 50% of fumarate whereas those labelled by glucose were less than 1% (Figure 5.2.6 C), which is consistent with the well-known fact that glutamine is the major anaplerotic source of TCA cycle metabolites. Nonetheless, the glutamine catabolism was not significantly attenuated in the OCIAD2 knockdown TIS fibroblasts, although it reached the statistical significance partly in the decitabine-induced and doxorubicin-induced senescent fibroblasts (Figure 5.2.6 C). Lastly, the mitochondrial fatty acid β -oxidation was measured by feeding $^{13}\text{C}_{16}$ palmitic acid to cells. Like glucose and glutamine, palmitate flux into the cells was not changed by OCIAD2 in the TIS fibroblasts (Figure 5.2.6 D).

These data together speak against the possible role of OCIAD2 in regulating the mitochondrial metabolism of glucose, glutamine, or fatty acid in TIS fibroblasts.

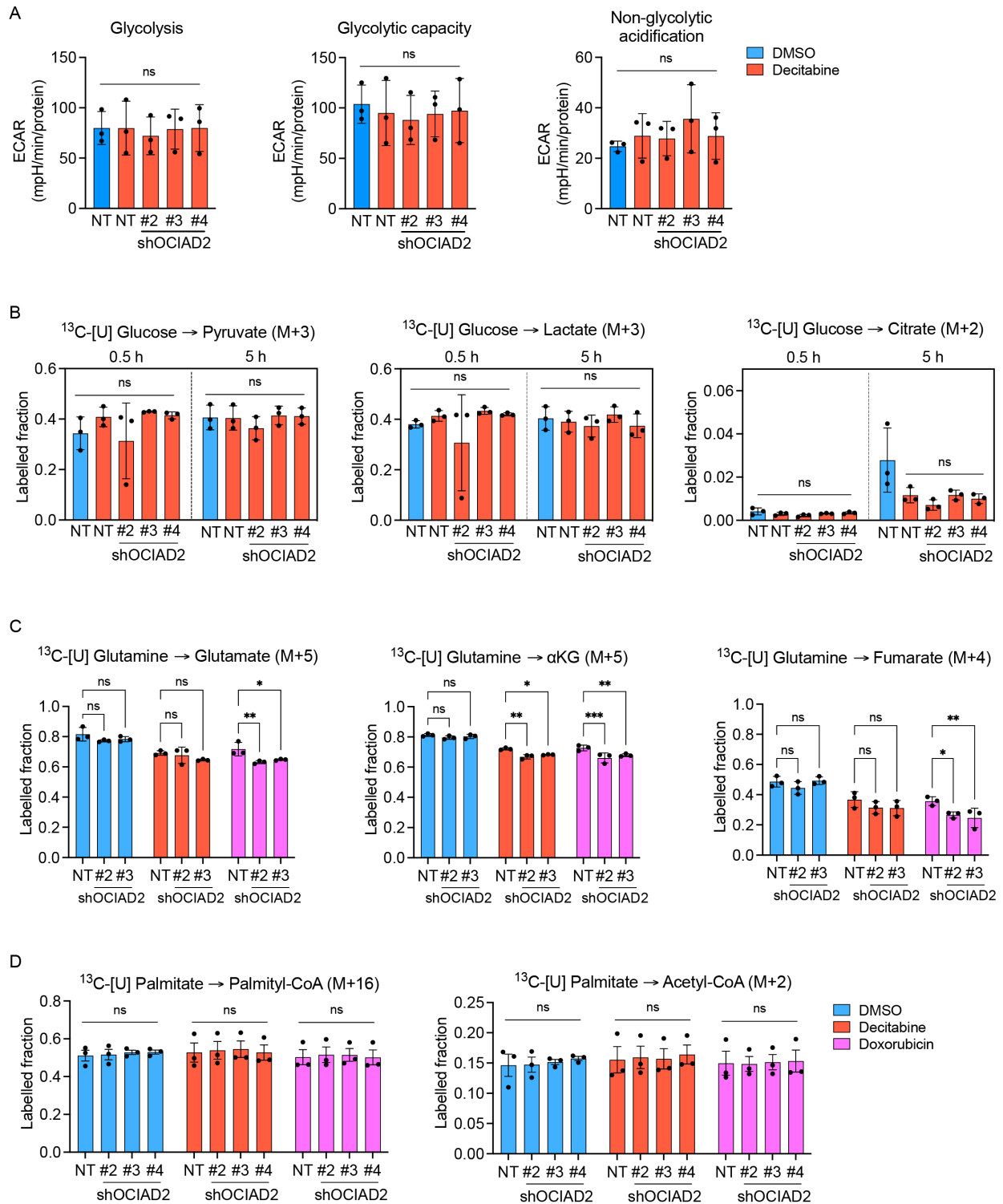


Figure 5.2.6 OCIAD2 does not alter mitochondrial metabolism of nutrients in TIS fibroblasts

(A) Glycolysis assay by Seahorse. ECAR: extracellular acidification rate. One-way ANOVA, n=3.

(B) Glycolysis assay by tracing glucose uniformly labelled with ^{13}C isotope (5.5 mM). One-way ANOVA. n=3

(C) Glutaminolysis assay by tracing glutamine uniformly labelled with ^{13}C isotope (2 mM, 5 hours). Two-way ANOVA, followed by multiple comparisons on each treatment, Dunnett correction. n=3

(D) Fatty acid β -oxidation assay by tracing palmitate uniformly labelled with ^{13}C isotope (10 μM , 7 hours). Two-way ANOVA, followed by One-way ANOVA on each treatment. n=3

5.2.7 OCIAD2 promotes formation of mitochondrial clump at perinuclear region in TIS fibroblasts

Having ruled out the possibilities of OCIAD2 regulating mitochondrial superoxide, respiration, and metabolism, I focused on the mitochondrial morphology as it is a critical mitochondrial feature that has not been investigated yet. In addition to the dramatic increase of mitochondrial volume in a TIS fibroblast, it was observed that there was a significant increase in mitochondrial clumps around the nucleus. Of note, such a mitochondrial clump in the perinuclear region was observed nearly only in the cell that has little or no OCIAD2 expression upon the establishment of the TIS (Figure 5.2.7 A), showing that it is inversely correlated to the level of OCIAD2. In fact, such clumps were reduced in all 3 different OCIAD2 stable knockdown cells particularly in accordance with the degree of the OCIAD2 reduction (Figure 5.2.7 B, 5.2.4 C). These data strongly argue that OCIAD2 is required to form the perinuclear mitochondrial clump in the TIS fibroblasts. Since OCIAD2 is found to be dispensable for other mitochondrial features tested as well as the establishment of the TIS, it remains to be studied about the biological meaning of the clump promoted by OCIAD2 in the TIS fibroblasts.

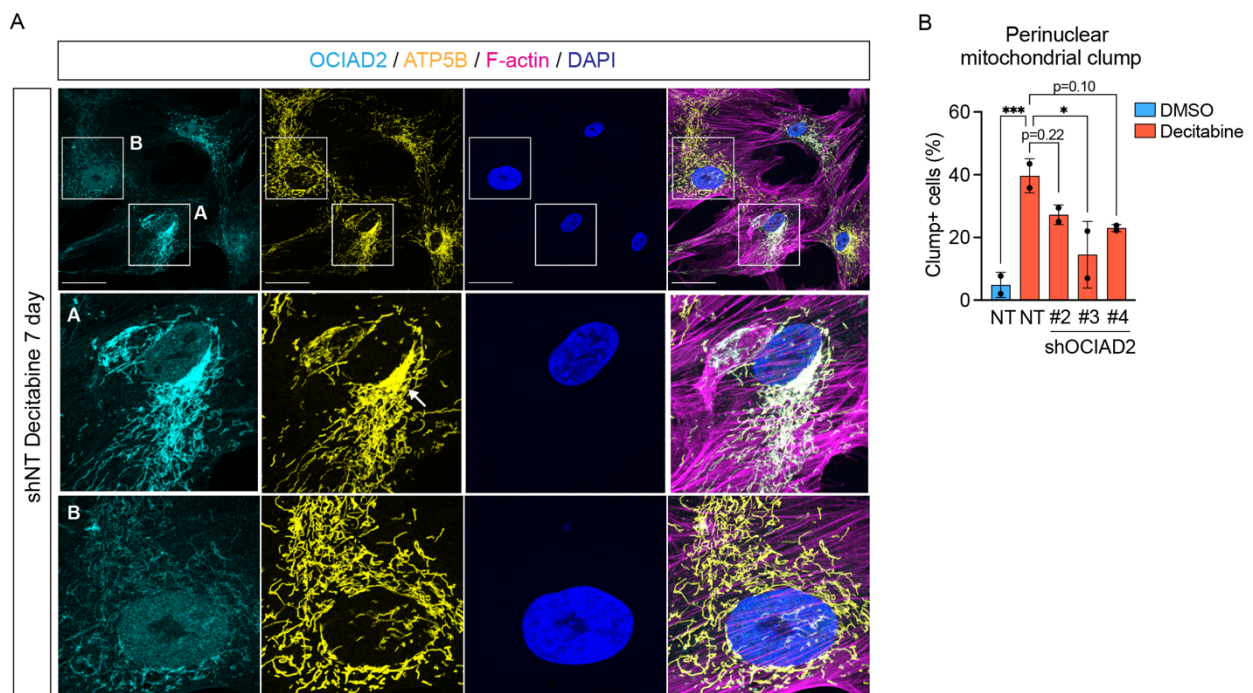


Figure 5.2.7 OCIAD2 promotes formation of mitochondrial clump at perinuclear region in TIS fibroblasts

(A) Representative images with perinuclear mitochondrial clump associated with OCIAD2 expression level. The clump is indicated by a white arrow. A: high OCIAD2, B: low OCIAD2. Scale bar: 100 μ m.

(B) Quantification of cells with the perinuclear mitochondrial clump. Counted were 17-97 cells per condition per replicate. One-way ANOVA, Dunnett correction. n=2

5.2.8 Analysis of OCIAD2 interactome in the TIS fibroblasts

To gain insights into the function of OCIAD2 in the TIS mitochondria, physically binding proteins of OCIAD2 were examined. The TIS was established by decitabine in either the wild-type or OCIAD2^{MycFLAG} overexpressing cells and the mitochondria-enriched fraction was obtained from them. Then the immunoprecipitated eluate by FLAG magnetic beads from the fractions was analyzed by mass spectrometry to map the interactome of OCIAD2 (Figure 5.2.8 A). The wild-type rather than vehicle (empty vector transduced) cells were used as a control to have a clean background without any FLAG expression. As a result, 225 proteins were significantly enriched in the overexpressing mitochondria and 143 proteins were MitoCarta 3.0 among them (Figure 5.2.8 B). OCIAD2 was found to be the most enriched protein above all, confirming the validity of the experiment. Proteins were then selected based on the region in the graph where there are only MitoCarta 3.0 proteins with the high enrichment and high significance designated as the MitoCarta exclusive interactors which yielded 27 proteins (Figure 5.2.8 C). Out of them, 23 proteins were either MIM or IMS proteins, corroborating the validity of the experiment given that OCIAD2 is localized at the inner membrane. Lastly, selected were proteins exclusively detected in OCIAD2^{MycFLAG} expressing cells since there is supposed to be no protein in the FLAG IP eluate of wild-type cells which do not express FLAG peptides. According to these criteria, the finalists were 9 proteins (Figure 5.2.8 C; green color). They were equally interesting proteins, yet any notable similarity among their functions was not found. Thus, it remains to be found the function of OCIAD2.

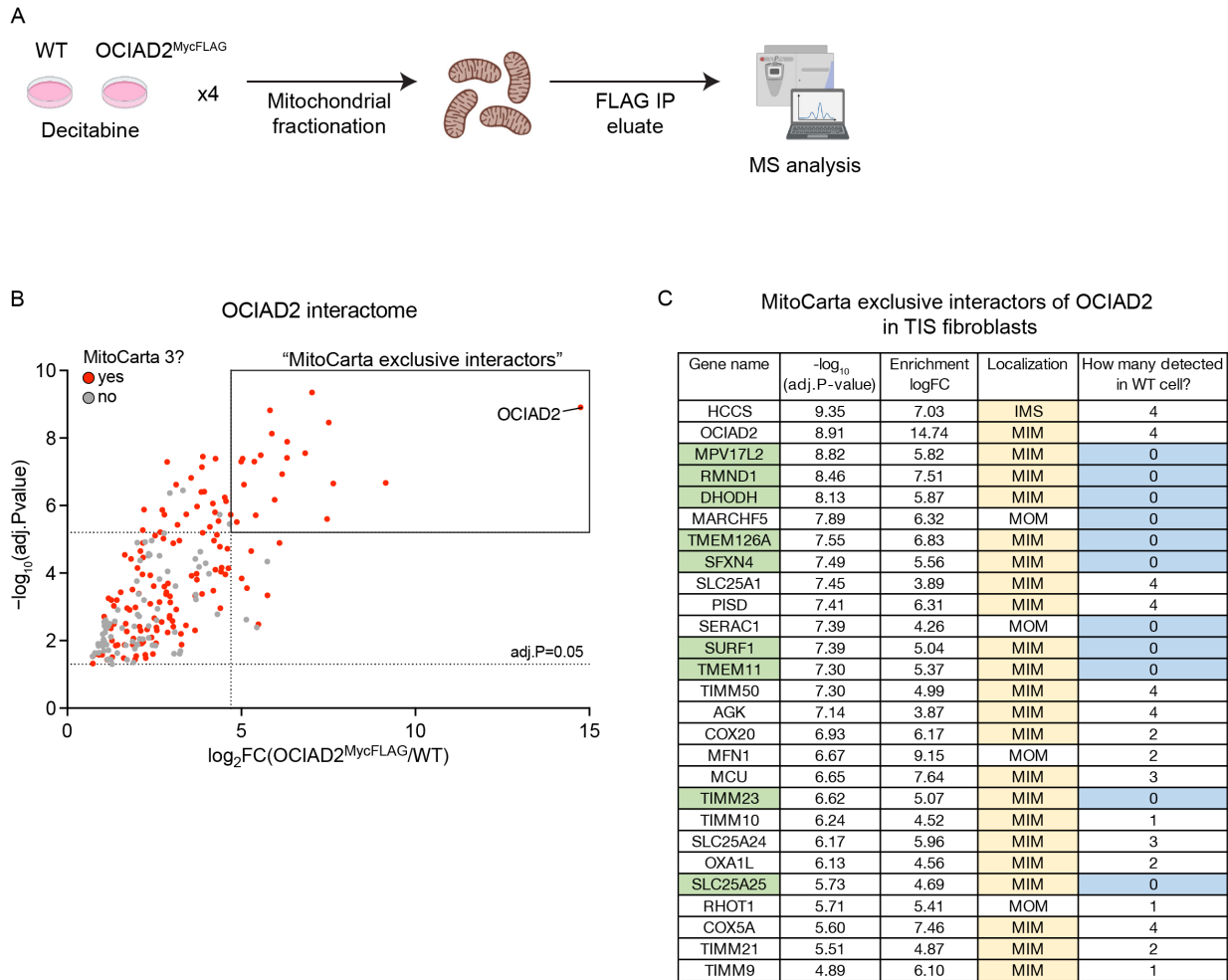


Figure 5.2.8 Analysis of OCIAD2 interactome in TIS fibroblasts

(A) Schematic workflow of OCIAD2 interactome analysis by label-free LC-MS/MS. n=4

(B) Significantly enriched proteins in FLAG IP eluate. Statistical analysis by Benjamin-Hochberg method. n=4

(C) List of proteins selected from (B). MIM: mitochondrial inner membrane, MOM: mitochondrial outer membrane, IMS: intermembrane space. Green: the final list, yellow: MIM proteins, blue: exclusively detected in OCIAD2^{MycFLAG} cells

5.2.9 OCIAD2 is stabilized by YME1L1 loss-of-function

Previous work from our lab suggested that OCIAD2 is a proteolytic substrate of mitochondrial protease YME1L1. Indeed, it was confirmed that the stability of OCIAD2 is increased in YME1L1 knockout HeLa cells by re-analyzing the same samples from the previous work (Figure 5.2.9 A). Moreover, preliminary data in HEK293 cells reproduced the finding from the very previous work done in mouse embryonic fibroblasts (MEF) and HeLa cells that OCIAD2 is degraded under hypoxia in a YME1L1-dependent manner (Figure 5.2.9 B). Our lab also showed that the substrates of YME1L1 found *in vitro* were true *in vivo* in the mouse model of the neuron-specific Yme1l1 knockout. OCIAD2 level in the mouse model was assessed as it was not shown before. Interestingly, a western blot analysis of several neuronal tissues of the mice revealed that OCIAD2 was not always accumulated in all

Yme111 knockout neuronal tissues (Figure 5.2.9 C). It is also noteworthy that the accumulation of OCIAD2 was negatively associated with the inflammatory phenotypes of the tissues. For instance, the previous work found neuroinflammation and axonal degeneration in the retina and spinal cord at the age of 6-7 weeks but no sign of inflammation or anomaly was observed in the forebrain or cerebellum until the age of 31-32 weeks when the mice were sacrificed due to ethical reasons.

All in all, the data showed that OCIAD2 is stabilized by the YME1L1 loss-of-function and suggest the presence of a possible factor to link OCIAD2 and YME1L1 *in vivo*.

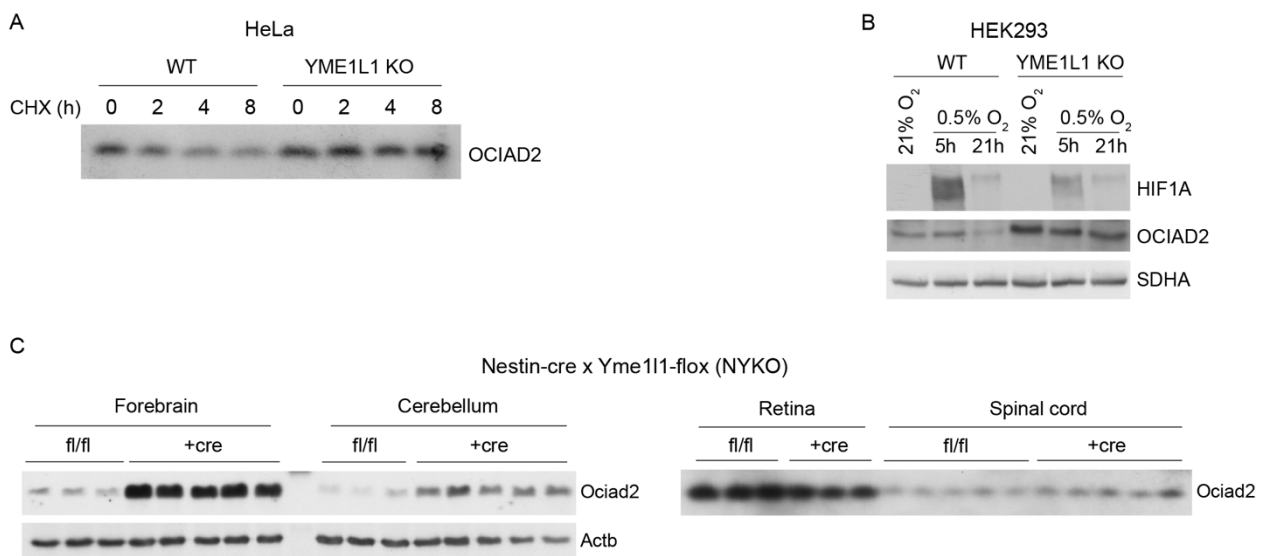


Figure 5.2.9 Stabilization of OCIAD2 by loss-of-function of YME1L1

(A) Re-analysis of OCIAD2 stability in HeLa cells from the published work by western blot. CHX: cycloheximide 100 µg/mL. n=1

(B) Western blot analysis of OCIAD2 stability under hypoxia in HEK293 cells. SDHA is the loading control. n=1

(C) Re-analysis of OCIAD2 in neuronal tissues of NYKO mice from the published work. Tissues were from 31-32 weeks old mice. Each lane represents an independent mouse. Actb is the loading control. n=3-5

5.2.10 Generation of whole-body Ociad2 knockout mice

To learn the function of OCIAD2 *in vivo*, the whole-body Ociad2 knockout mice were generated by introducing a premature stop codon to the exon 4 in the Ociad2 genomic locus of the mouse embryo using CRISPR-Cas9 technology (Figure 5.2.10 A). A subsequent genotyping confirmed a successful introduction of the intended premature stop codon to the loci. The Ociad2 knockout mice were born Mendelian ratio (Figure 5.2.10 B) and displayed the same body weight development in both males and females (Figure 5.2.10 C). Ociad2 was highly abundant in the liver, lung, and pancreas compared to the heart and kidney (Figure 5.2.10 D). Especially, the abundance in the lung was the most pronounced when compared to SDHA level which is a crude index of

mitochondrial respiration. Nevertheless, there had been no noticeable phenotype up to the age of 69 weeks in the knockout mice (BfR evaluation total score: 0-1).

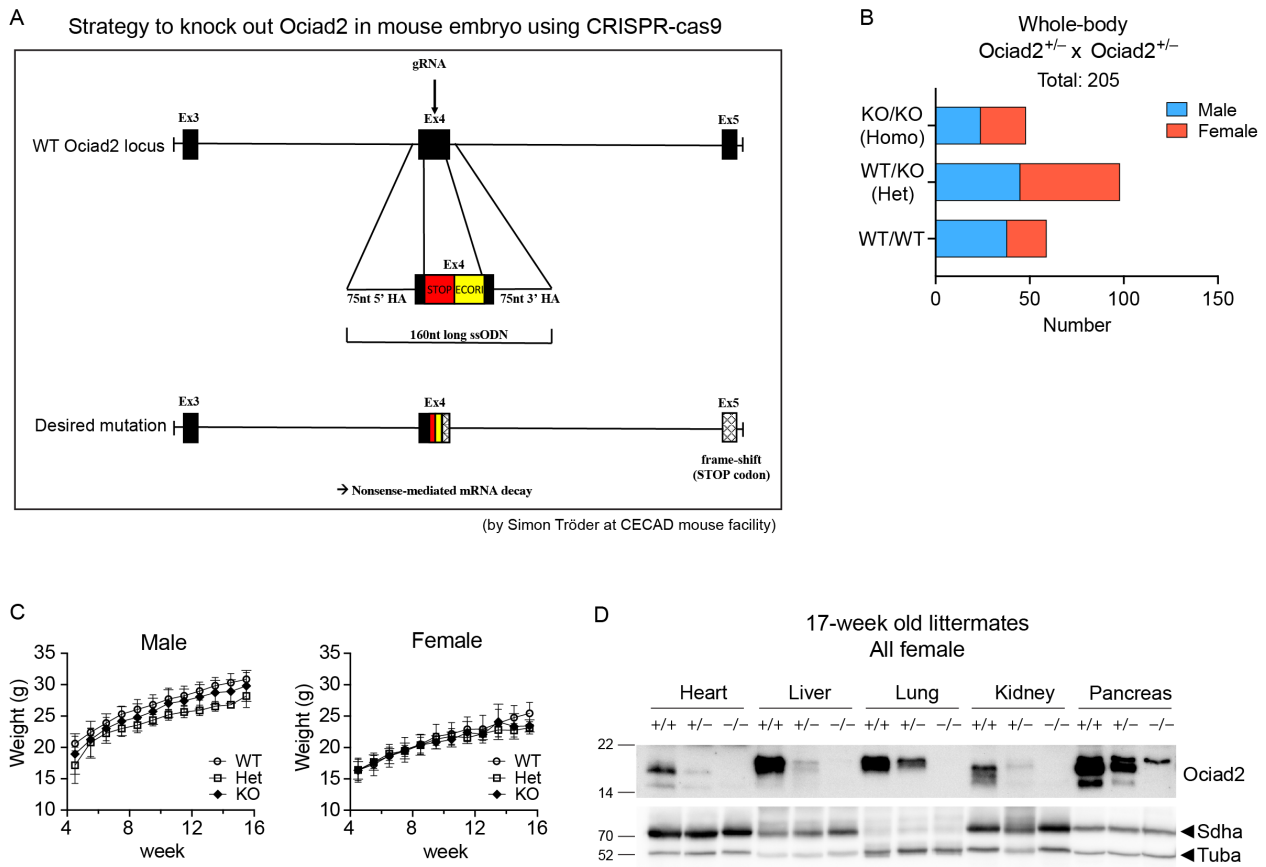


Figure 5.2.10 Generation of whole-body *Ociad2* knockout mice

(A) Schematic depiction of strategy to generate whole-body *Ociad2* knockout mice.

(B) Birth ratio between *Ociad2* WT, heterozygous and homozygous mice. n=205

(C) Body weights of mice with different *Ociad2* genotypes. Body weights were measured weekly from the age of 4.5 to 15.5 weeks. For male, WT: n=8, Het: n=2, KO: n=9. For female, WT: n=4, Het: n=11, KO: n=7.

(D) Western blot of mice tissues with different *Ociad2* genotypes. *Sdha* and *Tuba* was used as index of mitochondrial and cytosolic protein amount. n=1

6. Discussion

6.1 Resolving paradox of mitochondrial features in CS

This study largely resolved the paradoxical status of mitochondria by taking mitochondrial volume into account. Many studies reported that mitochondria are dysfunctional in senescent cells, based on the observation of increased mtROS levels and decreased MMP. However, these mitochondria as a whole were found to have higher respiration and metabolic activity with functional contributions to the CS. Although there were several attempts to consider the increased mitochondrial mass when measuring the functions, to my knowledge, none of them took the 3-dimensional volume into account. The mitochondrial volume measured in this study is far bigger than the one from 2-dimensional planes. The volume was increased over 12-fold in the TIS cells, whereas several other studies reported the increase is around 3-fold (22, 139, 163). The 2-dimensional image-based quantification is one intuitive reason for the discrepancy. Another reason would be a misleading result of Mitotracker dye as a proxy of the mitochondrial mass. Although this dye is largely known to be insensitive to MMP, it was observed in fact a clear reduction of the intensity by CCCP treatment (Figure 5.1.3 F). Thus, calculating the mitochondrial mass by Mitotracker dye yields a largely underestimated value due to the depolarized mitochondria in senescent cells. Moreover, the Mitotracker intensities in the TIS cells were comparable with those of TMRM and mitoSOX in accordance with other reports (163, 170).

Nevertheless, one should be cautious to interpret the data present in this study. The mitochondrial parameters scaled by the mitochondrial volume yielded a general decrease of nearly any measured parameter in this study. However, these are mean values. What could be true is that there are distinct subpopulations of mitochondria with varying amplitudes of activity. That is, only a subset of mitochondria in the TIS cells has higher MMP to yield overall higher MMP when measured per cell. This could be true for mtROS too, although this population is not likely to overlap the other with higher MMP. This hypothesis could be tested by imaging the mitochondria in senescent cells in the future. Another lesson from this study is that the generally used markers as a proxy of mitochondrial abundance do not faithfully reflect their true abundance. Other than Mitotracker, mtDNA copy number is often used as a readout of mitochondrial amount. However, as shown in this study (Figure 5.1.3A), it does not represent the true amount of the mitochondria. As summarized in the table (see 2.3.3), there are conflicting results about the mitochondrial states across the different cell types and stimuli. While this could, by all means, be true mitochondrial states, I presume this too is largely due to the negligence of taking an accurate mitochondrial abundance into account. Thus, it warrants the test as such.

What is not addressed in this study despite importance is the mechanism of mitochondrial accumulation in senescent cells. Countless studies reported the accumulation of mitochondria in senescent cells. Some of the studies suggested multiple scenarios, including diminished mitochondrial turnover, reduced mitophagy, and early and transient activation of mitochondrial biogenesis. However, the proteomic analysis in this study does not support such reductions at least by the level of the genes that are involved in mitochondrial dynamics and surveillance (Appendix 2; Dynamics & Surveillance). Contrary to the previous reports (145, 171), mitochondrial fission factor FIS1 was one of the highest upregulated proteins on day 7. Moreover, another fission factor MFF was also upregulated. It is also noteworthy that several fusion factors were also increased, including MFN2 and OPA1. Thus, the proteomic data in this study do not explain the increased mitochondrial volume (and tubulation). It remains to be determined which factors are critical for eliciting the mitochondrial accumulation in TIS cells.

6.2 Potential role of rewired mitochondria in CS

In this study, mitochondria were found to rewire their proteome as well as metabolism in TIS. The proteomic rewiring largely pointed to an increase in the mitochondrial membrane proteins in contrast to a decrease in the matrix proteins (Figure 5.1.5D). Detailed categorization of mitochondrial genes revealed that particularly metabolism-related genes were heavily increased (Appendix 2; Metabolism), in contrast to the mtDNA-related genes (Appendix 2; Central dogma). The general decrease in mtDNA-related genes associated with a reduced mitochondrial translation explains well the lowly energized mitochondria in the TIS cell. Thus, the general increase in metabolism-related genes is not likely attributed to the mitochondria with low bioenergetics. Indeed, the proteomic analyses suggested an early enhancement of BCAA catabolism, followed by the increase in lipid metabolism (Figure 5.1.5E). The enhanced BCAA catabolism was validated by the metabolic flux analysis using stable isotope tracers (Figure 5.1.7F). This enhancement was not led to an increase in OCR (data not shown). Moreover, preliminary data showed that the BCAA carbons did not reach the TCA cycle. Another data hinted that the downregulation of BCAA catabolism in TIS cells led to reduced intracellular levels of neutral lipids (all data not shown). These data collectively suggest that the enhanced BCAA catabolism supports not only NEAA synthesis (Figure 5.1.7F) but also lipogenesis in TIS. Of note, a general accumulation of lipids with a marked alteration of lipid profile in senescent cells have been reported (159, 160, 205-207). Moreover, the physiological role of BCAA catabolism was shown to provide lipogenic CoA molecules in adipose tissue and pancreas (108, 114, 208, 209). Thus, it could be hypothesized that enhanced BCAA catabolism in senescent cells is to support lipogenesis. Nevertheless, it is not completely understood yet the role of accumulated lipids in

senescent cells. Based on the preliminary OCR data abovementioned, it appears to be irrelevant to mitochondrial energy production. Therefore, it is warranted to test the role of enhanced BCAA catabolism and lipogenesis in TIS.

Unlike the BCAA catabolism, early downregulation of the 1C-folate pathway is not surprising in that its major significance is to provide nucleotides. Senescent cells would have lower demand for nucleotides due to a lack of proliferation. Indeed, a stark depletion of dNTPs was reported in the OIS (210). What was striking is that adding nucleosides in the OIS cells made them exit from the senescence, suggesting that dNTP reduction is not a mere consequence but a driver and sustainer of the OIS. However, it is unclear whether the reduction of 1C-folate metabolism is specific to the CS rather than quiescence, both of which are cell-cycle arrested states and would have a reduced demand for dNTP level. Thus, it remains to be elucidated about the causality of the curtailed 1C-folate metabolism in the TIS.

Another interesting observation is the altered ratio of purine/pyrimidine caused by the selective depletion of purines in TIS cells (Figure 5.1.6C, Appendix 4). In a normal cell, the abundance of pyrimidine is generally higher than purine. Certain pathological circumstances (e.g., urea cycle dysregulation) can exaggerate the pyrimidine to purine ratio (211). Interestingly, this ‘pathological’ ratio promoted genomic transversion mutations in cancer cells. That is, pyrimidine tends to be incorporated in lieu of purine presumably due to its overriding abundance. The idea that such an imbalance could lead to mutagenesis was more directly proven in yeast (212). This raises an interesting point that why senescent cells maintain the imbalanced ratio. While purine is synthesized from the 1C-folate pathway, pyrimidine synthesis requires IMM protein DHODH to catalyze the reaction from orotate to dihydroorotate. DHODH requires ETC activity for its function. This means senescent cells somehow maintain the pyrimidine level even with the bioenergetically hypoactive mitochondria. Thus, it would be interesting to investigate the role of the purine/pyrimidine imbalance in senescent cells, let alone the mechanism through which it is achieved.

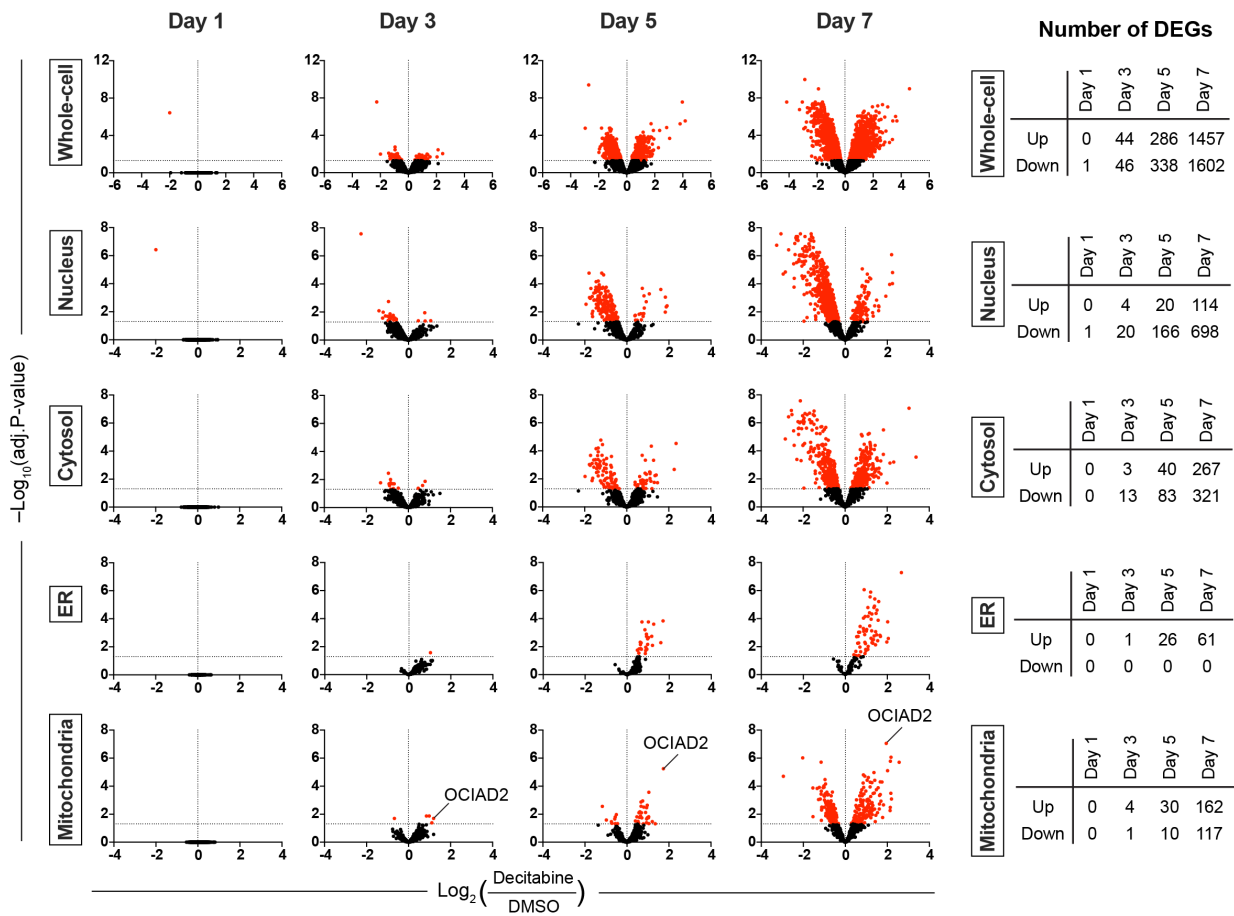
6.3 And still: the elusive orphan gene OCIAD2

This study identified OCIAD2 as a pan-senescence marker (Figure 5.2.1) besides cancer. Moreover, OCIAD2 was the earliest upregulated mitochondrial protein with the highest statistical significance (Appendix 1; mitochondria). This made OCIAD2 highly plausible to be a causal factor for CS. In the subsequent analyses, it was found that OCIAD2 has crosstalk with TGF- β signaling in TIS (Figure 5.2.4) and it promotes perinuclear clustering of mitochondria in TIS cells (Figure 5.2.7). Perinuclear clustering of mitochondria was observed in several stress conditions including senescence, apoptosis, hypoxia, and heat shock (147, 213-215). From these studies, it was found that the clustering

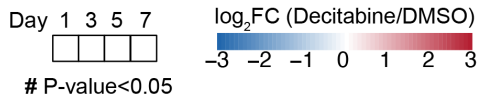
is largely mediated by HIF1A signaling. Interestingly, the perinuclear clustered mitochondria were shown to be a source of ROS or cholesterol to the nucleus. Of note, these mitochondria are morphologically distinct from hypertubulated mitochondria observed in, for example, DRP1 knockout cells. While mitochondria in DRP1 knockout cells are relatively well distributed with hypertubulated and elongated morphology (216), the perinuclear clustered mitochondria are clustered around the nucleus (hence is the name) often with strong polarity toward one side of the nucleus (215). However, in this study, these observations were not associated with any mitochondrial parameter that is known to be altered in senescent cells. This includes ETC function, mtROS, TCA cycle activity, glycolysis, glutaminolysis, and FAO (Figure 5.2.5, 5.2.6). Thus, it is still elusive about the role of OCIAD2 in forming perinuclear clustered mitochondria and its potential relevance with TGF- β signaling.

Only recently, the exact localization of OCIAD2 was demonstrated to be the IMM (178, 179). After having confirmed these results (Figure 5.2.2), the interactome of OCIAD2 in TIS was investigated to find out its direct function(s) in TIS. After stringent criteria, the final 9 proteins were regarded as *bona fide* interactors of OCIAD2 (Figure 5.2.8C). These 9 proteins have little in common in regard to the function, which makes it elusive to infer the OCIAD2 function. However, at least, we could rule out its possible interaction with OCIAD1, against the previous report (175). In fact, nearly all but one report differentiated the biology of OCIAD1 and OCIAD2. For example, in any given biological setting, OCIAD1 and OCIAD2 were not identified together (177-187). In agreement with this, the proteomic analyses in this study did not identify OCIAD1 as DEG at any given time point. Moreover, the OCIAD1 level did not change in OCIAD2 knockdown or overexpressed cells (Figure 5.2.3A, D). This strongly argues that OCIAD2 has a distinct function from that of OCIAD1.

7. Appendix



Appendix 1. Volcano plots of organelle-specific proteome from the time-resolved proteomics data



Metabolism

Carbohydrate metabolism

#	SLC25A11
#	SLC25A1
#	SLC25A13
#	MCEE
#	OGDH
#	CS
#	PC
#	PK1
#	HMGCL
#	ME2
#	SLC25A12
#	IDH2
#	GOT2
#	IDH3B
#	HADHB
#	DCXR
#	GPD2
#	ACLY
#	ACO2
#	PDP1
#	AUH
#	DLST
#	SUCLA2
#	PCCB
#	OXCT1
#	D2HGDH
#	SDHA
#	IDH3G
#	PDP1
#	PCCA
#	DLAT
#	PDHB
#	IDH3A
#	PDHA1
#	ABHD11
#	ACAA2
#	MDH2
#	SUCLG1
#	SUCLG2
#	ACAT1
#	PDHX
#	DL
#	SDHB
#	FAHD1
#	FH
#	RPIA

Detoxification

#	CYB5B
#	MGST1
#	ALDH3A2
#	CYB5F3
#	GSTK1
#	PRDX6
#	TST
#	ABHD10
#	PRDX4
#	CAT
#	NIT1
#	ALDH1B1
#	ALDH2
#	GPX1
#	PRDX5
#	PRDX3
#	ALDH7A1
#	TXNRD2
#	ALDH9A1
#	OXR1
#	AKR7A2
#	TXNRD1
#	SELENOO
#	HAGH
#	NIT2
#	MPST
#	MSRB2
#	PRDX2
#	GPX4
#	SOD1
#	GSR
#	BPHL
#	MSRB3
#	CBR3
#	GLRX2

Sulfur metabolism

#	SOOR
#	TST
#	GOT2
#	SUOX
#	ETHE1
#	MPST
#	MSRB2

Lipid metabolism

#	SLC25A20
#	CYB5R3
#	SLC25A1
#	LACTB
#	SPTLC2
#	FDXR
#	CROT
#	PRDX6
#	ACSL1
#	MCEE
#	ACADVL
#	ACAA1
#	ACSF2
#	ETFDH
#	CRAT
#	MLYCD
#	ACADSB
#	EHHADH
#	CPT2
#	FDP5
#	ECI1
#	FASN
#	OXSM
#	ACOT9
#	CPT1A
#	HADHB
#	HSD17B4
#	HADHA
#	ACSF3
#	PISD
#	ECHDC1
#	ETFA
#	HSD17B10
#	CYP27A1
#	ACOT13
#	OSBP1A
#	ETFB
#	PCCB
#	DBI
#	ECI2
#	ECHS1
#	PTGES2
#	IDH1
#	PCCA
#	LYPLA1
#	ACADM
#	SCP2
#	DECR1
#	MCAT
#	ACAA2
#	ZADH2
#	ACAT1
#	HADH
#	MECR
#	ACOT7
#	ACAD10
#	TRIA1
#	GCSH
#	STARD7
#	HINT2
#	FDX1

Nucleotide metabolism

#	SLC25A4
#	NME3
#	NT5DC2
#	SLC25A6
#	AK4
#	SLC25A5
#	PPA2
#	AK3
#	SUCLA2
#	GUK1
#	SUCLG1
#	SUCLG2
#	NUDT9
#	DHODH
#	NUDT5
#	NUDT2
#	AK2
#	PAICS
#	NME4
#	HINT1
#	DTYMK
#	DUT

Amino acid metabolism

#	ALDH6A1
#	COMT
#	SFXN3
#	DHTKD1
#	SLC25A13
#	KYAT3
#	ETFDH
#	BCAT2
#	SFXN1
#	ACADSB
#	ALDH4A1
#	HMGCL
#	MCCC1
#	SLC25A12
#	HIBCH
#	ACAD8
#	SARDH
#	GCDH
#	ALDH18A1
#	GOT2
#	AASS
#	HADHB
#	GLUD1
#	BCKDHB
#	DBT
#	HADHA
#	HIBADH
#	OAT
#	ETFA
#	ALDH7A1
#	IVD
#	HSD17B10
#	AUH
#	GRHPR
#	DLST
#	LDHB
#	ALDH9A1
#	ETFB
#	BCKDK
#	ECHS1
#	AKR7A2
#	PYCR1
#	PYCR2
#	ACAA2
#	GLS
#	GPT2
#	ACAT1
#	HADH
#	DL
#	GCSH
#	SHMT2

Vitamin metabolism

#	SFXN3
#	FDXR
#	RDH14
#	ETFDH
#	PPGS
#	PC
#	SFXN1
#	PNPO
#	MCCC1
#	SARDH
#	FLAD1
#	ALDH1L2
#	ETFA
#	ALDH7A1
#	ETFB
#	MMAAHC
#	QDPR
#	PCCA
#	MTFMT
#	MMAB
#	RFK
#	PLPBP
#	MTHFD1L
#	MTO1
#	GTPBP3
#	SHMT2
#	GLRX2
#	FDX1
#	MTHFD2

Metals and cofactors

#	FAM210B
#	CYB5B
#	SLC25A20
#	SLC25A3
#	NDUFS2
#	ABCB10
#	FIS1
#	CIS1
#	ABCB6
#	ABCB7
#	KYAT3
#	ETFDH
#	NNT
#	NADK2
#	NAXE
#	SPR
#	FELH
#	TMLHE
#	CPT2
#	COO5
#	COASY
#	NUDT19
#	CPT1A
#	PPOX
#	NAXD
#	COX11
#	ACC2
#	NFS1
#	NDUFV1
#	CYC1
#	SCO1
#	CYP27A1
#	LYRM4
#	IBA57
#	ISCU
#	NFU1
#	SUOX
#	CPOX
#	QDPR
#	CYCS
#	NDUFS7
#	GLRX5
#	COX19
#	HCCS
#	GRPEL1
#	PCSD2
#	COO6
#	PDSS2
#	NDUFV2
#	HSPA9
#	FTH1
#	NUBPL
#	NDUF58
#	SDHB
#	UQCORF1
#	COX17
#	ISCA1
#	COQ9
#	HSCB
#	CHCHD7
#	PP2A
#	ISCA2
#	BOLA1
#	COQ8B
#	ALAS1
#	FDX2
#	GLRX2
#	GRPEL2
#	FDX1

Small molecule transport

#	SLC25A4
#	ABCD3
#	ABCD1
#	SLC25A20
#	SLC25A11
#	SLC25A3
#	SLC25A1
#	SLC25A6
#	SLC25A5
#	ABCB7
#	SLC25A13
#	SLC25A16
#	SLC30A9
#	SFXN1
#	SLC25A5
#	SLC25A46
#	SLC25A12
#	MICU3
#	VDAC2
#	VDAC3
#	VDAC1
#	MCUB
#	CCDC51
#	MICU1
#	MICU2
#	ROMO1
#	STARD7

Signaling

Calcium homeostasis

#	SLC25A4
#	SLC25A3
#	SLC25A6
#	MCU
#	RHOT1
#	SLC25A13
#	SLC25A5
#	RHOT2
#	SLC25A12
#	MICU3
#	VDAC3
#	VDAC1
#	ETFDH
#	LETM1
#	MCUB
#	MICU1
#	MICU2
#	PIPF

Immune response

#	NLRX1
#	C1QBP
#	CPT1A
#	PPOX
#	NAXD
#	COX11
#	ACC2
#	NFS1
#	NDUFV1
#	CYC1
#	SCO1
#	CYP27A1
#	LYRM4
#	IBA57
#	ISCU
#	NFU1
#	SUOX
#	CPOX
#	QDPR
#	CYCS
#	NDUFS7
#	GLRX5
#	COX19
#	HCCS
#	GRPEL1
#	PCSD2
#	COO6
#	PDSS2
#	NDUFV2
#	HSPA9
#	FTH1
#	NUBPL
#	NDUF58
#	SDHB
#	UQCORF1
#	COX17
#	ISCA1
#	COQ9
#	HSCB
#	CHCHD7
#	PP2A
#	ISCA2
#	BOLA1
#	COQ8B
#	ALAS1
#	FDX2
#	GLRX2
#	GRPEL2
#	FDX1

cAMP-PKA signaling

#	AKAP10
#	AKAP1

Dynamics & surveillance

#	GHITM
#	FIS1
#	MGARP
#	BCL2L13
#	ATP5MG
#	BAK1
#	BCL2L1
#	RHOT1
#	MTX1
#	MFN2
#	SAMM50
#	ARMCX1
#	MTX3
#	RAB24
#	RHOT2
#	OPA1
#	MFF
#	SLC25A46
#	NIPSNAP1
#	MTX2
#	CASP8
#	DIABLO
#	ARMCX3
#	MFN1
#	RMDN3
#	APOO
#	ENDOG
#	VDAC1
#	BNIP3L
#	CHCHD6
#	AIFM1
#	CASP3
#	APOL
#	DNAJC11
#	BAD
#	FUNDC2
#	CYCS
#	TMEM11
#	ATAD3B
#	HTRA2
#	ARL2
#	ATAD3A
#	IMMT
#	TONM20
#	BAX
#	AHCYL1
#	NIPSNAP2
#	STX17
#	BNIP3
#	PGAM5
#	ATP5ME
#	BID
#	SPIRE1
#	PARK7
#	CHCHD2
#	NBR1
#	SNAP29
#	CHCHD3
#	MIEF1

Appendix 2. List of entire MitoCarta 3.0 genes quantified and analyzed by time-resolved proteomics

(continued)

Central dogma

mtDNA maintenance		Translation	
#	PPA2	#	RMND1
#	POLRMT	#	RARS2
#	ENDOG	#	IARS2
#	POLG	#	OXA1L
#	EXOG	#	MRPS27
#	POLDIP2	#	NARS2
#	ATAD3B	#	LRPPRC
#	POLB	#	EARS2
#	ATAD3A	#	MAARS2
#	TFB2M	#	PPA2
#	APEX1	#	CARS2
#	LIG3	#	GFM2
#	MGME1	#	EXD2
#	RNASEH1	#	YARS2
#	TFAM	#	LARS2
		#	P.TCD3
		#	AARS2
		#	DAP3
		#	MRPS2
		#	TIMM21
		#	MRPL37
		#	NOA1
		#	DARS2
		#	MTFMT
		#	NSUN4
		#	MRPS5
		#	MRPL38
		#	MTIF3
		#	GFM1
		#	WARS2
		#	MRPL4
		#	GUF1
		#	MTIF2
		#	TUFM
		#	HARS2
		#	MTERF4
		#	GTPBP10
		#	MRPS22
		#	IARS2
		#	DHX30
		#	COA3
		#	QRSL1
		#	MRPL21
		#	FARS2
		#	MRPS31
		#	GATB
		#	MTRF1L
		#	MRPS34
		#	MTG1
		#	TSM
		#	MRPL10
		#	MRPS30
		#	TFB1M
		#	MRPL48
		#	MRPS15
		#	SLIRP
		#	MRPL18
		#	MRPS6
		#	MRPS35
		#	PDF
		#	MTRF1
		#	MRPL13
		#	TACO1
		#	MRPS10
		#	MRPS25
		#	MRPL3
		#	MRPL39
		#	MRPL43
		#	MRPL44
		#	FASTKD2
		#	MRPS21
		#	MRPL16
		#	MRPL15
		#	CHCHD1
		#	MRPL42
		#	MRPL12
		#	MRPL53
		#	MRPS7
		#	MRPL24
		#	MRPL32
		#	MRPS14
		#	MRPL49
		#	MRPS16
		#	MRPL19
		#	MRPL50
		#	METTL17
		#	MRPL1
		#	MRPS9
		#	MRPL40
		#	DDX28
		#	MRPL28
		#	MRPL22
		#	MRPL9
		#	AURKAIP1
		#	MRPL41
		#	MRPL17
		#	MRPL46
		#	MRPS23
		#	MRPL54
		#	MRPL58
		#	ERAL1
		#	GADD45GIP1
		#	MRPL35
		#	MRPL2
		#	MRPS26
		#	MRPS18A
		#	MRPL27
		#	MRPL20
		#	MRPL57
		#	MRRF
		#	MIEF1
		#	MRPL14
		#	MRPL11
		#	MRPL51
		#	MRPL55
		#	MRM3
		#	GRSF1
		#	MRPL30
		#	MRPS28
		#	MRPL33
		#	MRPL34
		#	MRPL47
		#	MRPL52

mtRNA metabolism	
#	RMND1
#	LRPPRC
#	PPA2
#	FASTKD5
#	CDK5RAP1
#	SUPV3L1
#	TBRG4
#	POLRMT
#	ENDOG
#	PDE12
#	HSD17B10
#	NSUN2
#	LACTB2
#	MTPAP
#	TRMT1
#	NOA1
#	OSGEP1
#	NSUN4
#	TRNT1
#	QTRT1
#	TRMT5
#	TFB2M
#	REXO2
#	RCC1L
#	DHX30
#	PNPT1
#	TRMT10C
#	ELAC2
#	TFB1M
#	SLIRP
#	MTO1
#	PUS1
#	METTL5
#	TRIT1
#	TRUB2
#	FASTKD2
#	DUS2
#	YRDC
#	METTL15
#	RPUSD3
#	GTPBP3
#	MRPL12
#	MRPS7
#	METTL17
#	MRPS9
#	DDX28
#	RPUSD4
#	ERAL1
#	RNASEH1
#	MRM3
#	GRSF1
#	MRPL47
#	TFAM

Protein import/sorting/homeostasis

Protein homeostasis		Import & sorting	
#	LACTB	#	MTX1
#	SPG7	#	TOMM5
#	NRDC	#	OXA1L
#	MAIF1	#	SAMM50
#	CASP8	#	NRDC
#	PITRM1	#	MTX2
#	FKBP10	#	TOMM40
#	PMPCB	#	CHCHD4
#	AFG3L2	#	PMPCB
#	TRAP1	#	PMPCA
#	PMPCA	#	TIMM44
#	IDE	#	TIMM23
#	NLN	#	UQCRC2
#	XPNPEP3	#	XPNPEP3
#	YME1L1	#	AIFM1
#	CASP3	#	DNAJC11
#	LONP1	#	TIMM21
#	MIPE2	#	TOMM22
#	HTRA2	#	MIPE2
#	LAP3	#	UQCRC1
#	CLPX	#	TIMM50
#	STOML2	#	GRPEL1
#	CLPP	#	TOMM20
#	PHB	#	TIMM29
#	PHB2	#	TIMM17A
#	CLPB	#	TOMM70
#	TIMM8A	#	DNAJC19
#	PDF	#	TOMM6
#	HSPD1	#	TIMM8A
#	PARK7	#	ROMO1
#	TIMM13	#	TIMM13
#	HSPE1	#	DNAJC15
#	TIMM9	#	TIMM9
#	TIMM10	#	TIMM10
#	TIMM8B	#	GFE10
#	DNLZ	#	TIMM8B
		#	GRPEL2
		#	TOMM34

OXPHOS

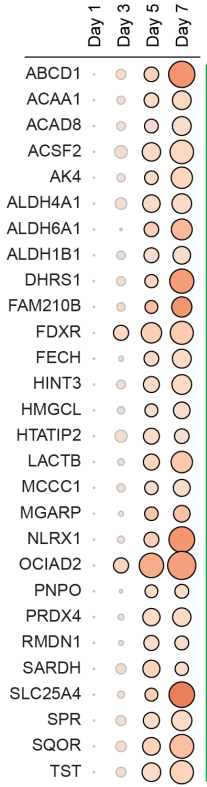
Complex 1		OXPHOS assembly	
#	NDUFB5	#	NDUFA4
#	NDUF2	#	BCS1L
#	NDUFC2	#	ATPAF2
#	NDUFA9	#	TMEM126A
#	NDUFA11	#	PNKD
#	NDUFB11	#	TTC19
#	NDUFA13	#	ACA19
#	NDUFB10	#	TIMMDC1
#	NDUFB6	#	COX11
#	NDUFV1	#	AIFM1
#	NDUF7	#	SCO1
#	NDUFA12	#	TIMM21
#	NDUFB1	#	SMIM20
#	NDUFB9	#	FOXRED1
#	NDUFB1	#	LYRM2
#	NDUFV2	#	COX19
#	NDUFB10	#	CMC1
#	NDUFA4	#	COX7A2L
#	NDUFS8	#	NDUFAF3
#	NDUFS5	#	NDUFAF2
#	NDUFB4	#	COX20
#	NDUFA2	#	NUBPL
#	NDUFA5	#	COA3
#	NDUFA8	#	UQCRC2
#	NDUFS6	#	COX17
#	NDUFA7	#	DMAC2
		#	NDUFAF8
		#	ECSIT
		#	TACO1
		#	NDUFAF1
		#	COA
		#	COA6
		#	CEP89
		#	COA4
		#	LYRM7
		#	CMC2

Complex 2		Respirasome assembly	
#	SDHA	#	COX7A2L
#	SDHB		

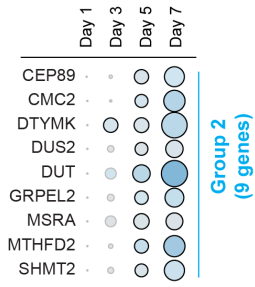
Complex 3		Electron carrier	
#	UQCRC	#	CYB5B
#	UQCRC2	#	SQOR
#	CYC1	#	ETFDH
#	UQCRC1	#	GPD2
#	UQCRCF1	#	ETFA
#	UQCRB	#	CYC1
#	UQCRH	#	ETFB
		#	CYCS
		#	DHODH

Complex 4		Cytochrome C	
#	MT-CO2	#	CYCS
#	NDUFA4	#	HCCS
#	COX4I1		
#	COX7A2L		
#	COX7A2		
#	COX5B		
#	COX5A		
#	COX6C		
#	COX6B1		
#	COX7C		

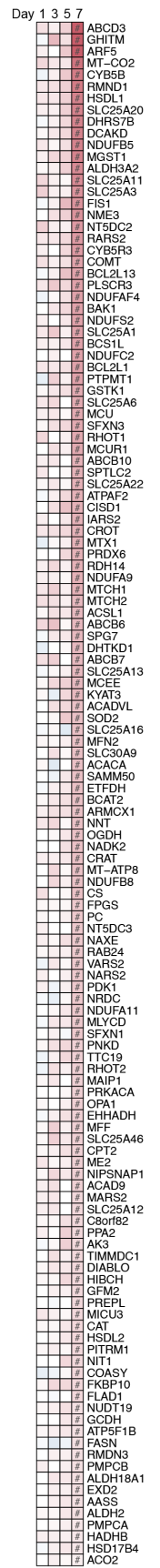
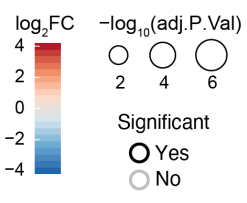
Complex 5	
#	ATP5PB
#	ATP5MG
#	MT-ATP8
#	ATP5F1C
#	ATP5F1B
#	ATP5F1A
#	ATP5PD
#	ATP5F1D
#	ATP5PF
#	ATP5ME
#	ATP5PO
#	ATP5F1E



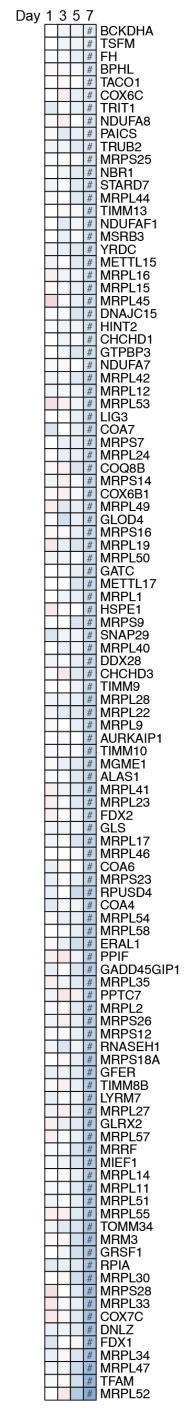
Group 1 (29 genes)



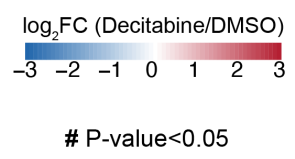
Group 2 (9 genes)



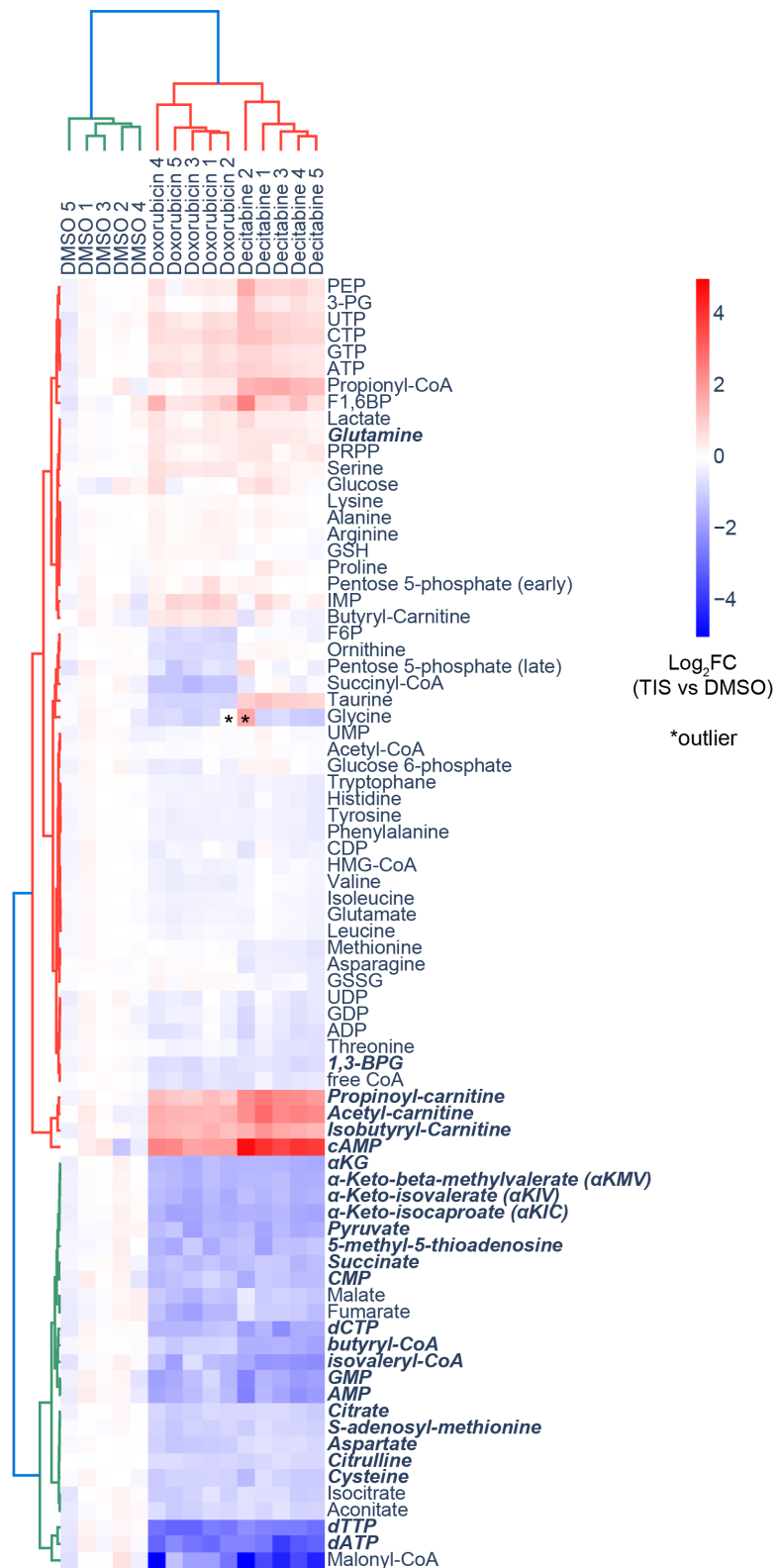
Group 3 (132 genes)



Group 4 (107 genes)



Appendix 3. List of genes of 4 groups divided according to temporal dynamics

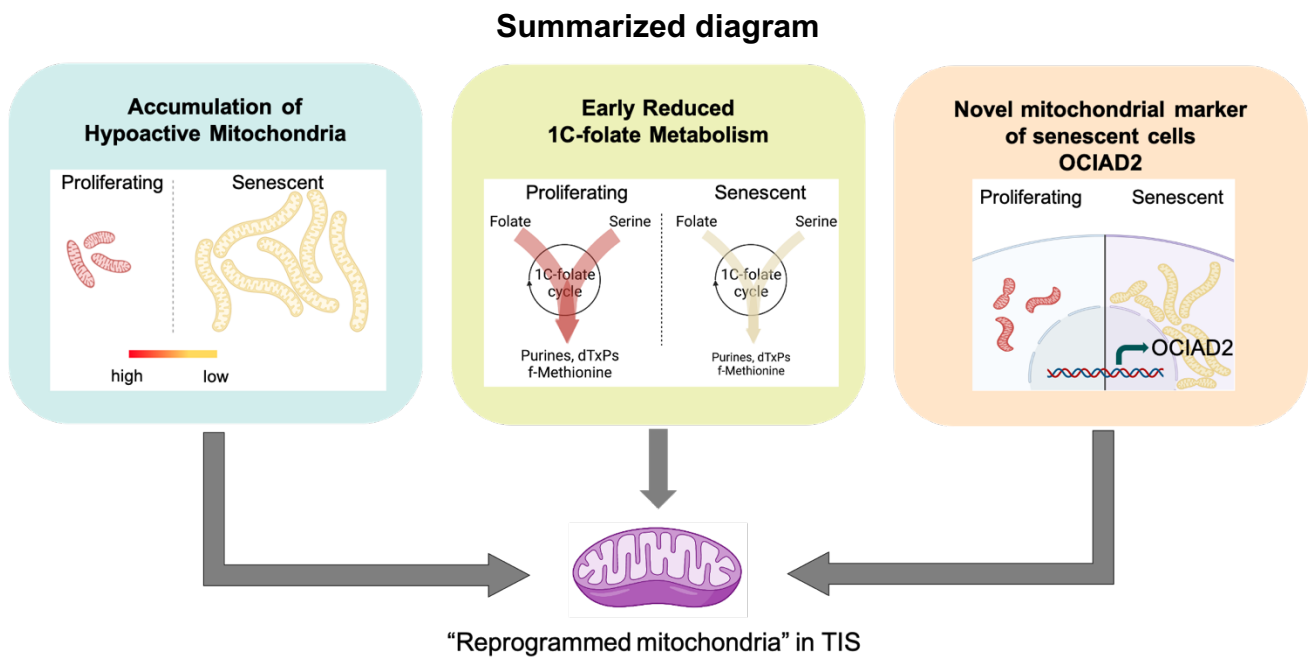


Appendix 4. List of 79 polar metabolites quantified by LC-MS from therapy-induced senescent IMR90 fibroblasts

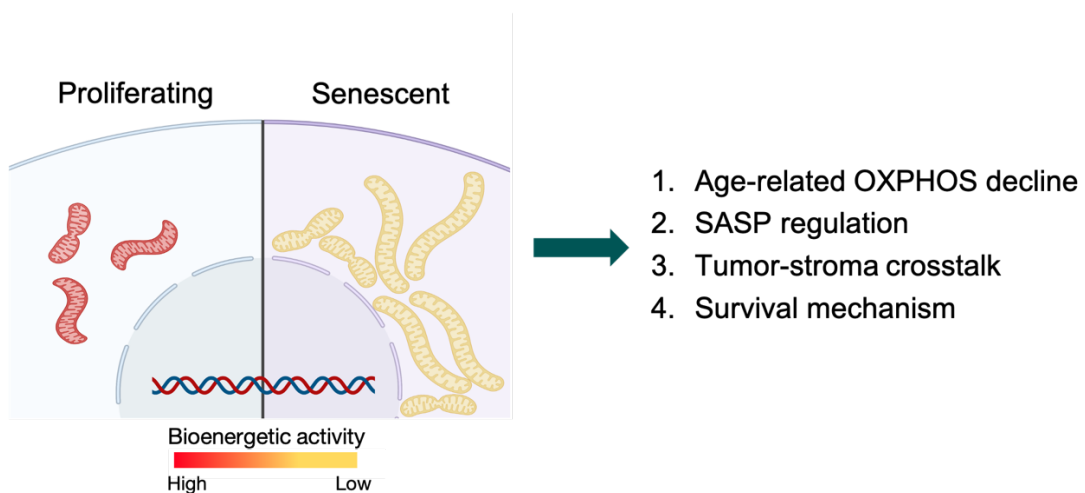
Significantly changed metabolites in both TIS conditions are shown in bold italic font. Welch t-test, Bonferroni-Dunn correction. n=5

8. Summary

Mitochondrial plasticity enabled themselves to transform with the rewired proteome, metabolism, and bioenergetic profile in therapy-induced senescent cells. Such reprogrammed mitochondria implicate their new role and purpose to meet the demands of senescent cells. The findings in this study are summarized graphically as below.



Future hypothesis



9. Acknowledgement

Throughout my PhD study, I learned about mitochondrial plasticity. I believe such plasticity takes place in every layer not only organellar but also organismal as I myself am transformed during my PhD years.

First, I want to thank my mom. She held me through this. It is hard to fathom such fundamental supports simply by words.

Second, I owe Thomas. He led by examples and I was quite occupied to absorb all those lessons during my PhD years. Also, he gave me the second chance to pursue PhD when I was in nadir with skepticism about science. The (almost) only way to reimburse the debt would be by scientific discoveries. I believe we are close there.

Third, I also owe peers that I met on the road. They are the foundation of my daily life. I will not forget what we shared throughout the journey.

Lastly, I acknowledge the two philosophers whom I stand with.

Was mich nicht umbringt, macht mich stärker.

Friedrich Nietzsche, Götzen-Dämmerung 1889

Worüber man nicht sprechen kann, darüber muss man schweigen.

Ludwig Wittgenstein, Tractatus Logico-Philosophicus 1922

10. Eidesstaatliche Erklärung

Erklärung zur Dissertation gemäß der Promotionsordnung vom 12. März 2020

***Diese Erklärung muss in der Dissertation enthalten sein.
(This version must be included in the doctoral thesis)***

„Hiermit versichere ich an Eides statt, dass ich die vorliegende Dissertation selbstständig und ohne die Benutzung anderer als der angegebenen Hilfsmittel und Literatur angefertigt habe. Alle Stellen, die wörtlich oder sinngemäß aus veröffentlichten und nicht veröffentlichten Werken dem Wortlaut oder dem Sinn nach entnommen wurden, sind als solche kenntlich gemacht. Ich versichere an Eides statt, dass diese Dissertation noch keiner anderen Fakultät oder Universität zur Prüfung vorgelegen hat; dass sie - abgesehen von unten angegebenen Teilpublikationen und eingebundenen Artikeln und Manuskripten - noch nicht veröffentlicht worden ist sowie, dass ich eine Veröffentlichung der Dissertation vor Abschluss der Promotion nicht ohne Genehmigung des Promotionsausschusses vornehmen werde. Die Bestimmungen dieser Ordnung sind mir bekannt. Darüber hinaus erkläre ich hiermit, dass ich die Ordnung zur Sicherung guter wissenschaftlicher Praxis und zum Umgang mit wissenschaftlichem Fehlverhalten der Universität zu Köln gelesen und sie bei der Durchführung der Dissertation zugrundeliegenden Arbeiten und der schriftlich verfassten Dissertation beachtet habe und verpflichte mich hiermit, die dort genannten Vorgaben bei allen wissenschaftlichen Tätigkeiten zu beachten und umzusetzen. Ich versichere, dass die eingereichte elektronische Fassung der eingereichten Druckfassung vollständig entspricht.“

Teilpublikationen:

Not applicable

Datum, Name und Unterschrift

07. 06. 2022

Jun Yong Kim



11. Curriculum vitae

KIM, JUN YONG

Postdoctoral researcher
Max Planck Institute for Biology of Ageing, Cologne, Germany
jkim@age.mpg.de
baizzang1@gmail.com

<u>Nationality</u>	Republic of Korea (South Korea)	
<u>Date of birth</u>	10 th March, 1988	
<u>Education</u>	Chungbuk National University, South Korea	2007 - 2012
	– B.S. in Pharmacy (achieved pharmacy licensure)	
	Seoul National University, Seoul, South Korea	2012 - 2016
	– M.S. in Pharmacy	
	– Including obligatory military service as a medic for 21 months	
	Ecole Polytechnique Fédérale de Lausanne, Switzerland	
	– PhD candidate	2016 - 2017
	University of Cologne, Germany	2017.09 – 2022. 08
	– PhD study	
	– Passed the exam on 16th Aug, 2022 (<i>Magna cum laude</i>)	

12. Reference

1. Carrel A, Ebeling AH. Age and Multiplication of Fibroblasts. *J Exp Med.* 1921;34(6):599-623.
2. Witkowski JA. Dr. Carrel's immortal cells. *Med Hist.* 1980;24(2):129-42.
3. Hayflick L, Moorhead PS. The serial cultivation of human diploid cell strains. *Exp Cell Res.* 1961;25:585-621.
4. Hayflick L. The Limited in Vitro Lifetime of Human Diploid Cell Strains. *Exp Cell Res.* 1965;37:614-36.
5. Harley CB, Futcher AB, Greider CW. Telomeres shorten during ageing of human fibroblasts. *Nature.* 1990;345(6274):458-60.
6. Allsopp RC, Chang E, Kashefi-Azham M, Rogaev EI, Piatyszek MA, Shay JW, et al. Telomere shortening is associated with cell division in vitro and in vivo. *Exp Cell Res.* 1995;220(1):194-200.
7. Bodnar AG, Ouellette M, Frolkis M, Holt SE, Chiu CP, Morin GB, et al. Extension of life-span by introduction of telomerase into normal human cells. *Science.* 1998;279(5349):349-52.
8. Serrano M, Lin AW, McCurrach ME, Beach D, Lowe SW. Oncogenic ras provokes premature cell senescence associated with accumulation of p53 and p16INK4a. *Cell.* 1997;88(5):593-602.
9. Wei S, Wei S, Sedivy JM. Expression of catalytically active telomerase does not prevent premature senescence caused by overexpression of oncogenic Ha-Ras in normal human fibroblasts. *Cancer Res.* 1999;59(7):1539-43.
10. Sager R. Senescence as a mode of tumor suppression. *Environ Health Perspect.* 1991;93:59-62.
11. Debaq-Chainiaux F, Ben Ameer R, Bauwens E, Dumortier E, Touffaire M, Toussaint O. Stress-Induced (Premature) Senescence. *Healthy Ageing Long.* 2016;4:243-62.
12. Ewald JA, Desotelle JA, Wilding G, Jarrard DF. Therapy-induced senescence in cancer. *J Natl Cancer Inst.* 2010;102(20):1536-46.
13. Sapiha P, Mallette FA. Cellular Senescence in Postmitotic Cells: Beyond Growth Arrest. *Trends Cell Biol.* 2018;28(8):595-607.
14. Campisi J. Aging, cellular senescence, and cancer. *Annu Rev Physiol.* 2013;75:685-705.
15. Beausejour CM, Krtolica A, Galimi F, Narita M, Lowe SW, Yaswen P, et al. Reversal of human cellular senescence: roles of the p53 and p16 pathways. *EMBO J.* 2003;22(16):4212-22.
16. Vredeveld LC, Possik PA, Smit MA, Meissl K, Michaloglou C, Horlings HM, et al. Abrogation of BRAFV600E-induced senescence by PI3K pathway activation contributes to melanomagenesis. *Genes Dev.* 2012;26(10):1055-69.
17. Kaplon J, Zheng L, Meissl K, Chaneton B, Selivanov VA, Mackay G, et al. A key role for mitochondrial gatekeeper pyruvate dehydrogenase in oncogene-induced senescence. *Nature.* 2013;498(7452):109-12.
18. van Deursen JM. The role of senescent cells in ageing. *Nature.* 2014;509(7501):439-46.
19. Munro J, Barr NI, Ireland H, Morrison V, Parkinson EK. Histone deacetylase inhibitors induce a senescence-like state in human cells by a p16-dependent mechanism that is independent of a mitotic clock. *Exp Cell Res.* 2004;295(2):525-38.
20. Guney I, Wu S, Sedivy JM. Reduced c-Myc signaling triggers telomere-independent senescence by regulating Bmi-1 and p16(INK4a). *Proc Natl Acad Sci U S A.* 2006;103(10):3645-50.
21. Passos JF, Nelson G, Wang C, Richter T, Simillion C, Proctor CJ, et al. Feedback between p21 and reactive oxygen production is necessary for cell senescence. *Mol Syst Biol.* 2010;6:347.
22. Correia-Melo C, Marques FD, Anderson R, Hewitt G, Hewitt R, Cole J, et al. Mitochondria are required for pro-ageing features of the senescent phenotype. *EMBO J.* 2016;35(7):724-42.
23. Shah PP, Donahue G, Otte GL, Capell BC, Nelson DM, Cao K, et al. Lamin B1 depletion in senescent cells triggers large-scale changes in gene expression and the chromatin landscape. *Genes Dev.* 2013;27(16):1787-99.
24. Freund A, Laberge RM, Demaria M, Campisi J. Lamin B1 loss is a senescence-associated biomarker. *Mol Biol Cell.* 2012;23(11):2066-75.

25. Dou Z, Xu C, Donahue G, Shimi T, Pan JA, Zhu J, et al. Autophagy mediates degradation of nuclear lamina. *Nature*. 2015;527(7576):105-9.
26. Li T, Kon N, Jiang L, Tan M, Ludwig T, Zhao Y, et al. Tumor suppression in the absence of p53-mediated cell-cycle arrest, apoptosis, and senescence. *Cell*. 2012;149(6):1269-83.
27. Coppe JP, Patil CK, Rodier F, Sun Y, Munoz DP, Goldstein J, et al. Senescence-associated secretory phenotypes reveal cell-nonautonomous functions of oncogenic RAS and the p53 tumor suppressor. *PLoS Biol*. 2008;6(12):2853-68.
28. Basisty N, Kale A, Jeon OH, Kuehnemann C, Payne T, Rao C, et al. A proteomic atlas of senescence-associated secretomes for aging biomarker development. *PLoS Biol*. 2020;18(1):e3000599.
29. Coppe JP, Desprez PY, Krtolica A, Campisi J. The senescence-associated secretory phenotype: the dark side of tumor suppression. *Annu Rev Pathol*. 2010;5:99-118.
30. Yang G, Rosen DG, Zhang Z, Bast RC, Jr., Mills GB, Colacino JA, et al. The chemokine growth-regulated oncogene 1 (Gro-1) links RAS signaling to the senescence of stromal fibroblasts and ovarian tumorigenesis. *Proc Natl Acad Sci U S A*. 2006;103(44):16472-7.
31. Bavik C, Coleman I, Dean JP, Knudsen B, Plymate S, Nelson PS. The gene expression program of prostate fibroblast senescence modulates neoplastic epithelial cell proliferation through paracrine mechanisms. *Cancer Res*. 2006;66(2):794-802.
32. Coppe JP, Kauser K, Campisi J, Beausejour CM. Secretion of vascular endothelial growth factor by primary human fibroblasts at senescence. *J Biol Chem*. 2006;281(40):29568-74.
33. Acosta JC, Banito A, Wuestefeld T, Georgilis A, Janich P, Morton JP, et al. A complex secretory program orchestrated by the inflammasome controls paracrine senescence. *Nat Cell Biol*. 2013;15(8):978-90.
34. Laberge RM, Awad P, Campisi J, Desprez PY. Epithelial-mesenchymal transition induced by senescent fibroblasts. *Cancer Microenviron*. 2012;5(1):39-44.
35. Rodier F, Coppe JP, Patil CK, Hoeijmakers WA, Munoz DP, Raza SR, et al. Persistent DNA damage signalling triggers senescence-associated inflammatory cytokine secretion. *Nat Cell Biol*. 2009;11(8):973-9.
36. Coppe JP, Rodier F, Patil CK, Freund A, Desprez PY, Campisi J. Tumor suppressor and aging biomarker p16(INK4a) induces cellular senescence without the associated inflammatory secretory phenotype. *J Biol Chem*. 2011;286(42):36396-403.
37. Orjalo AV, Bhaumik D, Gengler BK, Scott GK, Campisi J. Cell surface-bound IL-1alpha is an upstream regulator of the senescence-associated IL-6/IL-8 cytokine network. *Proc Natl Acad Sci U S A*. 2009;106(40):17031-6.
38. Chien Y, Scuoppo C, Wang X, Fang X, Balgley B, Bolden JE, et al. Control of the senescence-associated secretory phenotype by NF-kappaB promotes senescence and enhances chemosensitivity. *Genes Dev*. 2011;25(20):2125-36.
39. Acosta JC, O'Loughlen A, Banito A, Guijarro MV, Augert A, Raguz S, et al. Chemokine signaling via the CXCR2 receptor reinforces senescence. *Cell*. 2008;133(6):1006-18.
40. Kuilman T, Michaloglou C, Vredeveld LC, Douma S, van Doorn R, Desmet CJ, et al. Oncogene-induced senescence relayed by an interleukin-dependent inflammatory network. *Cell*. 2008;133(6):1019-31.
41. Freund A, Patil CK, Campisi J. p38MAPK is a novel DNA damage response-independent regulator of the senescence-associated secretory phenotype. *EMBO J*. 2011;30(8):1536-48.
42. Laberge RM, Sun Y, Orjalo AV, Patil CK, Freund A, Zhou L, et al. mTOR regulates the pro-tumorigenic senescence-associated secretory phenotype by promoting IL1A translation. *Nat Cell Biol*. 2015;17(8):1049-61.
43. Herranz N, Gallage S, Mellone M, Wuestefeld T, Klotz S, Hanley CJ, et al. mTOR regulates MAPKAPK2 translation to control the senescence-associated secretory phenotype. *Nat Cell Biol*. 2015;17(9):1205-17.

44. Bent EH, Gilbert LA, Hemann MT. A senescence secretory switch mediated by PI3K/AKT/mTOR activation controls chemoprotective endothelial secretory responses. *Genes Dev.* 2016;30(16):1811-21.
45. Ortiz-Prado E, Dunn JF, Vasconez J, Castillo D, Viscor G. Partial pressure of oxygen in the human body: a general review. *Am J Blood Res.* 2019;9(1):1-14.
46. Coppe JP, Patil CK, Rodier F, Krtolica A, Beausejour CM, Parrinello S, et al. A human-like senescence-associated secretory phenotype is conserved in mouse cells dependent on physiological oxygen. *PLoS One.* 2010;5(2):e9188.
47. van Vliet T, Varela-Eirin M, Wang B, Borghesan M, Brandenburg SM, Franzin R, et al. Physiological hypoxia restrains the senescence-associated secretory phenotype via AMPK-mediated mTOR suppression. *Mol Cell.* 2021;81(9):2041-52 e6.
48. Hoare M, Ito Y, Kang TW, Weekes MP, Matheson NJ, Patten DA, et al. NOTCH1 mediates a switch between two distinct secretomes during senescence. *Nat Cell Biol.* 2016;18(9):979-92.
49. Ito Y, Hoare M, Narita M. Spatial and Temporal Control of Senescence. *Trends Cell Biol.* 2017;27(11):820-32.
50. Rao SG, Jackson JG. SASP: Tumor Suppressor or Promoter? Yes! *Trends Cancer.* 2016;2(11):676-87.
51. Jun JI, Lau LF. The matricellular protein CCN1 induces fibroblast senescence and restricts fibrosis in cutaneous wound healing. *Nat Cell Biol.* 2010;12(7):676-85.
52. Demaria M, Ohtani N, Youssef SA, Rodier F, Toussaint W, Mitchell JR, et al. An essential role for senescent cells in optimal wound healing through secretion of PDGF-AA. *Dev Cell.* 2014;31(6):722-33.
53. Krizhanovsky V, Yon M, Dickins RA, Hearn S, Simon J, Miething C, et al. Senescence of activated stellate cells limits liver fibrosis. *Cell.* 2008;134(4):657-67.
54. Munoz-Espin D, Canamero M, Maraver A, Gomez-Lopez G, Contreras J, Murillo-Cuesta S, et al. Programmed cell senescence during mammalian embryonic development. *Cell.* 2013;155(5):1104-18.
55. Storer M, Mas A, Robert-Moreno A, Pecoraro M, Ortells MC, Di Giacomo V, et al. Senescence is a developmental mechanism that contributes to embryonic growth and patterning. *Cell.* 2013;155(5):1119-30.
56. Rajagopalan S, Long EO. Cellular senescence induced by CD158d reprograms natural killer cells to promote vascular remodeling. *Proc Natl Acad Sci U S A.* 2012;109(50):20596-601.
57. Ovadya Y, Krizhanovsky V. Senescent cells: SASPected drivers of age-related pathologies. *Biogerontology.* 2014;15(6):627-42.
58. Xue W, Zender L, Miething C, Dickins RA, Hernando E, Krizhanovsky V, et al. Senescence and tumour clearance is triggered by p53 restoration in murine liver carcinomas. *Nature.* 2007;445(7128):656-60.
59. Kang TW, Yevsa T, Woller N, Hoenicke L, Wuestefeld T, Dauch D, et al. Senescence surveillance of pre-malignant hepatocytes limits liver cancer development. *Nature.* 2011;479(7374):547-51.
60. Franceschi C, Campisi J. Chronic inflammation (inflammaging) and its potential contribution to age-associated diseases. *J Gerontol A Biol Sci Med Sci.* 2014;69 Suppl 1:S4-9.
61. Baker DJ, Wijshake T, Tchkonja T, LeBrasseur NK, Childs BG, van de Sluis B, et al. Clearance of p16Ink4a-positive senescent cells delays ageing-associated disorders. *Nature.* 2011;479(7372):232-6.
62. Baker DJ, Childs BG, Durik M, Wijers ME, Sieben CJ, Zhong J, et al. Naturally occurring p16(Ink4a)-positive cells shorten healthy lifespan. *Nature.* 2016;530(7589):184-9.
63. Kaur J, Farr JN. Cellular senescence in age-related disorders. *Transl Res.* 2020;226:96-104.

64. Krtolica A, Parrinello S, Lockett S, Desprez PY, Campisi J. Senescent fibroblasts promote epithelial cell growth and tumorigenesis: a link between cancer and aging. *Proc Natl Acad Sci U S A*. 2001;98(21):12072-7.
65. Liu D, Hornsby PJ. Senescent human fibroblasts increase the early growth of xenograft tumors via matrix metalloproteinase secretion. *Cancer Res*. 2007;67(7):3117-26.
66. Parrinello S, Coppe JP, Krtolica A, Campisi J. Stromal-epithelial interactions in aging and cancer: senescent fibroblasts alter epithelial cell differentiation. *J Cell Sci*. 2005;118(Pt 3):485-96.
67. Sun Y, Campisi J, Higano C, Beer TM, Porter P, Coleman I, et al. Treatment-induced damage to the tumor microenvironment promotes prostate cancer therapy resistance through WNT16B. *Nat Med*. 2012;18(9):1359-68.
68. Gilbert LA, Hemann MT. DNA damage-mediated induction of a chemoresistant niche. *Cell*. 2010;143(3):355-66.
69. Ruscetti M, Morris JPt, Mezzadra R, Russell J, Leibold J, Romesser PB, et al. Senescence-Induced Vascular Remodeling Creates Therapeutic Vulnerabilities in Pancreas Cancer. *Cell*. 2021;184(18):4838-9.
70. Williams GC. Pleiotropy, Natural-Selection, and the Evolution of Senescence. *Evolution*. 1957;11(4):398-411.
71. Childs BG, Gluscevic M, Baker DJ, Laberge RM, Marquess D, Dananberg J, et al. Senescent cells: an emerging target for diseases of ageing. *Nat Rev Drug Discov*. 2017;16(10):718-35.
72. Sullivan LH. 'Kindergarten Chats' + Selected Passages. *Spaz Soc-Space Soc*. 1991;14(54):98-111.
73. Wai T, Langer T. Mitochondrial Dynamics and Metabolic Regulation. *Trends Endocrinol Metab*. 2016;27(2):105-17.
74. Sprenger HG, Langer T. The Good and the Bad of Mitochondrial Breakups. *Trends Cell Biol*. 2019;29(11):888-900.
75. Hoitzing H, Johnston IG, Jones NS. What is the function of mitochondrial networks? A theoretical assessment of hypotheses and proposal for future research. *Bioessays*. 2015;37(6):687-700.
76. Rambold AS, Kostelecky B, Elia N, Lippincott-Schwartz J. Tubular network formation protects mitochondria from autophagosomal degradation during nutrient starvation. *Proc Natl Acad Sci U S A*. 2011;108(25):10190-5.
77. Pickles S, Vigie P, Youle RJ. Mitophagy and Quality Control Mechanisms in Mitochondrial Maintenance. *Curr Biol*. 2018;28(4):R170-R85.
78. Chen H, Detmer SA, Ewald AJ, Griffin EE, Fraser SE, Chan DC. Mitofusins Mfn1 and Mfn2 coordinately regulate mitochondrial fusion and are essential for embryonic development. *J Cell Biol*. 2003;160(2):189-200.
79. Dorn GW, 2nd. Mitochondrial dynamism and heart disease: changing shape and shaping change. *EMBO Mol Med*. 2015;7(7):865-77.
80. Zorzano A, Claret M. Implications of mitochondrial dynamics on neurodegeneration and on hypothalamic dysfunction. *Front Aging Neurosci*. 2015;7:101.
81. Nagashima S, Tokuyama T, Yonashiro R, Inatome R, Yanagi S. Roles of mitochondrial ubiquitin ligase MITOL/MARCH5 in mitochondrial dynamics and diseases. *J Biochem*. 2014;155(5):273-9.
82. Anand R, Wai T, Baker MJ, Kladt N, Schauss AC, Rugarli E, et al. The i-AAA protease YME1L and OMA1 cleave OPA1 to balance mitochondrial fusion and fission. *J Cell Biol*. 2014;204(6):919-29.
83. Ishihara N, Fujita Y, Oka T, Mihara K. Regulation of mitochondrial morphology through proteolytic cleavage of OPA1. *EMBO J*. 2006;25(13):2966-77.
84. Labbe K, Murley A, Nunnari J. Determinants and functions of mitochondrial behavior. *Annu Rev Cell Dev Biol*. 2014;30:357-91.

85. Friedman JR, Lackner LL, West M, DiBenedetto JR, Nunnari J, Voeltz GK. ER tubules mark sites of mitochondrial division. *Science*. 2011;334(6054):358-62.
86. Mears JA, Lackner LL, Fang S, Ingerman E, Nunnari J, Hinshaw JE. Conformational changes in Dnm1 support a contractile mechanism for mitochondrial fission. *Nat Struct Mol Biol*. 2011;18(1):20-6.
87. van der Blik AM, Shen Q, Kawajiri S. Mechanisms of mitochondrial fission and fusion. *Cold Spring Harb Perspect Biol*. 2013;5(6).
88. Ishihara N, Nomura M, Jofuku A, Kato H, Suzuki SO, Masuda K, et al. Mitochondrial fission factor Drp1 is essential for embryonic development and synapse formation in mice. *Nat Cell Biol*. 2009;11(8):958-66.
89. Lane N. Why are cells powered by proton gradients? 2010; 3(9):18. Available from: <https://www.nature.com/scitable/topicpage/why-are-cells-powered-by-proton-gradients-14373960/#>.
90. Silverstein T. The mitochondrial phosphate-to-oxygen ratio is not an integer. *Biochem Mol Biol Educ*. 2005;33(6):416-7.
91. Mitchell P. Coupling of phosphorylation to electron and hydrogen transfer by a chemi-osmotic type of mechanism. *Nature*. 1961;191:144-8.
92. Boyer PD. The ATP synthase--a splendid molecular machine. *Annu Rev Biochem*. 1997;66:717-49.
93. Isaac RS, McShane E, Churchman LS. The Multiple Levels of Mitonuclear Coregulation. *Annu Rev Genet*. 2018;52:511-33.
94. Divakaruni AS, Paradyse A, Ferrick DA, Murphy AN, Jastroch M. Analysis and interpretation of microplate-based oxygen consumption and pH data. *Methods Enzymol*. 2014;547:309-54.
95. Hill BG, Benavides GA, Lancaster JR, Jr., Ballinger S, Dell'Italia L, Jianhua Z, et al. Integration of cellular bioenergetics with mitochondrial quality control and autophagy. *Biol Chem*. 2012;393(12):1485-512.
96. Lunt SY, Vander Heiden MG. Aerobic glycolysis: meeting the metabolic requirements of cell proliferation. *Annu Rev Cell Dev Biol*. 2011;27:441-64.
97. Speijer D. Alternating terminal electron-acceptors at the basis of symbiogenesis: How oxygen ignited eukaryotic evolution. *Bioessays*. 2017;39(2).
98. Spinelli JB, Haigis MC. The multifaceted contributions of mitochondria to cellular metabolism. *Nat Cell Biol*. 2018;20(7):745-54.
99. Neinast M, Murashige D, Arany Z. Branched Chain Amino Acids. *Annu Rev Physiol*. 2019;81:139-64.
100. Chou PY, Fasman GD. Structural and functional role of leucine residues in proteins. *J Mol Biol*. 1973;74(3):263-81.
101. Dill KA. Dominant forces in protein folding. *Biochemistry*. 1990;29(31):7133-55.
102. Wolfson RL, Chantranupong L, Saxton RA, Shen K, Scaria SM, Cantor JR, et al. Sestrin2 is a leucine sensor for the mTORC1 pathway. *Science*. 2016;351(6268):43-8.
103. Gingras AC, Gygi SP, Raught B, Polakiewicz RD, Abraham RT, Hoekstra MF, et al. Regulation of 4E-BP1 phosphorylation: a novel two-step mechanism. *Genes Dev*. 1999;13(11):1422-37.
104. Fajans SS, Quibrera R, Pek S, Floyd JC, Jr., Christensen HN, Conn JW. Stimulation of insulin release in the dog by a nonmetabolizable amino acid. Comparison with leucine and arginine. *J Clin Endocrinol Metab*. 1971;33(1):35-41.
105. Goto M, Shinno H, Ichihara A. Isozyme patterns of branched-chain amino acid transaminase in human tissues and tumors. *Gan*. 1977;68(5):663-7.
106. Uhlen M, Fagerberg L, Hallstrom BM, Lindskog C, Oksvold P, Mardinoglu A, et al. Proteomics. Tissue-based map of the human proteome. *Science*. 2015;347(6220):1260419.

107. She P, Reid TM, Bronson SK, Vary TC, Hajnal A, Lynch CJ, et al. Disruption of BCATm in mice leads to increased energy expenditure associated with the activation of a futile protein turnover cycle. *Cell Metab.* 2007;6(3):181-94.
108. Yoneshiro T, Wang Q, Tajima K, Matsushita M, Maki H, Igarashi K, et al. BCAA catabolism in brown fat controls energy homeostasis through SLC25A44. *Nature.* 2019;572(7771):614-9.
109. Paxton R, Harris RA. Isolation of rabbit liver branched chain alpha-ketoacid dehydrogenase and regulation by phosphorylation. *J Biol Chem.* 1982;257(23):14433-9.
110. Shimomura Y, Honda T, Shiraki M, Murakami T, Sato J, Kobayashi H, et al. Branched-chain amino acid catabolism in exercise and liver disease. *J Nutr.* 2006;136(1 Suppl):250S-3S.
111. Indiveri C, Iacobazzi V, Tonazzi A, Giangregorio N, Infantino V, Convertini P, et al. The mitochondrial carnitine/acylcarnitine carrier: function, structure and physiopathology. *Mol Aspects Med.* 2011;32(4-6):223-33.
112. Mosaoa R, Kasprzyk-Pawelec A, Fernandez HR, Avantaggiati ML. The Mitochondrial Citrate Carrier SLC25A1/CIC and the Fundamental Role of Citrate in Cancer, Inflammation and Beyond. *Biomolecules.* 2021;11(2).
113. Neinast MD, Jang C, Hui S, Murashige DS, Chu Q, Morscher RJ, et al. Quantitative Analysis of the Whole-Body Metabolic Fate of Branched-Chain Amino Acids. *Cell Metab.* 2019;29(2):417-29 e4.
114. Green CR, Wallace M, Divakaruni AS, Phillips SA, Murphy AN, Ciaraldi TP, et al. Branched-chain amino acid catabolism fuels adipocyte differentiation and lipogenesis. *Nat Chem Biol.* 2016;12(1):15-21.
115. Ducker GS, Chen L, Morscher RJ, Ghergurovich JM, Esposito M, Teng X, et al. Reversal of Cytosolic One-Carbon Flux Compensates for Loss of the Mitochondrial Folate Pathway. *Cell Metab.* 2016;23(6):1140-53.
116. Lemons JM, Feng XJ, Bennett BD, Legesse-Miller A, Johnson EL, Raitman I, et al. Quiescent fibroblasts exhibit high metabolic activity. *PLoS Biol.* 2010;8(10):e1000514.
117. Farber S, Diamond LK. Temporary remissions in acute leukemia in children produced by folic acid antagonist, 4-aminopteroyl-glutamic acid. *N Engl J Med.* 1948;238(23):787-93.
118. Ron-Harel N, Santos D, Ghergurovich JM, Sage PT, Reddy A, Lovitch SB, et al. Mitochondrial Biogenesis and Proteome Remodeling Promote One-Carbon Metabolism for T Cell Activation. *Cell Metab.* 2016;24(1):104-17.
119. Anderson DD, Quintero CM, Stover PJ. Identification of a de novo thymidylate biosynthesis pathway in mammalian mitochondria. *Proc Natl Acad Sci U S A.* 2011;108(37):15163-8.
120. Tucker EJ, Hershman SG, Kohrer C, Belcher-Timme CA, Patel J, Goldberger OA, et al. Mutations in MTFMT underlie a human disorder of formylation causing impaired mitochondrial translation. *Cell Metab.* 2011;14(3):428-34.
121. Morscher RJ, Ducker GS, Li SH, Mayer JA, Gitai Z, Sperl W, et al. Mitochondrial translation requires folate-dependent tRNA methylation. *Nature.* 2018;554(7690):128-32.
122. Minton DR, Nam M, McLaughlin DJ, Shin J, Bayraktar EC, Alvarez SW, et al. Serine Catabolism by SHMT2 Is Required for Proper Mitochondrial Translation Initiation and Maintenance of Formylmethionyl-tRNAs. *Mol Cell.* 2018;69(4):610-21 e5.
123. Tran DH, Kesavan R, Rion H, Soflaee MH, Solmonson A, Bezwada D, et al. Mitochondrial NADP(+) is essential for proline biosynthesis during cell growth. *Nat Metab.* 2021;3(4):571-85.
124. Zhu J, Schworer S, Berisa M, Kyung YJ, Ryu KW, Yi J, et al. Mitochondrial NADP(H) generation is essential for proline biosynthesis. *Science.* 2021;372(6545):968-72.
125. Ju HQ, Lin JF, Tian T, Xie D, Xu RH. NADPH homeostasis in cancer: functions, mechanisms and therapeutic implications. *Signal Transduct Target Ther.* 2020;5(1):231.
126. Han C, Liu Y, Dai R, Ismail N, Su W, Li B. Ferroptosis and Its Potential Role in Human Diseases. *Front Pharmacol.* 2020;11:239.

127. Ducker GS, Rabinowitz JD. One-Carbon Metabolism in Health and Disease. *Cell Metab.* 2017;25(1):27-42.
128. MacFarlane AJ, Liu X, Perry CA, Flodby P, Allen RH, Stabler SP, et al. Cytoplasmic serine hydroxymethyltransferase regulates the metabolic partitioning of methylenetetrahydrofolate but is not essential in mice. *J Biol Chem.* 2008;283(38):25846-53.
129. Tani H, Ohnishi S, Shitara H, Mito T, Yamaguchi M, Yonekawa H, et al. Mice deficient in the *Shmt2* gene have mitochondrial respiration defects and are embryonic lethal. *Sci Rep.* 2018;8(1):425.
130. Momb J, Lewandowski JP, Bryant JD, Fitch R, Surman DR, Vokes SA, et al. Deletion of *Mthfd1l* causes embryonic lethality and neural tube and craniofacial defects in mice. *Proc Natl Acad Sci U S A.* 2013;110(2):549-54.
131. MacFarlane AJ, Perry CA, Girnary HH, Gao D, Allen RH, Stabler SP, et al. *Mthfd1* is an essential gene in mice and alters biomarkers of impaired one-carbon metabolism. *J Biol Chem.* 2009;284(3):1533-9.
132. Lopez-Otin C, Blasco MA, Partridge L, Serrano M, Kroemer G. The hallmarks of aging. *Cell.* 2013;153(6):1194-217.
133. Butow RA, Avadhani NG. Mitochondrial signaling: the retrograde response. *Mol Cell.* 2004;14(1):1-15.
134. Childs BG, Baker DJ, Kirkland JL, Campisi J, van Deursen JM. Senescence and apoptosis: dueling or complementary cell fates? *EMBO Rep.* 2014;15(11):1139-53.
135. Packer L, Fuehr K. Low oxygen concentration extends the lifespan of cultured human diploid cells. *Nature.* 1977;267(5610):423-5.
136. Chen Q, Fischer A, Reagan JD, Yan LJ, Ames BN. Oxidative DNA damage and senescence of human diploid fibroblast cells. *Proc Natl Acad Sci U S A.* 1995;92(10):4337-41.
137. von Zglinicki T. Oxidative stress shortens telomeres. *Trends Biochem Sci.* 2002;27(7):339-44.
138. Saretzki G, Murphy MP, von Zglinicki T. MitoQ counteracts telomere shortening and elongates lifespan of fibroblasts under mild oxidative stress. *Aging Cell.* 2003;2(2):141-3.
139. Passos JF, Saretzki G, Ahmed S, Nelson G, Richter T, Peters H, et al. Mitochondrial dysfunction accounts for the stochastic heterogeneity in telomere-dependent senescence. *PLoS Biol.* 2007;5(5):e110.
140. Gregg SQ, Robinson AR, Niedernhofer LJ. Physiological consequences of defects in ERCC1-XPF DNA repair endonuclease. *DNA Repair (Amst).* 2011;10(7):781-91.
141. Robinson AR, Yousefzadeh MJ, Rozgaja TA, Wang J, Li X, Tilstra JS, et al. Spontaneous DNA damage to the nuclear genome promotes senescence, redox imbalance and aging. *Redox Biol.* 2018;17:259-73.
142. Hara H, Araya J, Ito S, Kobayashi K, Takasaka N, Yoshii Y, et al. Mitochondrial fragmentation in cigarette smoke-induced bronchial epithelial cell senescence. *Am J Physiol Lung Cell Mol Physiol.* 2013;305(10):L737-46.
143. Araya J, Tsubouchi K, Sato N, Ito S, Minagawa S, Hara H, et al. PRKN-regulated mitophagy and cellular senescence during COPD pathogenesis. *Autophagy.* 2019;15(3):510-26.
144. Mai S, Muster B, Bereiter-Hahn J, Jendrach M. Autophagy proteins LC3B, ATG5 and ATG12 participate in quality control after mitochondrial damage and influence lifespan. *Autophagy.* 2012;8(1):47-62.
145. Mai S, Klinkenberg M, Auburger G, Bereiter-Hahn J, Jendrach M. Decreased expression of Drp1 and Fis1 mediates mitochondrial elongation in senescent cells and enhances resistance to oxidative stress through PINK1. *J Cell Sci.* 2010;123(Pt 6):917-26.
146. Jendrach M, Pohl S, Voth M, Kowald A, Hammerstein P, Bereiter-Hahn J. Morpho-dynamic changes of mitochondria during ageing of human endothelial cells. *Mech Ageing Dev.* 2005;126(6-7):813-21.

147. Ahmad T, Sundar IK, Lerner CA, Gerloff J, Tormos AM, Yao H, et al. Impaired mitophagy leads to cigarette smoke stress-induced cellular senescence: implications for chronic obstructive pulmonary disease. *FASEB J.* 2015;29(7):2912-29.
148. Lee HC, Yin PH, Chi CW, Wei YH. Increase in mitochondrial mass in human fibroblasts under oxidative stress and during replicative cell senescence. *J Biomed Sci.* 2002;9(6 Pt 1):517-26.
149. Yu B, Ma J, Li J, Wang D, Wang Z, Wang S. Mitochondrial phosphatase PGAM5 modulates cellular senescence by regulating mitochondrial dynamics. *Nat Commun.* 2020;11(1):2549.
150. Moiseeva O, Bourdeau V, Roux A, Deschenes-Simard X, Ferbeyre G. Mitochondrial dysfunction contributes to oncogene-induced senescence. *Mol Cell Biol.* 2009;29(16):4495-507.
151. Bartoletti-Stella A, Mariani E, Kurelac I, Maresca A, Caratozzolo MF, Iommarini L, et al. Gamma rays induce a p53-independent mitochondrial biogenesis that is counter-regulated by HIF1alpha. *Cell Death Dis.* 2013;4:e663.
152. Dalle Pezze P, Nelson G, Otten EG, Korolchuk VI, Kirkwood TB, von Zglinicki T, et al. Dynamic modelling of pathways to cellular senescence reveals strategies for targeted interventions. *PLoS Comput Biol.* 2014;10(8):e1003728.
153. Zhou X, Li N, Wang Y, Wang Y, Zhang X, Zhang H. Effects of X-irradiation on mitochondrial DNA damage and its supercoiling formation change. *Mitochondrion.* 2011;11(6):886-92.
154. Korolchuk VI, Miwa S, Carroll B, von Zglinicki T. Mitochondria in Cell Senescence: Is Mitophagy the Weakest Link? *EBioMedicine.* 2017;21:7-13.
155. Garcia-Prat L, Martinez-Vicente M, Perdiguero E, Ortet L, Rodriguez-Ubreva J, Rebollo E, et al. Autophagy maintains stemness by preventing senescence. *Nature.* 2016;529(7584):37-42.
156. Youle RJ, Narendra DP. Mechanisms of mitophagy. *Nat Rev Mol Cell Biol.* 2011;12(1):9-14.
157. Nacarelli T, Lau L, Fukumoto T, Zundell J, Fatkhutdinov N, Wu S, et al. NAD(+) metabolism governs the proinflammatory senescence-associated secretome. *Nat Cell Biol.* 2019;21(3):397-407.
158. Johmura Y, Yamanaka T, Omori S, Wang TW, Sugiura Y, Matsumoto M, et al. Senolysis by glutaminolysis inhibition ameliorates various age-associated disorders. *Science.* 2021;371(6526):265-70.
159. Quijano C, Cao L, Fergusson MM, Romero H, Liu J, Gutkind S, et al. Oncogene-induced senescence results in marked metabolic and bioenergetic alterations. *Cell Cycle.* 2012;11(7):1383-92.
160. Flor AC, Wolfgeher D, Wu D, Kron SJ. A signature of enhanced lipid metabolism, lipid peroxidation and aldehyde stress in therapy-induced senescence. *Cell Death Discov.* 2017;3:17075.
161. Velarde MC, Flynn JM, Day NU, Melov S, Campisi J. Mitochondrial oxidative stress caused by Sod2 deficiency promotes cellular senescence and aging phenotypes in the skin. *Aging (Albany NY).* 2012;4(1):3-12.
162. Velarde MC, Demaria M, Melov S, Campisi J. Pleiotropic age-dependent effects of mitochondrial dysfunction on epidermal stem cells. *Proc Natl Acad Sci U S A.* 2015;112(33):10407-12.
163. Wiley CD, Velarde MC, Lecot P, Liu S, Sarnoski EA, Freund A, et al. Mitochondrial Dysfunction Induces Senescence with a Distinct Secretory Phenotype. *Cell Metab.* 2016;23(2):303-14.
164. Vizioli MG, Liu T, Miller KN, Robertson NA, Gilroy K, Lagnado AB, et al. Mitochondria-to-nucleus retrograde signaling drives formation of cytoplasmic chromatin and inflammation in senescence. *Genes Dev.* 2020;34(5-6):428-45.
165. Trifunovic A, Wredenberg A, Falkenberg M, Spelbrink JN, Rovio AT, Bruder CE, et al. Premature ageing in mice expressing defective mitochondrial DNA polymerase. *Nature.* 2004;429(6990):417-23.
166. Lee S, Jeong SY, Lim WC, Kim S, Park YY, Sun X, et al. Mitochondrial fission and fusion mediators, hFis1 and OPA1, modulate cellular senescence. *J Biol Chem.* 2007;282(31):22977-83.

167. Park YY, Lee S, Karbowski M, Neutzner A, Youle RJ, Cho H. Loss of MARCH5 mitochondrial E3 ubiquitin ligase induces cellular senescence through dynamin-related protein 1 and mitofusin 1. *J Cell Sci.* 2010;123(Pt 4):619-26.
168. Dorr JR, Yu Y, Milanovic M, Beuster G, Zasada C, Dabritz JH, et al. Synthetic lethal metabolic targeting of cellular senescence in cancer therapy. *Nature.* 2013;501(7467):421-5.
169. Hutter E, Renner K, Pfister G, Stockl P, Jansen-Durr P, Gnaiger E. Senescence-associated changes in respiration and oxidative phosphorylation in primary human fibroblasts. *Biochemical Journal.* 2004;380:919-28.
170. Hubackova S, Davidova E, Rohlenova K, Stursa J, Werner L, Andera L, et al. Selective elimination of senescent cells by mitochondrial targeting is regulated by ANT2. *Cell Death Differ.* 2019;26(2):276-90.
171. Yoon YS, Yoon DS, Lim IK, Yoon SH, Chung HY, Rojo M, et al. Formation of elongated giant mitochondria in DFO-induced cellular senescence: involvement of enhanced fusion process through modulation of Fis1. *J Cell Physiol.* 2006;209(2):468-80.
172. Luo LY, Soosaipillai A, Diamandis EP. Molecular cloning of a novel human gene on chromosome 4p11 by immunoscreening of an ovarian carcinoma cDNA library. *Biochem Biophys Res Commun.* 2001;280(1):401-6.
173. Sengupta S, Michener CM, Escobar P, Belinson J, Ganapathi R. Ovarian cancer immunoreactive antigen domain containing 1 (OCIAD1), a key player in ovarian cancer cell adhesion. *Gynecol Oncol.* 2008;109(2):226-33.
174. Strausberg RL, Feingold EA, Grouse LH, Derge JG, Klausner RD, Collins FS, et al. Generation and initial analysis of more than 15,000 full-length human and mouse cDNA sequences. *Proc Natl Acad Sci U S A.* 2002;99(26):16899-903.
175. Sinha S, Bheemsetty VA, Inamdar MS. A double helical motif in OCIAD2 is essential for its localization, interactions and STAT3 activation. *Sci Rep.* 2018;8(1):7362.
176. Rath S, Sharma R, Gupta R, Ast T, Chan C, Durham TJ, et al. MitoCarta3.0: an updated mitochondrial proteome now with sub-organelle localization and pathway annotations. *Nucleic Acids Res.* 2021;49(D1):D1541-D7.
177. Han J, Jung S, Jang J, Kam TI, Choi H, Kim BJ, et al. OCIAD2 activates gamma-secretase to enhance amyloid beta production by interacting with nicastrin. *Cell Mol Life Sci.* 2014;71(13):2561-76.
178. Chojnacka KJ, Elancheliyan P, Mussulini BHM, Mohanraj K, Callegari S, Gosk A, et al. Ovarian carcinoma immunoreactive antigen-like protein 2 (OCIAD2) is a novel complex III-specific assembly factor in mitochondria. *Mol Biol Cell.* 2022;33(4):ar29.
179. Le Vasseur M, Friedman J, Jost M, Xu J, Yamada J, Kampmann M, et al. Genome-wide CRISPRi screening identifies OCIAD1 as a prohibitin client and regulatory determinant of mitochondrial Complex III assembly in human cells. *Elife.* 2021;10.
180. Ishiyama T, Kano J, Anami Y, Onuki T, Iijima T, Morisita Y, et al. OCIA domain containing 2 is highly expressed in adenocarcinoma mixed subtype with bronchioloalveolar carcinoma component and is associated with better prognosis. *Cancer Sci.* 2007;98(1):50-7.
181. Honda S, Minato M, Suzuki H, Fujiyoshi M, Miyagi H, Haruta M, et al. Clinical prognostic value of DNA methylation in hepatoblastoma: Four novel tumor suppressor candidates. *Cancer Sci.* 2016;107(6):812-9.
182. Itoguchi N, Nakagawa T, Murata Y, Li D, Shiba-Ishii A, Minami Y, et al. Immunocytochemical staining for stratifin and OCIAD2 in bronchial washing specimens increases sensitivity for diagnosis of lung cancer. *Cytopathology.* 2015;26(6):354-61.
183. Nagata C, Kobayashi H, Sakata A, Satomi K, Minami Y, Morishita Y, et al. Increased expression of OCIA domain containing 2 during stepwise progression of ovarian mucinous tumor. *Pathol Int.* 2012;62(7):471-6.

184. Nikas JB. A mathematical model for short-term vs. long-term survival in patients with glioma. *Am J Cancer Res.* 2014;4(6):862-73.
185. Sakashita M, Sakashita S, Murata Y, Shiba-Ishii A, Kim Y, Matsuoka R, et al. High expression of ovarian cancer immunoreactive antigen domain containing 2 (OCIAD2) is associated with poor prognosis in lung adenocarcinoma. *Pathol Int.* 2018;68(11):596-604.
186. Nikas JB. Independent validation of a mathematical genomic model for survival of glioma patients. *Am J Cancer Res.* 2016;6(6):1408-19.
187. Wu D, Yang X, Peng H, Guo D, Zhao W, Zhao C, et al. OCIAD2 suppressed tumor growth and invasion via AKT pathway in Hepatocellular carcinoma. *Carcinogenesis.* 2017;38(9):910-9.
188. Fecher C, Trovo L, Muller SA, Snaidero N, Wettmarshausen J, Heink S, et al. Cell-type-specific profiling of brain mitochondria reveals functional and molecular diversity. *Nat Neurosci.* 2019;22(10):1731-42.
189. Tröder SE. A protective function against apoptosis revealed by the neuronal interactome of the mitochondrial m-AAA protease: University of Cologne; 2014.
190. MacVicar T, Ohba Y, Nolte H, Mayer FC, Tatsuta T, Sprenger HG, et al. Lipid signalling drives proteolytic rewiring of mitochondria by YME1L. *Nature.* 2019;575(7782):361-5.
191. D'Souza RC, Knittle AM, Nagaraj N, van Dinther M, Choudhary C, ten Dijke P, et al. Time-resolved dissection of early phosphoproteome and ensuing proteome changes in response to TGF-beta. *Sci Signal.* 2014;7(335):rs5.
192. Zhang R, Zhao C, Xiong Z, Zhou X. Pathway bridge based multiobjective optimization approach for lurking pathway prediction. *Biomed Res Int.* 2014;2014:351095.
193. Schindelin J, Arganda-Carreras I, Frise E, Kaynig V, Longair M, Pietzsch T, et al. Fiji: an open-source platform for biological-image analysis. *Nat Methods.* 2012;9(7):676-82.
194. Viana MP, Lim S, Rafelski SM. Quantifying mitochondrial content in living cells. *Methods Cell Biol.* 2015;125:77-93.
195. Frezza C, Cipolat S, Scorrano L. Organelle isolation: functional mitochondria from mouse liver, muscle and cultured fibroblasts. *Nat Protoc.* 2007;2(2):287-95.
196. Sprenger HG, Wani G, Hesselting A, König T, Patron M, MacVicar T, et al. Loss of the mitochondrial i-AAA protease YME1L leads to ocular dysfunction and spinal axonopathy. *EMBO Mol Med.* 2019;11(1).
197. Rappsilber J, Ishihama Y, Mann M. Stop and go extraction tips for matrix-assisted laser desorption/ionization, nanoelectrospray, and LC/MS sample pretreatment in proteomics. *Anal Chem.* 2003;75(3):663-70.
198. Cox J, Mann M. MaxQuant enables high peptide identification rates, individualized p.p.b.-range mass accuracies and proteome-wide protein quantification. *Nat Biotechnol.* 2008;26(12):1367-72.
199. Ritchie ME, Phipson B, Wu D, Hu Y, Law CW, Shi W, et al. limma powers differential expression analyses for RNA-sequencing and microarray studies. *Nucleic Acids Res.* 2015;43(7):e47.
200. R Core Team. R: A Language and Environment for Statistical Computing. R Foundation for Statistical Computing; 2017.
201. Szklarczyk D, Gable AL, Nastou KC, Lyon D, Kirsch R, Pyysalo S, et al. The STRING database in 2021: customizable protein-protein networks, and functional characterization of user-uploaded gene/measurement sets. *Nucleic Acids Res.* 2021;49(D1):D605-D12.
202. Subramanian A, Tamayo P, Mootha VK, Mukherjee S, Ebert BL, Gillette MA, et al. Gene set enrichment analysis: a knowledge-based approach for interpreting genome-wide expression profiles. *Proc Natl Acad Sci U S A.* 2005;102(43):15545-50.
203. Liao Y, Wang J, Jaehnig EJ, Shi Z, Zhang B. WebGestalt 2019: gene set analysis toolkit with revamped UIs and APIs. *Nucleic Acids Res.* 2019;47(W1):W199-W205.
204. Iqbal A, Duitama, C., Metge, F., Rosskopp, D., Boucas, J. Flaski. 2021.

205. Millner A, Atilla-Gokcumen GE. Lipid Players of Cellular Senescence. *Metabolites*. 2020;10(9).
206. Wiley CD, Sharma R, Davis SS, Lopez-Dominguez JA, Mitchell KP, Wiley S, et al. Oxylipin biosynthesis reinforces cellular senescence and allows detection of senolysis. *Cell Metab*. 2021;33(6):1124-36 e5.
207. Millner A, Lizardo DY, Atilla-Gokcumen GE. Untargeted Lipidomics Highlight the Depletion of Deoxyceramides during Therapy-Induced Senescence. *Proteomics*. 2020;20(10):e2000013.
208. Li JT, Yin M, Wang D, Wang J, Lei MZ, Zhang Y, et al. BCAT2-mediated BCAA catabolism is critical for development of pancreatic ductal adenocarcinoma. *Nat Cell Biol*. 2020;22(2):167-74.
209. Wallace M, Green CR, Roberts LS, Lee YM, McCarville JL, Sanchez-Gurmaches J, et al. Enzyme promiscuity drives branched-chain fatty acid synthesis in adipose tissues. *Nat Chem Biol*. 2018;14(11):1021-31.
210. Aird KM, Zhang G, Li H, Tu Z, Bitler BG, Garipov A, et al. Suppression of nucleotide metabolism underlies the establishment and maintenance of oncogene-induced senescence. *Cell Rep*. 2013;3(4):1252-65.
211. Lee JS, Adler L, Karathia H, Carmel N, Rabinovich S, Auslander N, et al. Urea Cycle Dysregulation Generates Clinically Relevant Genomic and Biochemical Signatures. *Cell*. 2018;174(6):1559-70 e22.
212. Schmidt TT, Reyes G, Gries K, Ceylan CU, Sharma S, Meurer M, et al. Alterations in cellular metabolism triggered by URA7 or GLN3 inactivation cause imbalanced dNTP pools and increased mutagenesis. *Proc Natl Acad Sci U S A*. 2017;114(22):E4442-E51.
213. Al-Mehdi AB, Pastukh VM, Swiger BM, Reed DJ, Patel MR, Bardwell GC, et al. Perinuclear mitochondrial clustering creates an oxidant-rich nuclear domain required for hypoxia-induced transcription. *Sci Signal*. 2012;5(231):ra47.
214. Agarwal S, Ganesh S. Perinuclear mitochondrial clustering, increased ROS levels, and HIF1 are required for the activation of HSF1 by heat stress. *J Cell Sci*. 2020;133(13).
215. Thomas LW, Staples O, Turmaine M, Ashcroft M. CHCHD4 Regulates Intracellular Oxygenation and Perinuclear Distribution of Mitochondria. *Front Oncol*. 2017;7:71.
216. Kamerkar SC, Kraus F, Sharpe AJ, Pucadyil TJ, Ryan MT. Dynamin-related protein 1 has membrane constricting and severing abilities sufficient for mitochondrial and peroxisomal fission. *Nat Commun*. 2018;9(1):5239.